國 立 交 通 大 學

電子工程學系 電子研究所碩士班

碩 士 論 文

利用二段式熱化學氣相沉積法成長不同間距

高度比之奈米碳管柱列之場發射特性研究

Study on the Improvement of the Field Emission

Characteristics of Carbon Nanotube Pillar Arrays with

Different Pitch/Height Ratios Using Two-Step Thermal

Chemical Vapor Deposition

研 究 生: 魏 英 彰

指導教授: 邱 碧 秀 博士

鄭 晃 忠 博士

中華民國九十八年七月

利用二段式熱化學氣相沉積法成長不同間距

高度比之奈米碳管柱列之場發射特性研究

The study of Study on the Improvement of the Field Emission Characteristics of Carbon Nanotube Pillar Arrays with Different Pitch/Height Ratios Using Two-Step Thermal Chemical Vapor Deposition

研 究 生：魏英彰　　　　　Student：Yin-Chang Wei

指導教授：邱碧秀 博士　　　Advisor：Dr. Bi-Shiou Chiou

　　　　　鄭晃忠 博士　　　Advisor：Dr. Huang-Chung Cheng

國 立 交 通 大 學

電子工程學系 電子研究所碩士班

碩 士 論 文

A Thesis

Submitted to Department of Electronics Engineering & Institute of Electronics

College of Electrical Engineering and Computer Engineering

National Chiao Tung University

In Partial Fulfillment of the Requirements

For the Degree of

Master

In

Electronics Engineering

July 2009

Hsinchu, Taiwan

中華民國九十八年七月

利用二段式熱化學氣相沉積法成長不同間距

高度比之奈米碳管柱列之場發射特性研究

學生:魏英彰　　　　　　　　　指導教授:邱碧秀 博士

　　　　　　　　　　　　　　　　　　鄭晃忠 博士

國立交通大學

電子工程學系　電子研究所碩士班

摘　要

此篇論文之實驗當中,成長奈米碳管方面,為了可以減低成本且能夠均勻的將奈米碳管應用於場發射顯示器當中,熱化學氣相沉積法比起其他分法具有簡單且低成本的優勢,因此被認為是最具有潛力的碳管成長發法之一。在催化金屬的使用方面,於多層共鍍催化金屬合成柱狀形式奈米管的奈米探管陣列於場發射的應用,採取了鈷鈦共鍍的合金,此方式不僅得到高度一制性的碳管管徑並且利用了金屬鈦於高溫下與炭的化合結果,能夠有效提升奈米碳管對於基板的附著能力以及展現較佳的場發射特性。

首先,根據以往關於柱狀形式奈米碳管用於場發射方面的論文當中,數種不同高寬比都被提及,例如 R/H = 6,R/H=3,R/H=2 等,並沒有真正探討出高寬比與柱狀形式奈米碳管陣列組合上之絕對關係,在這實驗當中,設計了三種不同柱狀奈米碳管之間的間距,且由控制成長時通入碳源的流量與成長的時間可以穩定成長出所需要柱狀奈米碳管的高度,進而討論其 R/H 值,當中,也發現到當柱狀奈米碳管之間的間距越遠,可以得到其對應最小起始電場的理想 R/H 值有趨近於 2 的趨勢,實驗中定義了電流密度為 J=10

$\mu A/cm^2$ 對應到的電場為起始電場，在間距 $80\mu m$，$150\mu m$ 與 $250\mu m$ 最佳 R/H 值為 8，4.7 與 3.2 分別能夠對應到最小起始電場為 $E_{turn-on}=1.78V/\mu m$, $E_{turn-on}=1.55V/\mu m$ 與 $E_{turn-on}=1.53V/\mu m$，並且在最佳 R/H 情況下可以得到均勻性最佳的場發射效果。

根據先前實驗中奈米碳管成長機制，倘若要得到長度較長的奈米碳管，必須控制其成長時碳源氣體流量與成長時間的搭配，因此，改良了單一階段成長的參數而成功的達到二階段形式的成長方式，此方法不僅能夠成長出較高的柱狀碳管並且在場發射方面可以得到相當優異的起始電場 $E_{turn-on}=0.1V/\mu m$, 以及飽和電場 $E_{threshold}=0.3V/\mu m$, 實驗中也定義了電流密度為 $J=10mA/cm^2$ 對應到的電場為飽和電場，並且利用了 SEM, Raman, TEM 作了材料特性方面上的分析。

由於奈米碳管密度會影響其場發射特性，為了使其均勻特性有效提升，近一步使用電漿來改善柱狀奈米碳管的表面密度分佈是可行的方法之一，本論文中提出了使用純氧電漿或氧氣加氬氣的電漿作為柱狀奈米碳管的後段處理，當中發現氧氣加上氬氣的電漿可以藉由改變轟擊的時間，造成某些奈米碳管被摧毀，而留下一些較高的奈米碳管，而這些較高的奈米碳管表現了較高的場發射電流，當中也明顯發現了，經過電漿處理後柱狀奈米碳管的幾何型態有顯著的變化，也因為型態上的改變使得電場遮蔽效應的下降，以致於起始電場的降低與均勻性顯著的提升，並且得到了當氧氣加氬氣電漿處理三分鐘後的結果，電場遮蔽效應能夠最有效的抑至，而起始電場 $E_{turn-on}=1.4V/\mu m$ 相較於未經過電漿後處理的起始電場 $E_{turn-on}=2.6V/\mu m$ 有很明顯的下降。

最後，在奈米碳管場發射的應用當中，低操作電壓是個很重要的因素，因此設計了一種溝槽式的奈米碳管三極結構，利用氧化層來取代傳統的絕緣間隙層，藉由控制奈米碳管的長度可以改變閘極到發射極的間距，實驗中固定陽極電壓為 800V，當閘極電壓從 0V 增加到 80V 時，場發射結果的亮度和均勻性都會大幅提升，並且論文中也利用了 SIMION 3D 軟體，模擬了不同閘極到發射極的間距與閘極對於均勻性的影響，因此這結構應用於奈米碳管場發射將是不錯的優勢。

Study on the Improvement of the Field Emission Characteristics of Carbon Nanotube Pillar Arrays with Different Pitch/Height Ratios Using Two-Step Thermal Chemical Vapor Deposition

Student: Yin-Chang Wei   Advisor: Dr. Bi-shiou Chiou

                                              Dr. Huang-Chung Cheng

Department of Electronics Engineering & Institute of Electronics

National Chiao Tung University

Abstract

Cost reduction and uniformly distribution of carbon nanotubes are the two main topics in the field emission display application. Thermal chemical vapor deposition (T-CVD) is regarded as one of the best candidates of the growth methods due to the merits of simplicity and cost efficiency in the fabrication and large scalability. Besides, we also find titanium (Ti) layer can improve the uniformity and strengthen the adherence between the CNTs and substrate for CNTs' growth. Therefore, co-deposited multilayer catalyst composed of Co and Ti on Al (Co-Ti/Al) is used in the T-CVD to grow pillar arrays of CNTs.

It has been reported that the field emission can be effectively enhanced for the aligned CNTs as the field emitters when the ratio of distance between neighboring nanotubes (R) to the height of each individual CNT (H) is about 2. Although the pillar arrays of CNTs with different optimum R/H ratios to get best field emission characteristics were investigated by the different results have been reported. In this thesis, three different inter-pillar distances(80μm、150μm and 250μm) are designed to find the optimum R/H ratio of pillar

arrays of CNTs by controlling the flow rate of carbon source and growth time precisely. The optimum R/H ratio is approaching to 2 when the inter-pillar distance is as larger as possible.CNT pillars probably behaves like an individual field emitter and has less field screening effect between pillars. The results show that when R/H ratios are 8, 4.7 and 3.2 for inter-pillar distance of 80μm、150μm and 250μm , respectively, ultra low turn-on field(1.78V/μm, 1.55V/μm and 1.53V/μm, respectively) is achieved and fluorescent uniformity can also be improved.

Two-step method is used to grow CNT pillar array until with 80 μm in the height successfully. CNT pillar array synthesized with two-step method revealed a good field emission performance of an emission current density of $10mA/cm^2$ at the electric field of 0.64 V/μm, and field emission characteristics show a very ultra-low turn-on field of 0.1V/μm at an emission current density 10 $\mu A/cm^2$ .As CNT pillar with one-step skill to two-step technique exhibit the I_G/I_D increases from 1.5 to 1.8 which confirms that the CNTs for the two-step one have a highly crystalline graphite structure as shown in TEM micrograph SEM show that thinner diameter about 24 nm is observed on the top of CNTs′ pillar. In addition to better crystallizing, the thinner diameter (i.e. high aspect ratio) also facilitate to the field emission characteristic.

Plasma post-treatment is one of the best ways to improve the field emission properties and fluorescent uniformity. In this thesis, we propose O_2 plus Cl_2 plasma post-treatment to the pillar array of CNTs and the experimental results reveal that the improved emission properties can be achieved by optimizing the density of CNTs and the defects on the nanotubes under proper plasma treatment conditions. The turn-on field is reduced from 2.6 V/μm to 1.4 V/μm and the fluorescent uniformity is also improved when the plasma post-treatment time is 3 min for the O_2 30sccm plus Cl_2 10sccm.

Finally, field emission triode is fabricated to reduce the operation voltage and improve emission uniformity by the beam spreading. The optimum parameters of the field emission

trides are obtained according to the simulations, the gate-to-emitter length is 1 μm. The experimental results show that the driving voltage is as low as 17 V. In the future, this structure is promising for the applications in a planar backlight because of the large-area uniformity and simple fabrication process with low cost.

誌　　謝

Contents

Chapter 1: Introductions

Chapter 2: Experiment

Chapter 3: Results and Discussion

Chapter 4: Summary and Conclusions

Table Lists

Chapter 1

Chapter 2

Chapter 3

Figure Captions

Chapter 1:

Chapter 2:

Chapter 3:

Chapter 1
Introduction

1.1 Overview of Vacuum Microelectronics

In 1991, carbon nanotubes (CNTs) were discovered by Sumio Iijima who observed hollow carbon nanotubes by TEM. Since the diameter of nanotubes is on the order of a few nanometers, and the length can be up to several micrometers, they have very height-to-diameter ratios. Carbon nanotubes are cylindrical carbon molecules with novel properties that make them potentially used in nano-electronics and optics etc. Due to the nanometer-sized , hollow center, and large surface area,CNTs are ideal field emission sources and used in vacuum microelectronics.

1.1.1 History of Vacuum Microelectronics

In 1948, vacuum tubes have been gradually replaced by solid state devices, which tiny volume, low cost, better reliability, and more power efficient transistors were invented by John Bardeen, Walter Bratain, and William Shockley [1.1].

But nowadays, there has been a growing interest in vacuum microelectronics. Some reasons for the increasing interest have to do with the superior theoretical electrical characteristics of the vacuum microelectronic devices over semiconductor devices. The so called vacuum microelectronic devices using the professional micro fabrication technology have been successfully fabricated and gave a new life to vacuum electronics due to great improvements on semiconductor manufacturing technology for the past decades.

"Vacuum state" devices have many superior advantages with respect to the present "solid state" devices, including radiation hardness, temperature insensitivity, and fast drift velocity. For example, there is negligible radiation effect in vacuum devices due to medium being damaged as the electrons fly in the vacuum [1.2].

Moreover, there is no medium for electrons fly in the vacuum, so there is no lattice scattering or bulk carrier generation/recombination. Therefore, the vacuum microelectronic devices can suffer to 500 ℃ or above as long as the structures of the vacuum devices do not destroyed and greatly reduced (nearly eliminated) temperature

sensitivity problem which usually comes along with semiconductor devices. Additionally, the saturation drift velocity is limited to less than 3×10^7 cm/s in all semiconductor due to scattering mechanism whereas the saturation drift velocity in vacuum is limited theoretically to 3×10^{10} cm/s and practically to about 6-9$\times10^8$ cm/s [1.3].

Table 1-1 shows the comparison between vacuum microelectronic and semiconductor devices. Vacuum electronics can be broadly separated into two categories: Thermionic emission or Field emission. The theory of field emission started in 1928, when R. H. Fowler and L. W. Nordheim published the first theory of electron field emission (Fowler- Nordheim theory) from metals using quantum mechanics [1.4]. The difference concerns the way electrons are emitted from the cathode. Thermionic emission relies on a heated electron emitter, or cathode. The cathode is heated up enough such that the electrons receive enough kinetic energy to leave the surface of the cathode. Field emission, unlike thermionic emission, is possible with a cold cathode. Field emission is a form of quantum tunneling in which electrons pass through a barrier in the presence of a high electric field. This phenomenon is highly dependent on both the properties of the material and the shape of the particular cathode, so that higher aspect ratios produce higher field emission currents. According to the Fowler-Nordheim theory, an applied electric field of approximately 10^3 V/m is needed for electrons to tunnel through the sufficiently narrow barrier [1.2]. To reach this high field at reasonable applied voltage, it is customary to machine the field emitters into protruding objects to take advantage of field enhancement.

It was not until 1968 when C. A. Spindt camp up with a fabrication method to create very small dimension metal cones that vacuum microelectronic triodes became possible [1.2]. **Fig.1-1** is a schematic diagram of the triode fabricated by Spindt [1.5]. From the late 1960s to the year 1990, Ivor Brodie, Henry F. Gray, and C. A. Spindt made many contributions to this field. Also, most of research was focused on the devices similar to the Spindt cathode during the past three decades.

In 1991, a group of research of the French company LETI CHEN reported a microtip display at the fourth International Vacuum Microelectronics Conference [1.6]. Their display was the first announcement of a practical vacuum microelectronic device. From then on, a great amount of researchers all over the world devoted themselves to this

interesting, challenging, and inventive field. Part of the work focused on fabricating very small radius silicon tip by utilizing modern VLSI technology [1.7-1.8]. Some of them increased the emission current by coating different metals, such as W, Mo, Ta, Pt etc., even diamond on field emission arrays [1.9-1.10]. Different device schemes also have been proposed to enhance the emission current density, stability, and reliability.

1.1.2 Theory Background

In quantum mechanical, electron field emission is a tunneling phenomenon of electrons extracted from the conductive solid surface, such as a metal or a semiconductor, where the surface electric field is extremely high.

If a sufficient electric field is applied on the emitter surface, electrons will be emitting through the surface potential barrier into vacuum, even under a very low temperature. On the other hand, thermionic emission is the hot electron emission under high temperature and low electric field. **Fig. 1-2(a)** demonstrates the band diagram of a metal-vacuum system.

Here W_0 is the energy difference between an electron at rest outside the metal and an electron at rest inside, whereas W_f is the energy difference between the Fermi level and the bottom of the conduction band. The work function ϕ is defined as $\phi = W_0 - W_f$. If an external bias is applied, vacuum energy level is reduced and the potential barrier at the surface becomes thinner as shown in **Fig. 1-2(b)**.
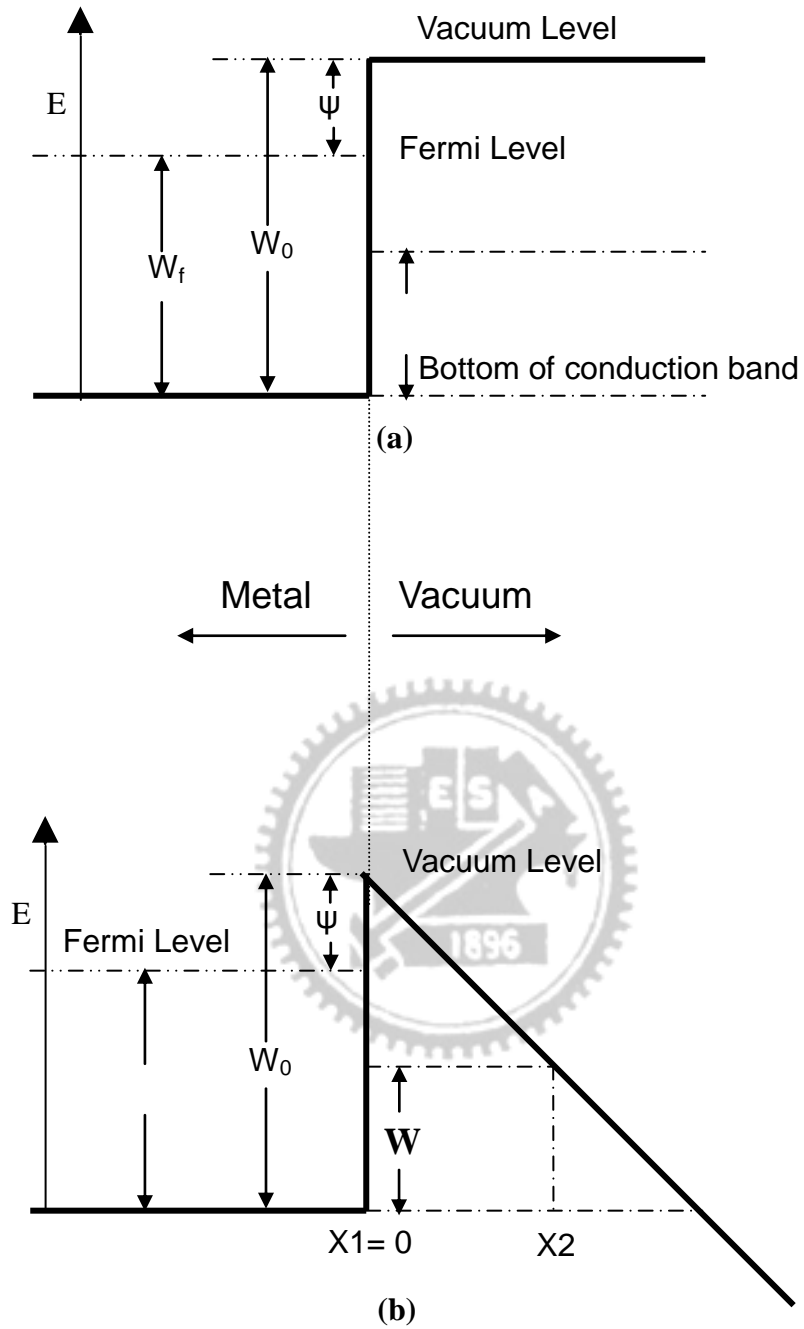
Figure 1-2 **Energy diagrams of vacuum-metal boundary: (a) without external electric field; and (b) with an external electric field.**

Then, an electron having energy "W" has a finite probability of tunneling through the surface barrier. Fowler and Nordheim derive the famous F-N equation (1.1) as follow [1.2]:

$$J = \frac{aE^2}{\phi t^2(y)} \exp[-b\phi^{\frac{3}{2}}v(y)/E],$$
(1-1)

where J is the current density (A/cm^2). E is the applied electric field (V/cm), ϕ is the work function (in eV), a = 1.56×10^{-6}, b = -6.831×10^{-7}, y = 3.79x10^{-4}×10^{-4}E$^{1/2}$/ϕ, t^2(y)~1.1 and v(y) can be approximated as [1.10]

$$v(y) = \cos(0.5\pi y),$$
(1-2)

or

$$v(y) = 0.95 - y^2.$$
(1-3)

Typically, the field emission current I is measured as a function of the applied voltage V. Substituting relationships of J = I/α and E = βV into **Eq.(1-1),** where α is the emitting area and β is the local field enhancement factor of the emitting surface, the following equation can be obtained

$$I = \frac{A\alpha\beta^2 V^2}{\phi t^2(y)} \exp[-bv(y)\frac{\phi^{\frac{3}{2}}}{\beta V}].$$
(1-4)

Then taking the log. form of **Eq. (1-4)** and v(y) ~ 1

$$\log(\frac{I}{V^2}) = \log[1.54\times10^{-6}\frac{\alpha\beta^2}{\phi t^2(y)}] - 2.97\times10^7(\frac{\phi^{3/2}v(y)}{\beta V}),$$
(1-5)

from **Eq. (1-5)**, the slope of a Fowler-Nordheim (F-N) plot is given by

$$S \equiv slope_{FN} = 2.97\times10^7(\frac{\phi^{\frac{3}{2}}}{\beta}),$$
(1-6)

The parameter β can be evaluated from the slope S of the measured F-N plot if the work function ϕ was known

$$\beta = -2.97 \times 10^7 \left(\frac{\phi^{\frac{3}{2}}}{S}\right) (\text{cm}^{-1}), \tag{1-7}$$

The emission area α can be subsequently extracted from a rearrangement of Eq.(1-5)

$$\alpha = \left(\frac{I}{V^2}\right) \frac{\phi}{1.4 \times 10^{-6} \beta^2} \exp\left(\frac{-9.89}{\sqrt{\phi}}\right) \exp\left(\frac{6.53 \times 10^7 \phi^{\frac{3}{2}}}{\beta V}\right) (\text{cm}^2). \tag{1-8}$$

For example, the electric field at the surface of a spherical emitter of radius r concentric with a spherical anode (or gate) of radius r+d can be represented analytically by

$$E = \frac{V}{r}\left(\frac{r+d}{d}\right), \tag{1-9}$$

Though a realistic electric field in the emitter tip is more complicated than above equation, we can multiply **Eq.(1-9)** by a geometric factor $\beta`$ to approximate the real condition.

$$E_{tip} \equiv \text{function of (r,d)} = \beta` \frac{V}{r}\left(\frac{r+d}{d}\right), \tag{1-10}$$

where r is the tip radius of emitter tip, d is the emitter-anode(gate) distance and $\beta`$ is a geometric correction factor [1.11].

For a very sharp conical tip emitter, where d >> r, E_{tip} approaches to $\beta`(V/r)$. And for r>>d, $E_{tip}$ approaches to $\beta`(V/d)$ which is the solution for a parallel-plate capacitor and for a diode operation in a small anode-to-cathode spacing.

As the gated FEA with very sharp tip radius, **Eq. (1-10)** can be approximated as:

$$E_{tip} = \beta`(V/r), \tag{1-11}.$$

Combining $E = \beta V$ and **Eq. (1-11)**, we can obtain the relationship:

$$E_{tip} = \beta V = \beta`(V/r), \text{ and } \beta` = \beta r., \tag{1-12}$$

The tip radius r is usually in the range from a few nm to 50 nm, corresponding to the parameter $\beta`$ ranging from 10^{-1} to 10^{-2}.

6

Besides, transconductance g_m of a field emission device is defined as the change in anode current due to the change in gate voltage [1.1].

$$g_m = \frac{\partial I_C}{\partial V_g} |_{Vc},\tag{1-13}$$

Transconductance of a FED is a figure of merit that gives as an indication of the amount of current charge that can be accomplished by a given change in grid voltage. The transconductance can be increased by using multiple tips or by decreasing the gate-to-cathode spacing for a given anode-to-cathode spacing.

The following approaches may therefore be taken to reduce the operating voltage of the field emission devices according to the equations above mentioned:

    a. Narrow the cone angle for increasing β

    b. Reproducibly sharpen the tips to the atomic level for increasing β

    c. Choose the tip material which has the lower work function (ϕ)

    d. Reduce the gate-opening diameter for increasing β.

1.2 Applications of Vacuum Microelectronic Devices

Due to the superior properties of vacuum microelectronic devices, potential applications include high brightness flat-panel display [1.12-1.16], high efficiency microwave amplifier and generator [1.17-1.19], ultra-fast computer, intense electron/ion sources [1.20-1.21], scanning electron microscopy, electron beam lithography, micro-sensor [1.22-1.23], temperature insensitive electronics, and radiation hardness analog and digital circuits

1.2.1 Vacuum Microelectronic Devices for Electronic Circuits

Either vacuum or solid-state devices can generate power at frequency in the GHz range. Solid-state devices, such as impact avalanche transit time (IMPATT) diodes, Si

bipolar transistors, and GaAs FETs [1.24], are typically used in the lower power (up to 10 W) and frequency (up to 10 GHz) range. Vacuum devices still remain the only technology available for high power and high frequency applications. These devices include traditional multi-terminal vacuum tubes, like triodes, pentodes, and beam power tubes, and distributed-interaction devices, such as traveling wave tubes (TWTs), klystrons, backward-wave oscillators (BWOs).

The performance of FEAs in conventionally modulated power tubes, like TWT, is determined primarily by their emission current and current density capability. On the other hand, application of FEAs in the microwave tubes in which modulation of the beam is accomplished via modulation of the emission current at source, such as capacitance and transconductance. Successful operation of a gated FEA in a 10 GHz TWT amplifier with conventional modulation of electron beam has been demonstrated by NEC Corporation of Japan [1.25]. The amplifier employed a modified Spindt-type Mo cathode with circular emission area of 840 μm in diameter. The modified cathode structure incorporated a resistive poly-Si layer as a current limiting element. The emission current from the cathode was 58.6 mA. The prototype TWT could operate at 10.5 GHz with the output power of 27.5 W and the gain of 19.5 dB. The bandwidth of the tube was greater than 3 GHz. The prototype was operated for 250 h.

1.2.2 Field Emission Displays

Among wide range applications of the vacuum microelectronics, the first commercial product could be the field emission flat-panel display. The field emission fluorescent display is basically a thin cathode ray tube (CRT), which was first proposed by SRI International and later demonstrated by LETI [1.6].

Various kinds of flat-panel displays, such as liquid crystal display (LCD), electroluminescent display (EL), vacuum fluorescent display (VFD), plasma display panel (PDP), and light emitting display (LED), are developed for the better characteristics of small volume, light weight, and low power consumption. LCDs have become the most popular flat panel displays, however, LCDs have some drawbacks, such as poor viewing angle, temperature sensitivity and low brightness. As a result, some opportunities still exist and waiting for the solutions from other flat panel displays such as FED.

FED features all the pros of the CRTs in image quality and is flat and small volume. The schematic comparisons are revealed in **Fig. 1-3** [1.24]. The operation of CRTs involves deflection of the beam in such a way that the electron spot scans the screen line-by-line. In FEDs, multiple electron beams are generated from the field emission cathode and no scanning of beams is required. The cathode is a part of the panel substrate consists of an X-Y electrically addressable matrix of field emission arrays (FEAs). Each FEA is located at the intersection of a row and a column conductor, with the row conductor serving as the gate electrode and the column conductor as the emitter base. The locations where the rows and columns intersect define a pixel. The pixel area and number of tips are determined by the desired resolution and luminance of the **d**isplay. Typically, each pixel contains an FEA of 4-5000 tips. The emission current required for a pixel varies from 0.1 to 10 μA, depending on the factors such as the luminance of the display, phosphor efficiency and the anode voltage.

Compared to the active matrix LCDs and PDPs, FEDs are energy efficient and could provide a flat panel technology that features less power consumption. They can also be cheaper to make, as they have fewer total components. Moreover, FEDs could generate three times the brightness with wilder viewing angle at the same power level. Full color FEDs have been developed by various research groups from different aspects such as Motorola, PixTech, Futaba, Sony/Candescent, Samsung, and Canon-Toshiba are presently engaged in commercially exploiting FEDs. the products of above mentioned companies are shown in Fig. 1-4.

1.2.3 Cathode Structure and Materials for Field Emission Displays

Field emission display is one of the most promising emissive type flat-panel displays, which can overcome the drawbacks of TFT-LCD, such as poor viewing angle, temperature sensitivity, low contrast and low brightness. This section introduces some novel cathode structures and synthesizes these novel emitter materials for FED operations

1.2.3.1 Spindt-type Field Emitters

The "Spindt" cathode was first proposed by C. A. Spindt in 1968 [1.25]. The scanning electron microscope (SEM) image of a spindt type field emission triode has

been shown in **Fig. 1-1** agian. It was first invented by Spindt of SRI and improved for the electron source of high-speed switching devices or microwave devices [1.2]. In 1970s, Meyer of LETI applied Spindt-typed emitters for a display and introduce a resistive layer as the feedback resistance to stabilizing the field emission from Spindt-type emitters [1.26].

The structure of Spindt-type FED includes a substrate, a cathode electrode of an electron emission unit formed thereon having a substantially conical shape, and a gate electrode of a lead-out electrode stacked on a substrate around the cathode electrode having an insulating layer. In the Spindt type FED a voltage is applied between the cathode electrode and the gate electrode in a vacuum to thereby produce a high electric field. As a result, electrons are emitted from a tip end of the cathode electrode through the electron emission mechanism in an electric field. In addition, the Spindt-type FED has a conical electron emission portion formed on a cathode electrode. It higher electron drawing efficiency since the electron emission portion is arranged in the vicinity of the center of the gate electrode where the electric field is most concentrated, and the directivity of electron emission is regular.

The merits of the Spindt-type field emitters are summarized as following: (1) High emission current efficiency, more than 98 % anode current to cathode current can be achieved for the symmetric structure of Spindt tip and the gate hole, the lateral electric field to the metal tip can be cancelled out. (2) The fabrication is self-aligned, easy process; uniform field emission arrays can be fabricated easily. Some research groups have successfully fabricated commercial FED products based on Spindt-type field emitters such as motorola, Pixtech, Futaba and Sony/Candesent.[1.27], the products of above mentioned companies are shown in **Fig. 1-4**.

However, there are some drawbacks of Spindt-type field emitters when fabricating Spindt-type FED such as (1) High gate driving voltage required; for a Spindt-type field emission triode with 4 μm gate aperture, the driving voltage is typically more than 60 V, which results in the high cost of the driving circuits. To reduce the gate driving voltage, frontier lithography technologies such as E beam lithography must be applied to reduce the gate aperture to the sub-micron level. (2) The emission property degrades for the chemically instable of the metal tips. (3) Huge, expensive high vacuum deposition system

required during fabricating large area Spindt-type FED.

1.2.3.2 Silicon Tip Field Emitters

An alternative approach to fabricate tip type field emitters is to fabricate the Si tip field emitters based on the semiconductor fabricating process. **Figure 1-5** depicts the SEM micrographs of Si tips array, Si tip field emission triodes array formed by chemical mechanical polishing (CMP) [1.28] and double gate of Si field emitter arrays [1.29]. Symmetric device structure and similar advantages with Spindt-type field emitters can be obtained. However, high temperature oxidation sharpening process prohibits Si tip from large area fabrication

1.2.3.3 Surface Conduction Electron Emitters

A surface conduction electron emitter (SCE) display is a flat panel display technology that uses surface conduction electron emitters for every individual display pixel. The surface conduction emitter emits electrons that excite a phosphor coating on the display panel, the same basic concept found in traditional CRT televisions. The key technology to the electron emitters begins with the creation of an extremely narrow slits (~ several nanometers) between two electric poles in thin film of PdO (Palladium Oxide). Electrons are emitted from one side of the slit when approximately 10 V of electricity are applied. Some of these electrons are scattered at the other side of the silt and accelerated by the voltage (approximately 10 kV) applied between the glass substrates; causing light to be emitted when they collide with the phosphor-coated glass plate. The PdO film is coated by inject printing or screen-printing technology and this is a low cost process. This means that SEDs use small cathode ray tubes behind every single pixel (instead of one tube for the whole display) and can combine the slim form factor of LCDs and plasma displays with the superior viewing angles, contrast, black levels, color definition and pixel response time of CRTs. The major problem of SED is that the efficiency is still low and the power consumption will be very high. Fig. 1-6 shows the SEM image of SCE cathode array, structure and a 36-inch display of SED [1.30][1.31].

The research of SED was began by Canon in 1986, and in 2004, Toshiba and Canon announced a joint development agreement originally targeting commercial production of

SEDs. In October 2006, Toshiba's president announced the company plans to begin full production of 55" SED TVs in 2007. In December 2006, Toshiba President and Chief Executive Atsutoshi Nishida said Toshiba is on track to mass-produce SED TV sets in cooperation with Canon by 2008.

1.2.3.4 Carbon and Nano-sized Emitters

So-called carbon nanotubes (CNTs) is the nano-sized and carbon emitters, is known to be useful for providing electron emission in field emission devices, such as cold cathodes that are used in a field emission display. Although Spindt-type emitters are generally used for FEDs, they still have a problem in that the life span of micro-tips is shortened due to atmospheric gases or a non-uniform field during a field emission operation. Moreover, the work function of the conventional metal emitters is too high to decrease a driving voltage for field emission. To overcome the problem, CNTs which have a substantially high aspect ratio, excellent durability due to their structure and excellent electron conductivity have been instead of Spindt-type emitters for field emission. CNTs are are anticipated to be an ideal electron emission source since they feature a low work function, the resultant electron emission source can be driven by applying low voltages, and the method of fabricating the same is not complicated. They will thereby offer advantages to realize a large size panel display in terms of view angle, definition, power consumption, and temperature stability.

1.3 Field Emission Properties of Carbon Nanotubes

Since the discovery of carbon nanotubes (CNTs) by Iijima in 1991, [1.32] CNTs have attracted considerable interests because of their unique physical properties and many potential applications [1.33]. CNTs have numerous potential applications in nanoelectronics, nanometer-scale structural materials, hydrogen storage, field-emission devices, and so on. Among these applications, CNTs seem to be very promising as electron emitters for field-emission displays (FEDs).

1.3.1 The Synthesis Methods of Carbon Nanotubes

Carbon nanotubes (CNTs) have been extensively investigated for the synthesis using arc discharge, laser vaporization, pyrolysis, solar energy, and plasma-enhanced chemical vapor deposition (CVD), for its unique physical and chemical properties and for applications to nanoscale devices. However, common methods of CNT synthesis include: (1) arc-discharge [1.34], (2) laser ablation [1.35], (3) thermal CVD [1.36-1.38], and (4) plasma enhanced CVD [1.39][1.40].

The laser ablation can synthesize pure carbon nanotubes in high fabrication temperature, but large scale display panel can not be fabricated in the high fabrication temperature above the melting point of glass substrate. The arc discharge can synthesize carbon nanotubes in shorter fabrication times, but it has some issues, such as (1) poor purity, (2) hard to control growth orientations of carbon nanotubes, and (3) poor emission uniformity.

Compared to laser ablation and arc discharge, using CVD for carbon nanotube growth has some features, such as (1) high purity carbon nanotubes, (2) selective growth only for catalyst metal, (3) controlling growth direction, and (4) much suitable to semiconductor fabrication procedure. However, with the display technology trend, it is the time for large panel display. We need to synthesize carbon nanotubes using CVDs on large panel substrates. For this reason, carbon nanotube growth at low temperatures is unavoidable, but the purity of carbon nanotubes at low temperatures is poor. So, we still try some methods to increase growth rates at low temperatures, such as (1) multilayer catalysts, (2) plasma CVDs, (3) post-treatment, and so on.

1.3.2 Structure and Properties of Carbon Nanotubes

CNTs can be divided into two categories. The first is called multiwalled carbon nanotubes (MWNTs). MWNTs are close to hollow graphite fibers [1.41], except that they have a much higher degree of structural perfection. They are made of sheets of carbon atoms with a cylindrical shape and generally consist of co-axially arranged 2 to 20 cylinders「**Fig. 1-7(b)**」. The interlayer spacing in MWNT ($d_{(002)} = 0.34$ nm) is slightly larger than that in single crystal graphite ($d_{(002)} = 0.335$ nm) [1.42]. This is attributed to a combination of tubule curvature and van der Waals force interactions between successive garphene layers. The second type of the nanotube is made up of just a single layer of

carbon atoms. These nanotubes are called the single-walled nanotubes (SWNTs) and possess good uniformity in diameter about 1.2 nm **Fig.**[**1-7(a)**]. They are close to fullerenes in size and have a single-layer cylinder extending from end to end [1.43][1.44].

Most experimentally observed CNTs are multi-walled structures with outer most shell diameters exceeding 10 nm. Since current conduction in a MWNT is known to be mostly confined to the outermost single-walled nanotube and since band gap of a SWCNT varies inversely with its diameter, MWNTs are metallic in nature. SWNTs can be either metallic or semiconducting depending on the way the roll-up of the graphene sheet occurs - an aspect termed as Chirality, and if all the roll-up types are realized with equal probability, 1/3 of the SWNTs end up being metallic and 2/3 semiconducting. The structure of a SWNT can be conceptualized by wrapping a one-atom-thick layer of graphite called graphene into a seamless cylinder. The way of the graphene sheet is wrapped is represented by a pair of indices (n,m) called the chiral vector. The integers n and m denote the number of unit vectors along two directions in the honeycomb crystal lattice of graphene. If $m=0$, the nanotubes are called "zigzag". If $n=m$, the nanotubes are called "armchair". Otherwise, they are called "chiral". **Fig. 1-8** depicts these structures of a SWNT [1.45] [1.46].

CNTs have been attracting much attention for their unique physical and chemical properties such as high mechanical strength, chemical stability, high aspect ratio, super-therml conductivity, and electron emission properties [1.47] [1.48]. CNTs could be one of the strongest and stiffest materials known, in terms of tensile strength and elastic modulus respectively. This strength results from the covalent sp^2 bonds formed between the individual carbon atoms. The highest tensile strength an individual multi-walled carbon nanotube has been tested to be is 63 GPa [1.49]. Under excessive tensile strain, the tubes will undergo plastic deformation, which means the deformation is permanent. This deformation begins at strains of approximately 5% and can increase the maximum strain the tube undergoes before fracture by releasing strain energy. For the thermal conductivity of CNTs , it is predicted that carbon nanotubes will be able to transmit up to 6000 watts per meter per kelvin at room temperature; compare this to copper, a metal well-known for its good thermal conductivity, which only transmits 385 W/m/K. The temperature stability of carbon nanotubes is estimated to be up to 2800 degrees Celsius in

vacuum and about 750 degrees Celsius in air [1.50].

1.3.3 Potential Applications of Carbon Nanotubes

Since the discovery of CNTs in 1991, CNTs had attracted much attention for their unique physical and chemical properties. Their extensively potential applications lead them to become a super star of nano technology, which cover: (1) Chemical sensor [1.51], (2) IR detector, (3) Nano-conducting Wire, (4) Vehicles for Hydrogen Storage [1.52], (5) Field Effect Transistor [1.53], (6) Field Emission Display (FED), (7) Probe of AFM and etc.

In the wide-ranging applications of CNTs, FED arouses researchers' interest particularly. In virtue of the superior field emission characteristics, CNTs are applied to the emitting source of cold cathode. The advantages of FED are its low response time, wide view angle, high brightness, high working temperature range and well combination with mature phosphor technology. However, a major problem needs to be solved in this field. It is not allowed to effectively analyze CNTs on a flat panel at relatively lower temperature (<500°C) and this barrier restriction obstructs the development of CNT-FED so far. The products of CNTs FED is shown in **Fig. 1-9**.

1.4 Motivation

For technological commercialization of products today, the cost is the most important issue. The main concern for manufactures is cost down. It is worth noted that lower cost will provide more advantages for a product. In our research of CNT field-emission backlight unit (FE-BLU), we ensure that if the cost of field-emission backlight unit (FE-BLU) continuously decreases, it can even replace the traditional light bulbs or light-emitting diode (LED) in the future. So the following motivation will focus on decreasing the cost and increasing the quality of CNT FE-BLU.

Nowadays, the backlight unit of liquid crystal display (LCD) is CCFL, but CCFL backlight system contains several components for providing planar and uniformity illumination. The following are designs of LED-BLU:

1.   Reflection sheet is used to reflect the light beam of wrong direction from the

lamp.

2. Light guide panel is used to transform spot or linear light source to planar light source.

3. The prism sheet and diffusion sheet are playing the crucial roles in spreading the brightness.

Fig. 1-10 shows the complex system of LED backlight unit on LCD below [1.55] [1.56]. The uniformity become better due to the uniformity-assisted layer of backlight system, but thickness and cost increase obviously. For a LCD, the cost of backlight system on the total cost is about 14% for 17inch TFT-LCD, and 21% for 32inch TFT-LCD, which are shown in **Fig. 1-11** [1.57]. As this result, we could easily to make a prediction that we will require more cost on backlight system for a larger size TFT-LCD.

Many relative researches for the synthesis or the field-emission characteristics improvements of the carbon nanotubes-based field-emission devices have been reported so far. However, only few of them discussed the problems of reliability and uniformity in the field-emission devices. For the purpose of applications, the issues of reliability and uniformity are two of the most critical keys for the commercialization of field-emission displays and back-light units. Therefore, we focus on the issue of uniformity of the carbon nanotubes-based field-emission devices. Furthermore, the increase of emission current density and power efficiency of the carbon nanotubes-based field-emission devices are also discussed here (in Chapter 2 and Chapter 3).

1.4.1 Uniformity

Uniformity is the most difficult challenge for the applications of field-emission displays and back-light units, especially for the displays with image size. Due to the difficulty of controlling the diameter, length, direction, and distribution of the carbon nanotubes, it is still hard to obtain a uniform emission current from the carbon nanotubes-based field-emission devices. In Chapter 2 Experiment A, man-made emitters are defined by lithography to control the morphologies and distribution of the emitters. In Chapter 2 Experiment C, try to improve uniformity of field-emission displays by plasma post-treatment.In Chapter 2 Experiment D, triode emitters are defined by lithography to control the morphologies and gate-control distribution of the emitters precisely.

1.5 Thesis Organization

The overview of vacuum microelectronics, field emission display and basic principles of field emission theory was described in chapter 1.

The experimental procedures were revealed in chapter 2. First, we utilize three types of different inter-pillar distance patterns, such as 80, 150 and 250 μm then use them on silicon substrate to compare their morphology and discussion their uniformity. We discussed the effect of R/H ratios of CNTs pillars. In the part, we investigated and found the relations of R/H ratios (inter-pillar spacing (R)/pillar height (H) ratios) to obtain the optimization and perimeter of the field emission characteristics. We also post-treat CNT pillar array by plasma bombardment and find the optimal condition of plasma. Finally, try to enhance emission electron from triode-pillar array by gate voltage.

Results and discussion were summarized in chapter 3. then, we accomplished many important results including, (1) SEM images, (2) TEM images, (3) AFM images, (4) Raman analysis, (5) EDS analysis, and (7) Field Emission Measurement.

Finally, the summaries and conclusions are provided in chapter 4.
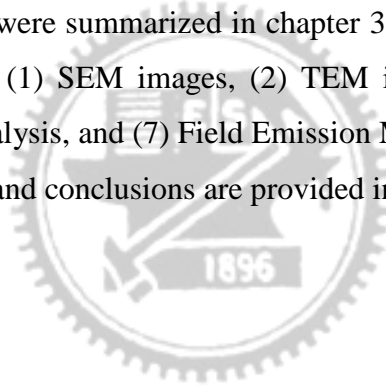
Table 1-1
Comparison between vacuum microelectronics and solid-state electronics.

Items	Solid State Microelectronics	Vacuum Microelectronics
Current Density	$10^4 - 10^5$ (A/cm^2)	similar
Turn-on Voltage	0.1 – 0.7 V	5 – 300 V
Structure	solid/solid interface	solid/vacuum interface
Electron Transport	in solid	in vacuum
Electron Velocity	3×10^7 (cm/sec)	3×10^{10} (cm/sec)
Flicker Noise	due to interface	due to emission
Thermal & Short Noise	comparable	comparable
Electron Energy	< 0.3 eV	a few to 1000 eV
Cut-off Frequency	< 20 GHz (Si) & 100 GHz (GaAs)	< 100 – 1000 GHz
Power	small – medium	medium – large
Radiation Hardness	poor	excellent
Temperature Effect	-30 – 50 °C	< 500 °C
Fabrication & Materials	well established (Si) & fairly well (GaAs)	not well established
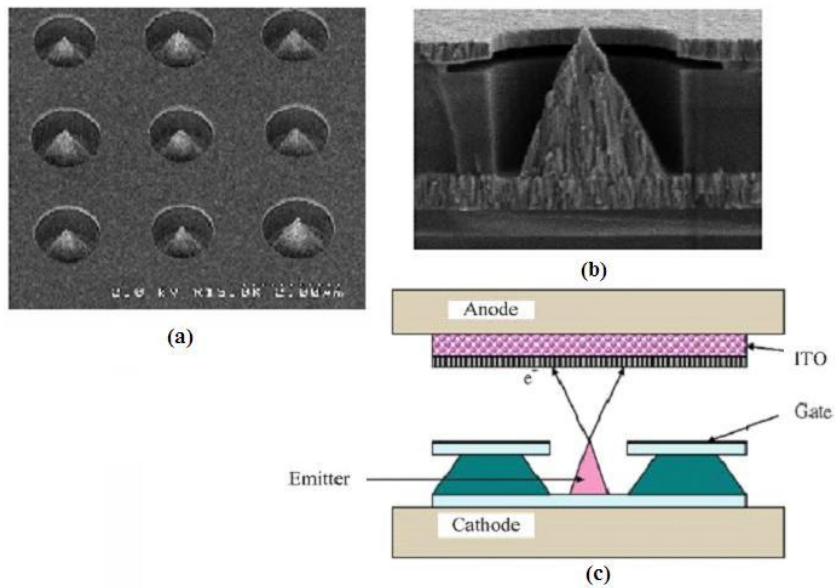
Figure 1-1 The SEM micrograph of (a) Spindt type triodes array, (b) Spindt type

field emission triode, (c) Emitting way of spindt type triode. [1.5]
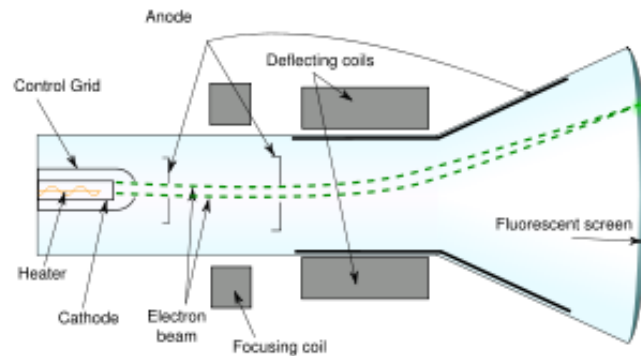
(a)
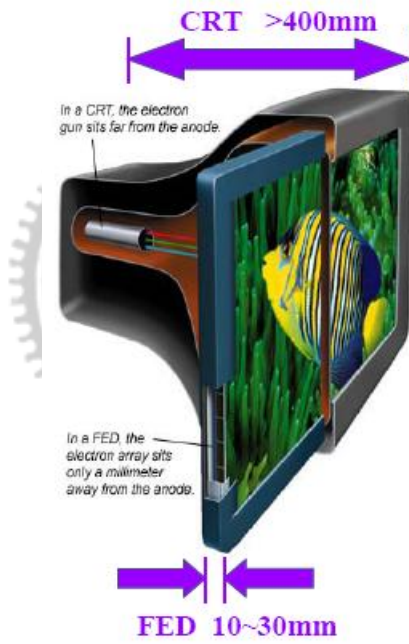
(b)

Figure 1-3 The schematic diagram of (a) conventional CRT and (b) comparison between CRT and FED. [1.24].

(a)

(b)

(c)

(d)

(e)

(f)
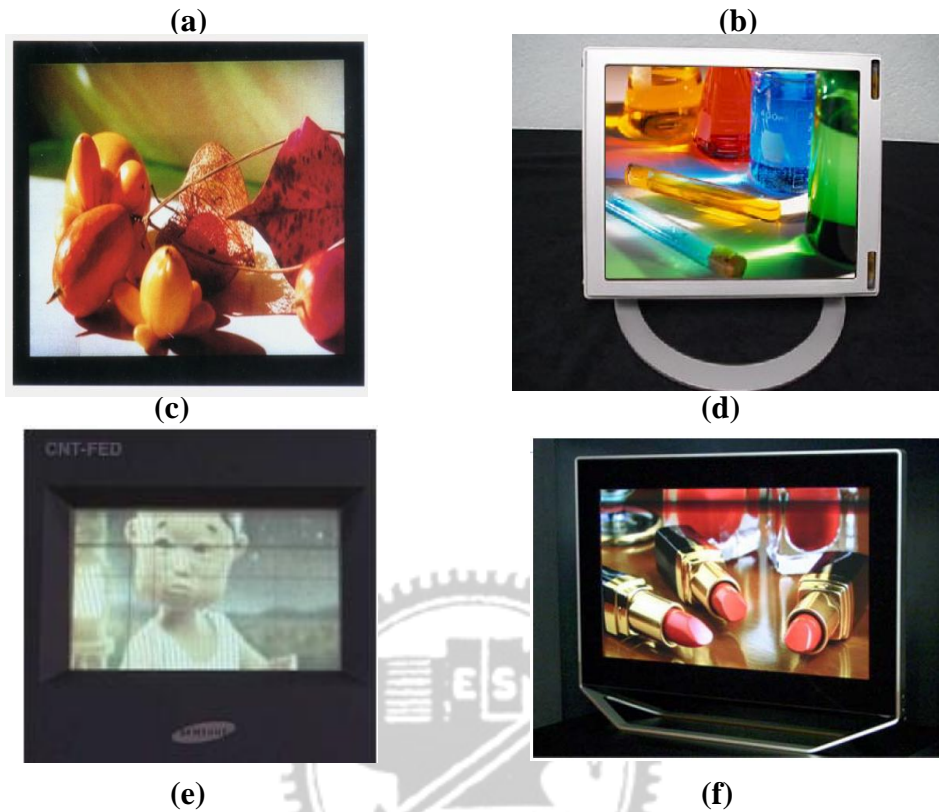
Figure 1-4 The full color FED products: (a) Motorola 5.6" color FED based on Spindt-type , (b) Pixtech 5.6" color FED based on Spindt-type, (c) Futaba 7" color FED based on Spindt-type, (d) Sony/Candescent 13.2" color FED based on Spindt-type, (e) Samsung 32" under-gate CNT-FED, and (f) Canon-Toshiba 36" SED-TV.

15.0kV X10.3K 3.00μm
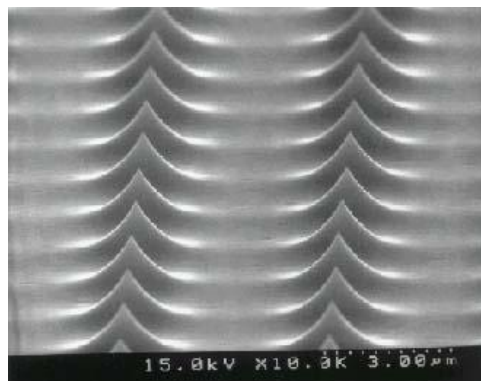
(a)
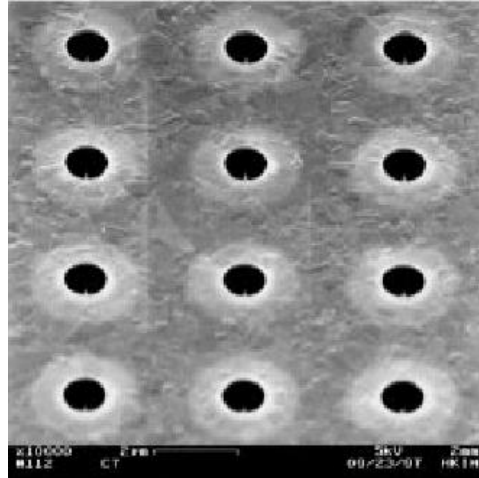
(b)

Figure 1-5 (a) Si tip formed by isotropic etching and (b) Si tip field emission triodes array formed by CMP [1.28] [1.29]

(a)

t

(b)

(c)
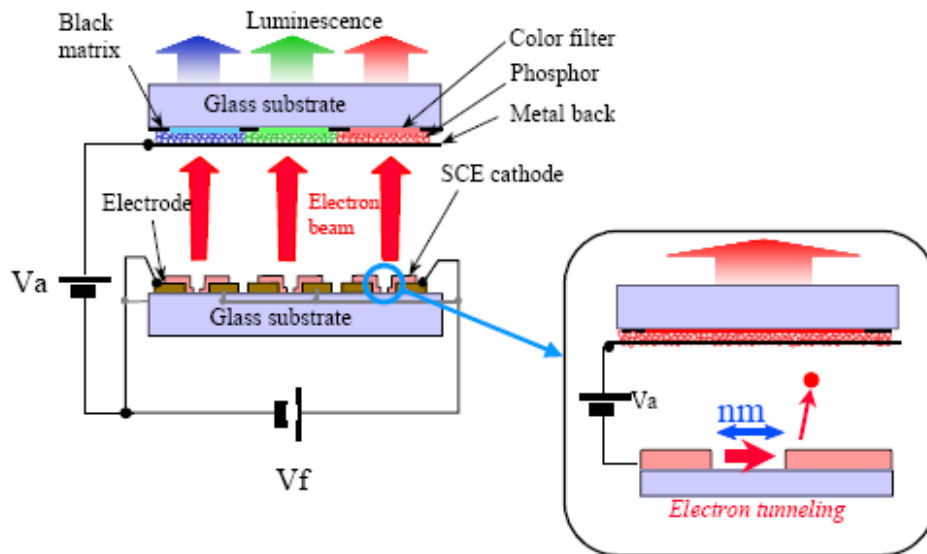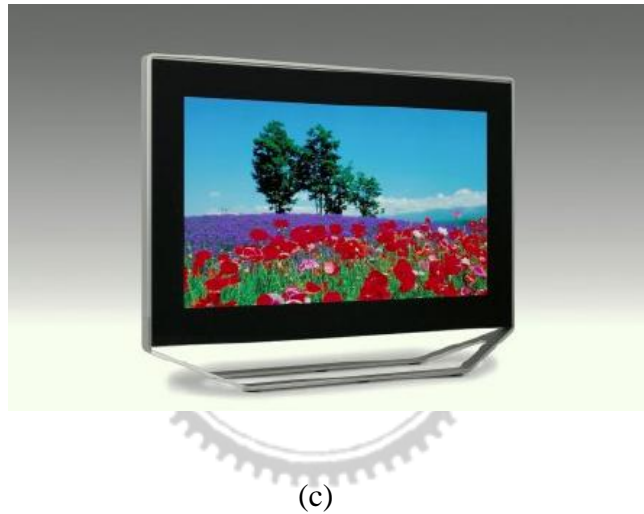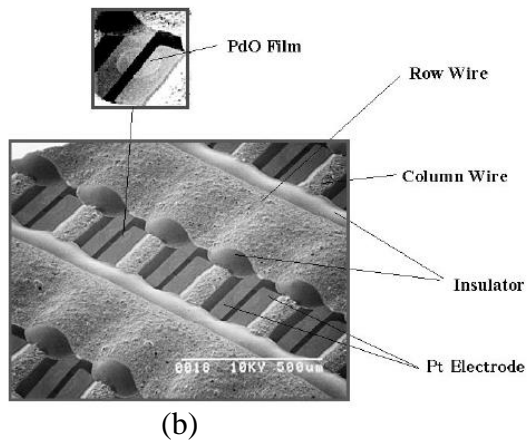
Figure 1-6 (a) The structure of SED, (b) SEM image of SCE cathode array, and (c) A 36-inch prototype of surface conduction electron emitter display. [1.30] [1.31]

(a)
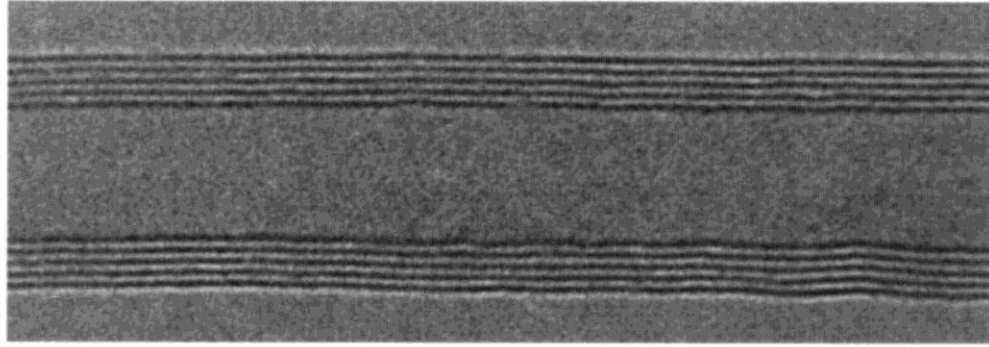
(b)

Figure 1-7 High-resolution transmission electron microscopy images of (a) SWNTs, and (b) MWNTs. Every layer in the image (fringe) corresponds to the edges of each cylinder in the nanotube assembly [1.42].
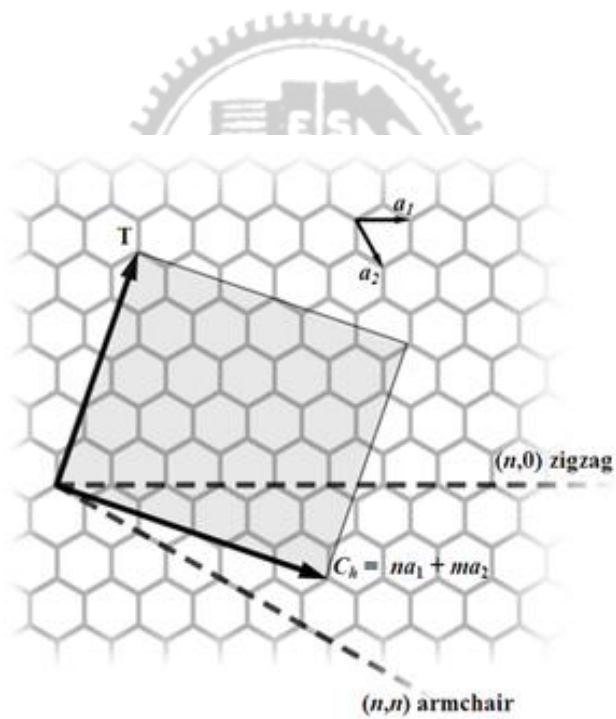
(a)
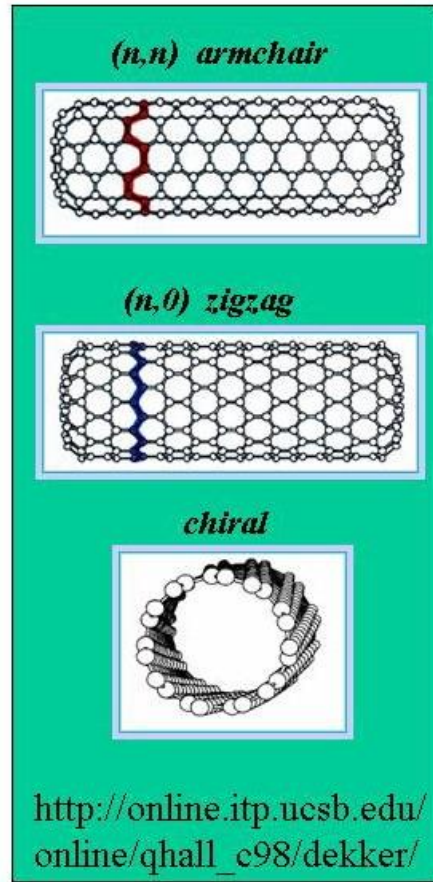
(b)

Figure 1-8 Molecular models of SWNTs with (a) chiral vector (b) the categories of the configuration [1.45] [1.46].
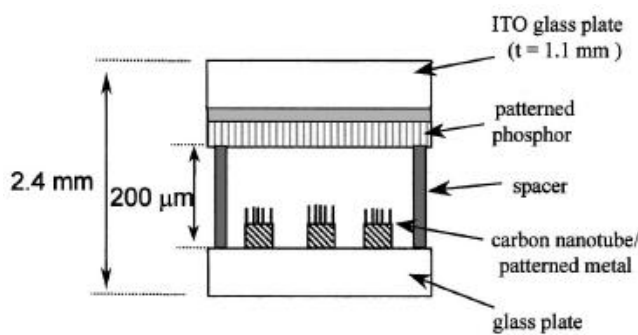
(a)
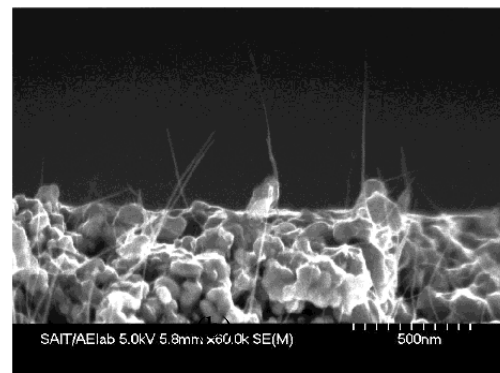
(b)

(c)
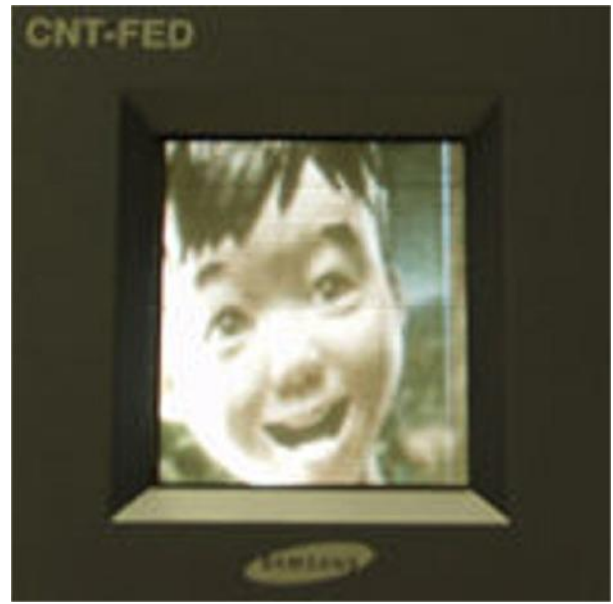
(d)

Figure 1-9 (a) Schematic structure of the fully sealed 128 lines matrix-addressable CNT-FED. (b) Cross section SEM image of CNT cathode from Samsung's FED.(c) A 4.5-inch FED from Samsung, the emitting image of fully sealed SWNT-FED at color mode with red, green, and blue phosphor columns. (d) A prototype of 5" CNT flat panel display by Samsung. [1.54]

■ DIAART   Internal structure of C Series model

■ DIAART   Internal structure of Y – type model
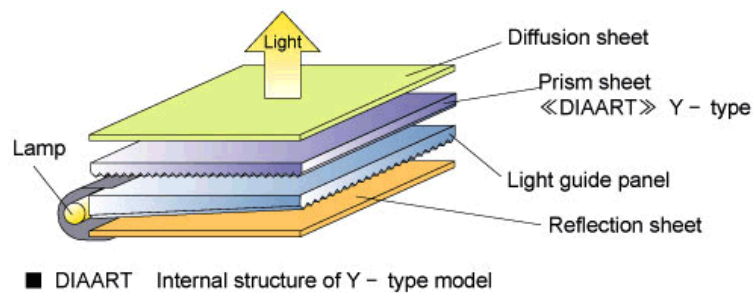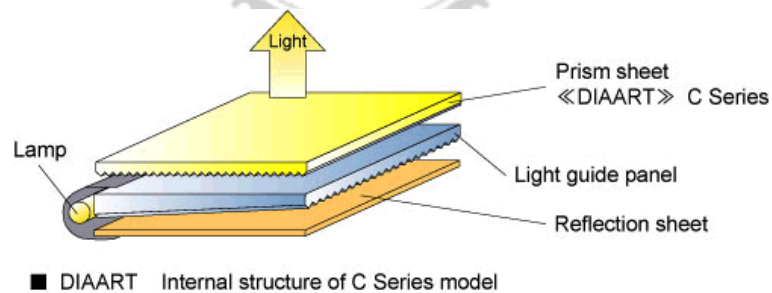
(a)
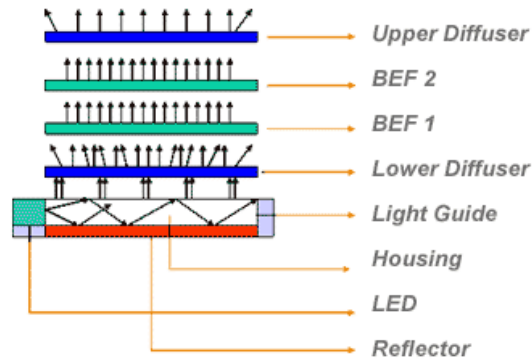
(b)
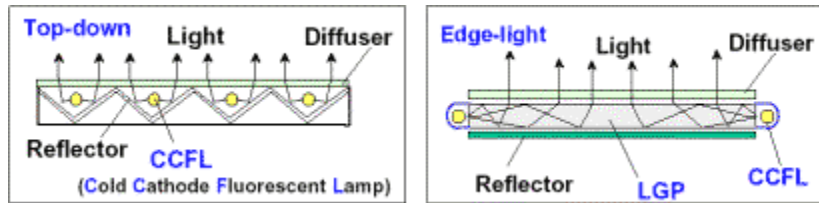
(c)   (d)

Fig 1.10 The profile of LED backlight system (a) shows names of every sheet. [1.55] (b) direction of light beams in backlight system. (c) bottom lighting type of backlight system. (d) edge lighting type of backlight system. [1.56]
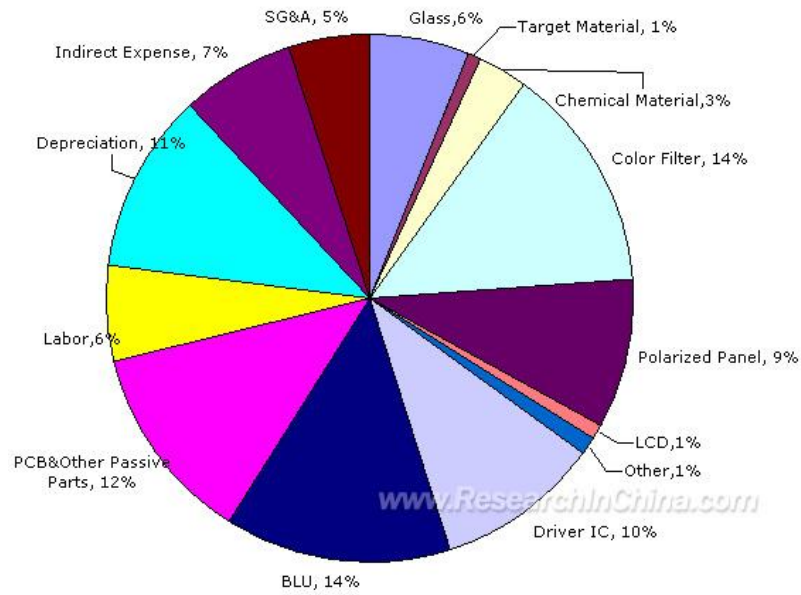
(a)
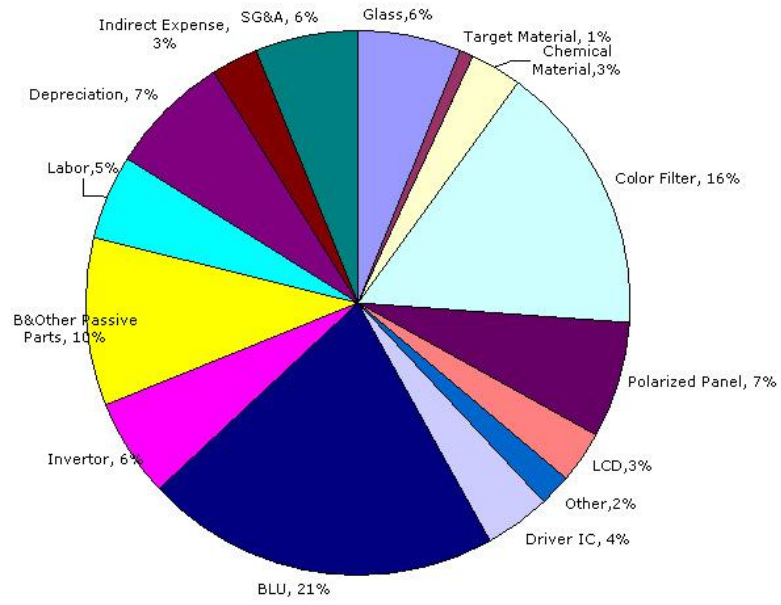
(b)

Fig 1.11 The cost of the overall (a) 17inch (b) 32inch TFT-LCD [1.57].
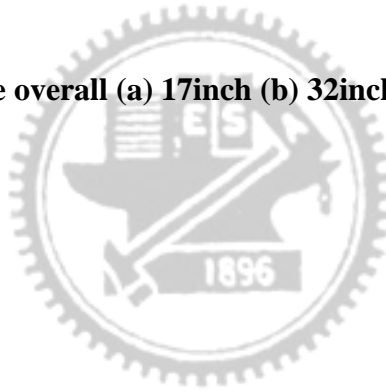
Chapter 2
Experimental Procedures

2.1 Introduction

Carbon nanotubes (CNTs) are one of the field-emission materials because of their high geometric aspect ratio, small tip radius of curvature, high electrical conductivity, high mechanical strength, and chemical stability[2.1]. So far, the usefulness of electron sources using a CNT emitter as a cold cathode has been demonstrated for vacuum electronic devices such as field-emission displays[2.2][2.3], backlight sources[2.4], and x-ray tubes[2.5]. For such device applications, CNT emitters are required to possess a low driving voltage and durability for a long lifetime. In recent years, CNT emitters have been fabricated by two main methods: chemical vapor deposition (CVD)[2.6] and screen printing[2.4]. In both methods, it is important to control the length and the inter-tube distance of CNTs to reduce the screening effect in adjacent CNTs[2.7] shown in **Fig.2.1**. It has been reported that field emission can effectively enhanced for aligned CNTs as field emitters when the ratio of the inter-tube distance to the height of each CNT is about 2[2.8], but, in our research, the ratio of the inter-tube distance to the height of each CNT is not approximately 2. However, the reduction of the field screening effect, and the optimal ratio of the inter-tube distance to the height which are components of an efficient field emitter, has not been sufficiently investigated.

Reports have stated that field emission is dependent on the direct parameters of CNTs such as the number of walls, the shape and structure of the tips, and indirect parameters such as surface treatment and CNT-alignment methods on a substrate. Recent works on CNT field emission are focused on several post-treatment methods and new growth method of CNTs to improve the uniformity and density of the electron emission site. Plasma surface treatment has been used as one of the post-treatment methods to improve the field emission properties of carbon-based materials. For example, hydrogen, oxygen, and argon plasma are all found to improve the field emission properties of carbon-based material films by changing the atomic configurations on the surface.

In our research, we used a method of transforming the CNT pillar arrays into a ring

edge shaped emitter array by plasma of O_2 and Cl_2 gases. The pillar arrays have been fabricated on a patterned silicon wafer by thermal chemical vapor deposition technique (T-CVD). The ring edge formed after the plasma treatment by high density plasma reactive ion etching system (HDP-RIE) shown in **Fig.2.2** [2.9], of almost perfect shape, are found to be excellent field emitters. The improved emission current density is attributed to enhancement in the field at the tip of the emitter, reduction in screening effect, and increase in the aspect ratio.

Triode type CNT field emitters have some advantages such as field emission at a lower electric field, the uniformity and stability of field emission, easy adjustment, and high-quality screen, compared with diode type CNT emitters in display applications of CNTs. In order to fabricate the triode type CNT field emitters, it is desirable to selectively synthesize vertically aligned CNTs on substrates with patterned trench structure. Vertical alignment of CNTs on the substrate is crucial for the practical applications of CNTs as field emitters. The trench structure can permit a favorable condition for a vertically aligned growth of CNT emitters. In our research, we got a selective growth of CNTs has been carried out by thermal chemical vapor deposition (T-CVD) on plat substrates, while there were rare research on the vertically aligned growth of CNTs in triode type trench structure by chemical vapor deposition (CVD) method.

The application in industry recently, the schematic of a typical BLU is shown in **Fig.2-3** [2.10] including light source, reflector, light guide, diffuser, and brightness enhancement film (BEF). The light source can be an incandescent light bulb, light emitting diodes (LED), cold cathode fluorescent lamp (CCFL), hot cathode fluorescent lamp (HCFL). All the backlights employ a diffuser and a BEF. The diffuser posited between the light source and the display panel is used to scatter the light for display uniformity. The BEF is used to enhance display brightness. The cost structure of materials for TFT-LCDs is described in **Fig. 1-11** [1.57].

If we success to solve the reliability and uniformity problems, CNT-BLU will replace the traditional backlight system of LCD, it will be ensure to decrease amount of cost.

2.2 Experimental Procedures

2.2.1 Forward Arrangement

We have chosen 4 inch n-type silicon (100) wafer as our experimental substrate. After RCA clean and lithography processes, we defined several kinds of circle patterns for CNT flied emission arrays which diameter is 50μm in experiments (A) (B) (C) and 6μm in experiment (D). We designed three different pillar-spacing, which are 80μm, 150μm and 250μm respectively in experiments (A) (B) (C).

In the field emission measurement, n-type silicon (100) wafer was used as its cathode pad to save consumption from Cr electrode. Catalyst with 40Å cobalt-titanium and 10Å titanium co-deposited on 100Å aluminum. are sequentially deposited on Si substrates by magnetron sputtering (Ion Tech Microvac 450CB) at the pressure of 7.6×10^{-2} torr at room temperature. This sputtering system consisted of three sputtering source for different material targets and two power source for co-deposition, so our multilayer catalysts could be sequentially deposited without breaking the vacuum environment and co-deposited uniformly.

2.2.2 CNTs Synthesis

In our researches, an atmospheric pressure thermal chemical vapor deposition (T-CVD) system consists of a 2-inch-diameter horizontal quartz tube, an electric heating system, reaction gas supply, and related mass flow controllers shown in **Fig.2.4** is used for CNTs' synthesis. In order to prevent the nanoparticles are wrapped up by carbon graphite quickly. We reduce carbon source (C_2H_4) from 135sccm to 60sccm. Therefore, nanoparticles obtain suitable carbon source flowing and vertically aligned CNTs with long length and high density are obtained.

First, Samples loaded into the quartz tube are heated to the predetermined temperatures (700℃) in nitrogen at 1000 sccm to avoid catalyst being reacted during steps of heating. Secondary, hydrogen at 50 sccm is fed into quartz tube about 5 minutes to reduce the catalyst metal to the metallic phase, and then transforming into

nano-particles. Third, CNTs are grown at 700℃ with the flow rate of hydrogen is 10 sccm, 1000 sccm for nitrogen and 60 sccm for ethylene [2.11]. Finally, samples are furnace-cooled to room temperature in nitrogen at 3000 sccm. The schematic of growth process is shown below in **Fig 2-5**.

2.2.3 Analysis

The morphologies of CNTs' samples are characterized by scanning electron microscopy (SEM), the morphologies of pre-treatment catalyst are observed by atomic force microscopy (AFM). The finer internal structures of interface of CNTs and nano-sized catalytic materials were examined by high-resolution transmission electron microscopy (HRTEM), JEOL JEM-2000EX and X-ray energy dispersive spectroscopy (EDS) respectively.

Field emission characteristics of CNTs are measured with a parallel diode-type configuration in a high-vacuum chamber with the pressure of 5×10^{-6} torr. A glass substrate coated with indium tin oxide (ITO) and P22 phosphor (ZnS: Cu, Al) was used as the anode plate, and the distance between the cathode and the anode plate was set to be 150 μm. The emitting area was variable, which was determined by pillar-spacing and pattern-area.

Anode voltages is sweep-type from 0 V to 1000 V which are applied at intervals of 10 V by a source measure unit (Keithley 237) shown in **Fig. 2-6** for the verification of field emission characteristics while the cathode was biased at 0 V.

2.3 Experiment Procedures

2.3.1 Experiment A: Optimum R/H Ratio of Different Inter-Pillar Spacing

We investigated field emission properties from a pillar arrays of aligned carbon nanotube (CNT) bundles, which are fabricated on a Si substrate by thermal chemical

vapor deposition (T-CVD). To explore the influence of the pillar arrays' arrangement on its field emission, the ratio of inter-pillar distance (R) to pillar height (H), R/H shown in **Fig.2-7**[2.12], was investigated by changing H while maintaining R at 80 μm, 150 μm and 250 μm, respectively.

A circle arrays with 50 μm in diameter with three different inter-distances (80μm, 150μm and 250μm, respectively) using Co-Ti (40 Å)/Ti(10 Å) /Al (100 Å) as multilayer catalyst shown in **Fig.2.8** are made on a Si substrate (1cm×1cm) by photolithography and magnetron sputtering. To form catalyst nanoparticles, the catalyst was pre-treated at 700 ℃ for 5 min in hydrogen at 50sccm. Subsequently, thermal CVD was carried out at a growth temperature of 700 ℃ maintained by flowing 60sccm ethylene (C_2H_4) gas diluted with nitrogen (N_2) gas as carrier gas. The total experimental process of profile was shown schematically in **Fig. 2-9**.

Scanning electron microscopy (SEM) and transmission electron microscopy (TEM) are used to characterize the synthesized pillar array of aligned CNT bundles. The field emission property is measured using a parallel diode type configuration at a pressure of $\sim 10^{-6}$ torr. The gap between the anode plate and the CNT emitter was set at 150μm or 300μm.

2.3.2 Experiment B: Two-Step Growing Method for CNTs' synthesis

In this section, circle patterns with 50μm in diameter using Co-Ti(40 Å)/Ti(10 Å) /Al (100 Å) multilayer catalyst and inter-pillar distance is 80μm shown in Fig.2.8-(a). is made on a Si substrate (1cm×1cm) by photolithography and magnetron sputtering. To form catalyst nanoparticles, the catalyst pattern was pre-treated at 700 ℃ for 5 min in hydrogen at 50sccm. Subsequently, thermal CVD was carried out at a growth temperature of 700 ℃ maintained by flowing 60sccm ethylene (C_2H_4) gas diluted with nitrogen (N_2) gas as carrier gas and maintain 20mins for first step growth. Than flowed 1000sccm nitrogen (N_2) to perch space, and pretreated again for holding on second step CNTs growth. The total experimental process of profile was shown schematically shown   in **Fig. 2-10**.

2.3.3 Experiment C: Plasma Post-treatment for CNTs' Pillar arrays

Aligned CNT pillar array samples are synthesized by thermal CVD (T-CVD) on the patterned silicon wafer. The patterns for circular of 50μm diameter are fabricated silicon substrate.

In this section, sample with pillar height about 30μm and inter-pillar distance about 80μm is post-treated by High Density Plasma Reactive Ion Etching System (HDP-RIE). The plasma treatment of as grown CNT pillar array was carried out in a plasma of a mixture of O_2 and Cl_2 gases generated by microwave power. The flow rates and treating time of O_2 and Cl_2 were shown in **Table 2-1**. The operating temperature, pressure, and process duration in the plasma treatment are room temperature , 10 mtorr, and 2、3、5、10 min, respectively. The structural and chemical modifications of CNTs arrays before and after the plasma treatment are examined by a Hitachi model S-4700I scanning electron microscope (SEM) and Jobin Yvon model HR800 micro-Raman spectrometer, EDS, and TEM respectively. The field emission characteristics of the sample before and after plasma treatment were measured in a high vacuum chamber with a parallel diode-type configuration at a base pressure of $\sim 10^{-6}$ torr.

2.3.4 Experiment D: Triode Structure for CNT Field Emission

Schematically illustrates the fabrication procedures of triode structure for CNT field emission. Heavily doped N-type silicon wafers are used as the substrate. A 5000 –Å -thick silicon dioxide is thermally grown on the silicon substrate at $1050^{o}C$. A 2000 –Å -thick Poly-Si layer is then deposited on the thermal oxide by pressure chemical vapor deposition (LPCVD) using a pure SiH_4 gas at $620^{o}C$. The Poly-Si layer was further doped by $POCl_3$ at $950^{o}C$ for 20 min. An array of 100×100 circle patterns with the diameter of 6μm and inter-circle distance of 9μm are defined by photolithography and etching by Die-electric Material RIE 200L shown in **Fig 2-12**[2.13]. Then, the Poly-silicon layer is etched laterally by Die-electric Material RIE 200L to create a gap between the Poly-silicon gate and the CNTs shown in **Fig 2-13**. A catalytic layer of 50 Å cobalt-titanium in thickness is deposited on the 100 Å aluminum layer on the sample by sputtering. For deposition of the catalytic layer, the base and operating pressure of the sputter chamber are kept below 2×10^{-6} and 7.6×10^{-3} torr, respectively. The input RF power is 60W and the deposition rate was 0.1 Å /S for 100 Å aluminum layer. Then, the

input RF power for cobalt-titanium co-sputtering was kept 70W and 100W, respectively for 40 $\overset{\circ}{A}$ catalyst layer. Utilizing the original photoresist as a mask and lift-off technique, the circle pattern is transferred to the silicon substrate. Finally, CNTs are grown selectively on the iron layer by thermal chemical vapor deposition (T-CVD) system shown in **Fig 2-12**. The growth morphology of CNTs was observed by scanning electron microscopy (SEM).

Field emission properties of triode structure are measured in a high-vacuum environment with a base pressure of 1.0×10^{-6} torr. A glass plate coated with indium-tin-oxide (ITO) and phosphor is used as an anode and located 150μm above the sample surface. During the measurement, the device is in a common emitter configuration with the emitter grounded. The gate is applied with a voltage swept from 0 V to 80 V to obtain the current-voltage characteristics of the CNT triodes. The anode is applied with the constant voltage 800 V and the cathode maintain grounded, configuration shown in **Fig 2-14.**[2.14]
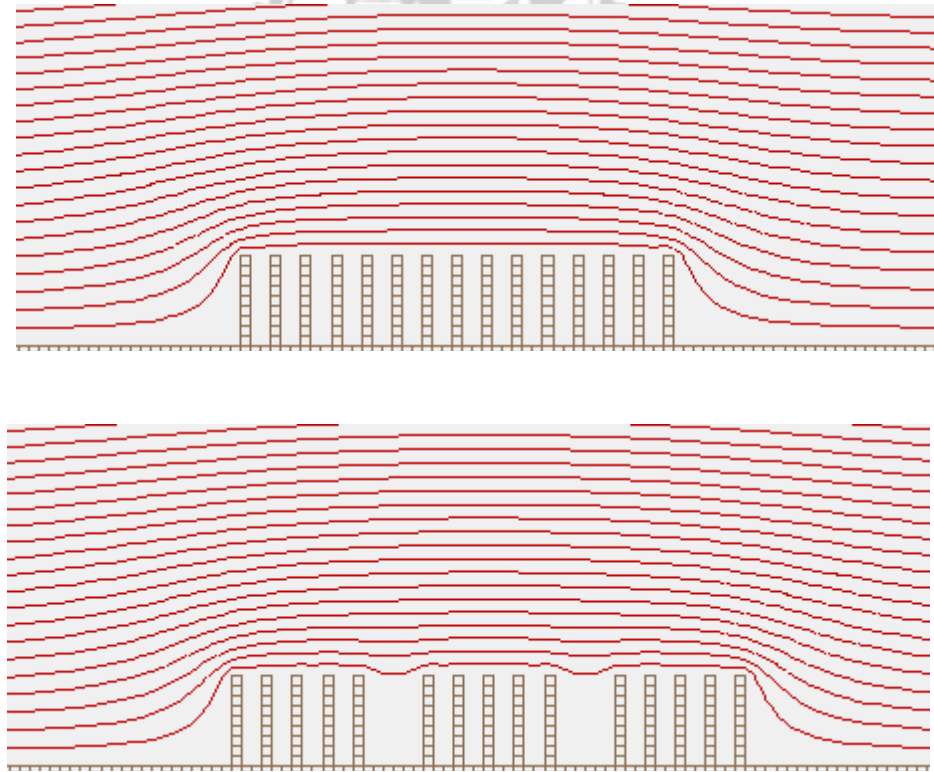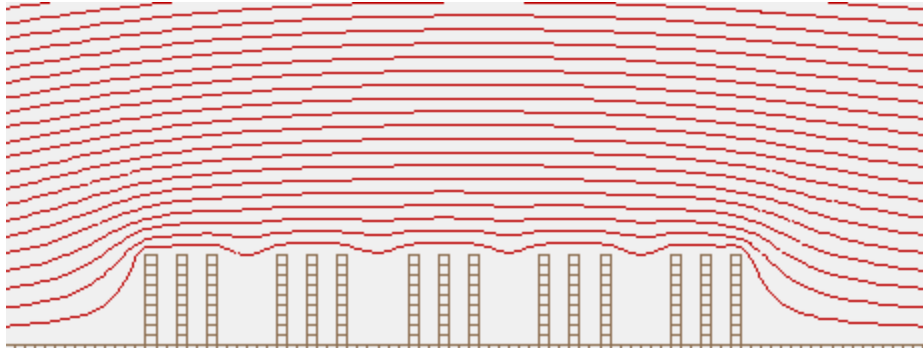
Fig.2.1 Simulation of the equipotential lines of the electrostatic field for tubes of different distances between tubes.

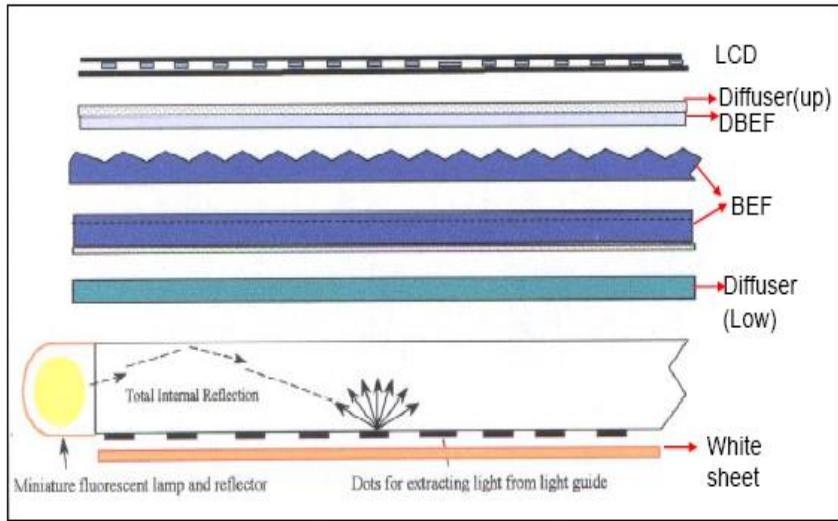**Fig.2.2 High Density Plasma Reactive Ion Etching System, HDP-RIE.**[2.9]

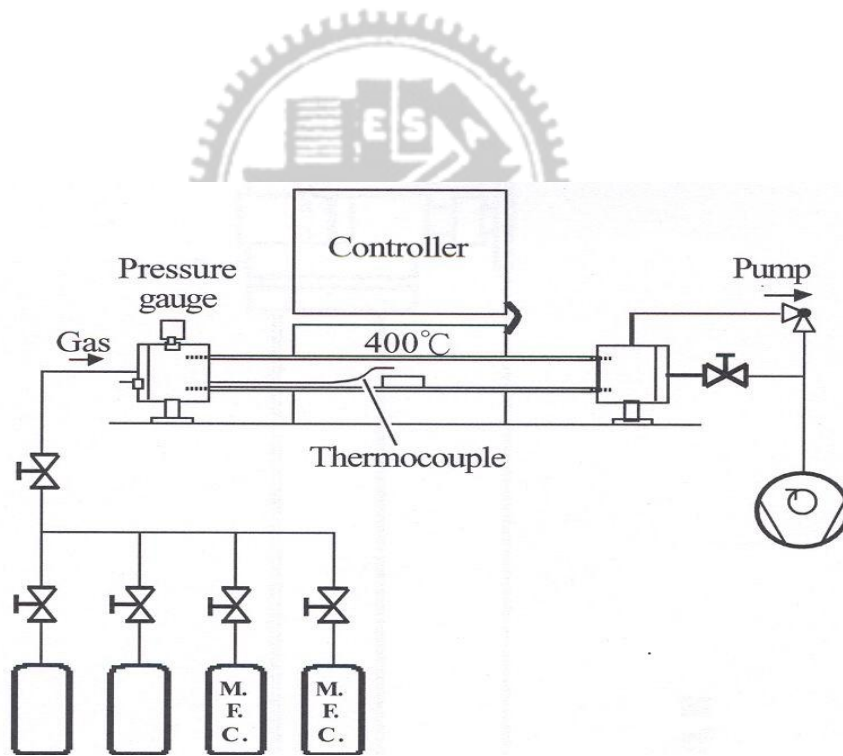**Fig.2.3 schematic of a typical backlight unit.**

Fig. 2-4 (a) Schematic picture and (b) photograph of thermal CVD.
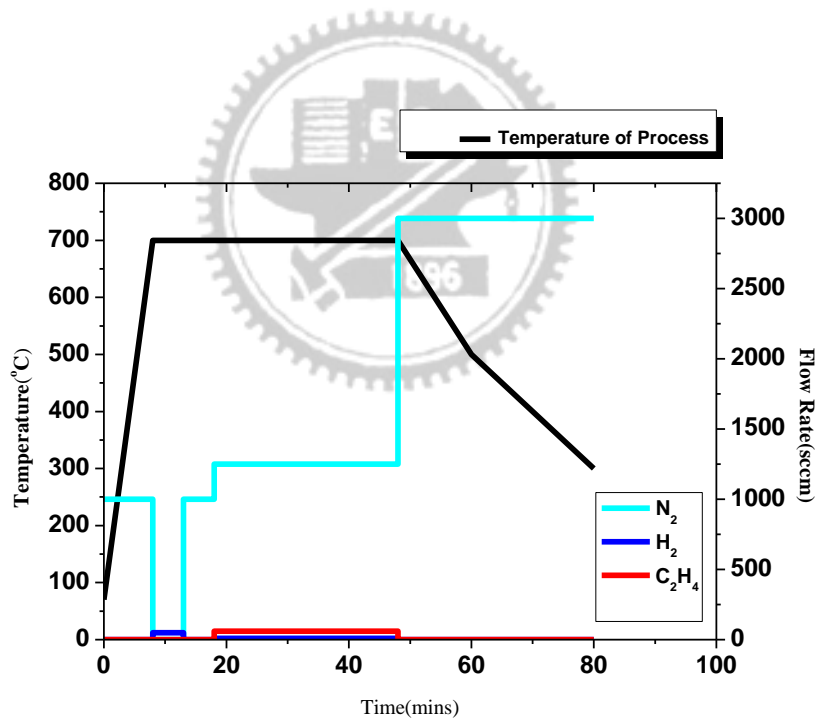

Fig. 2-5 Process of CNTs synthesis (an example of CNTs growing 30min at 700℃.
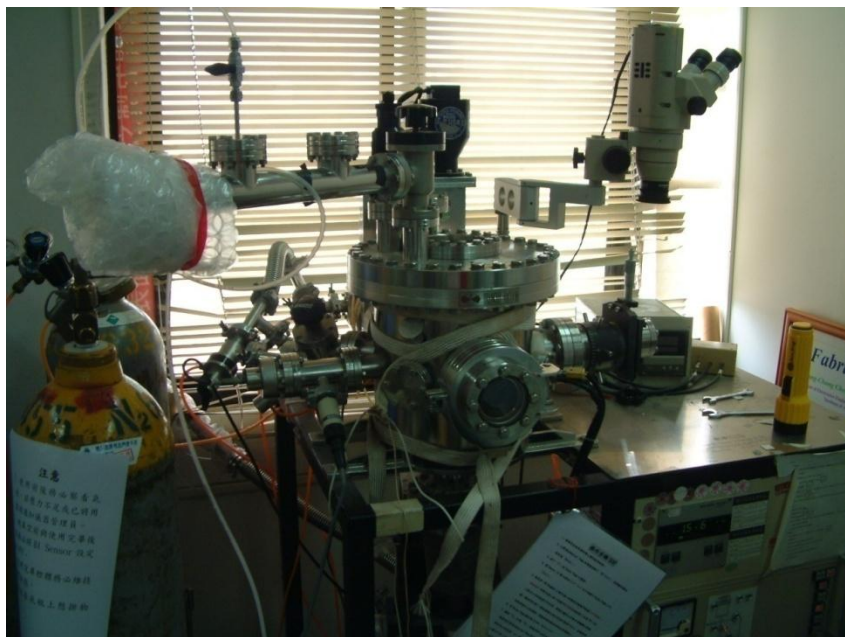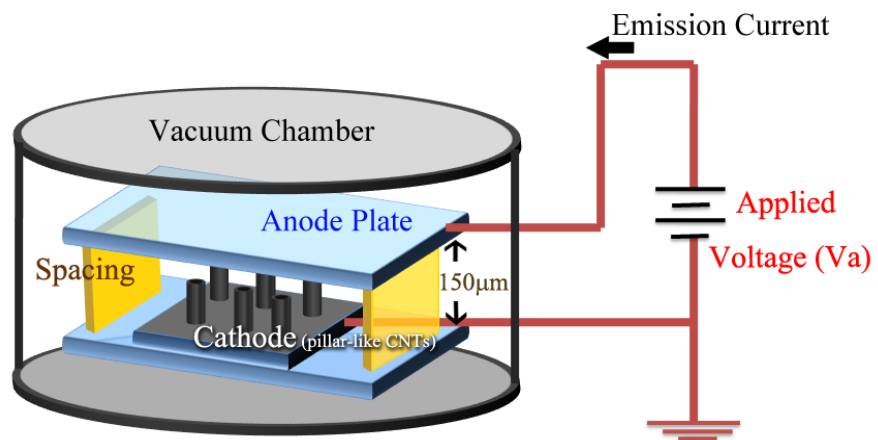
Fig. 2-6 High vacuum measurement system.

Fig.2-7 (a) SEM image of pillars of aligned CNT bundles grown by thermal CVD. (b) Cross-sectional SEM image of the pillar, showing that it is aligned perpendicular to the substrate surface and consists of high density CNTs[2.12]

(a)

(b)
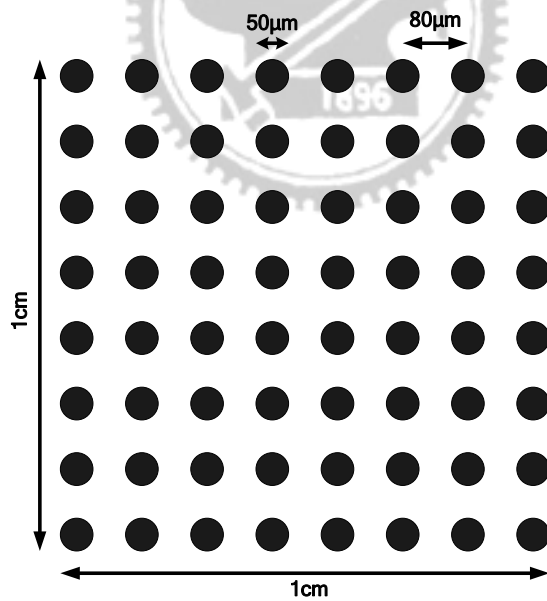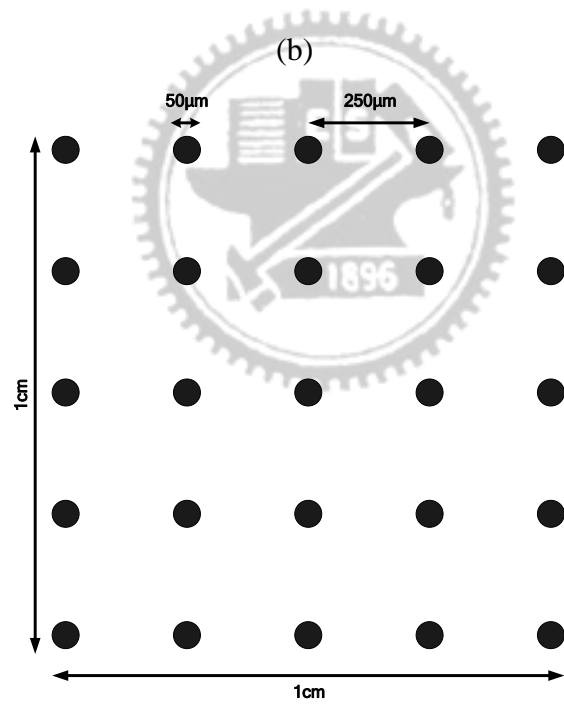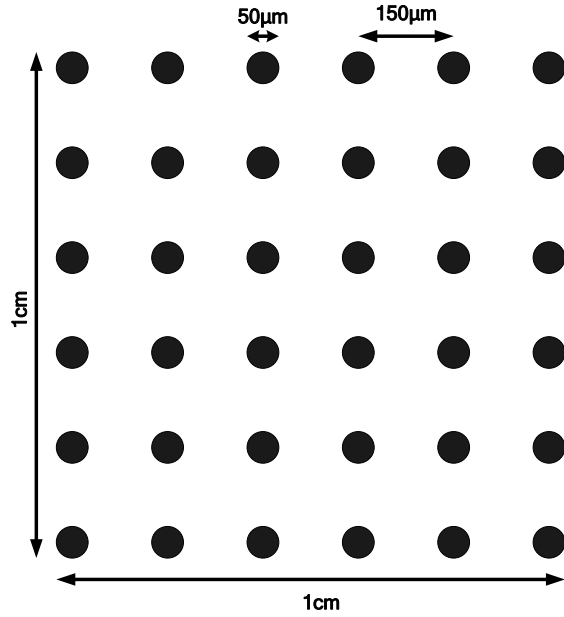
(c)

Fig.2.8 Masks design: (a)-(c) show array of three different inter-distance for 80 μm、150 μm and 250 μm defined in 1 cm×1 cm area, respectively.

Silicon substrate

(e) **PR development**

Photoresistance

(f) **Spatter catalyst**

Mask(pillar-like pattern)

(g) **Lift off**

Pretreatment
(h)
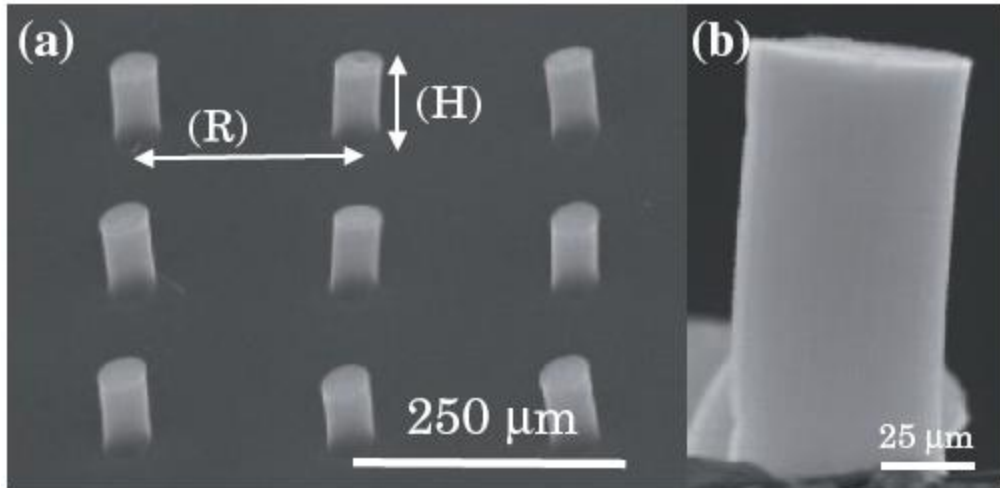
Exposure

(j) **CNTs growth**
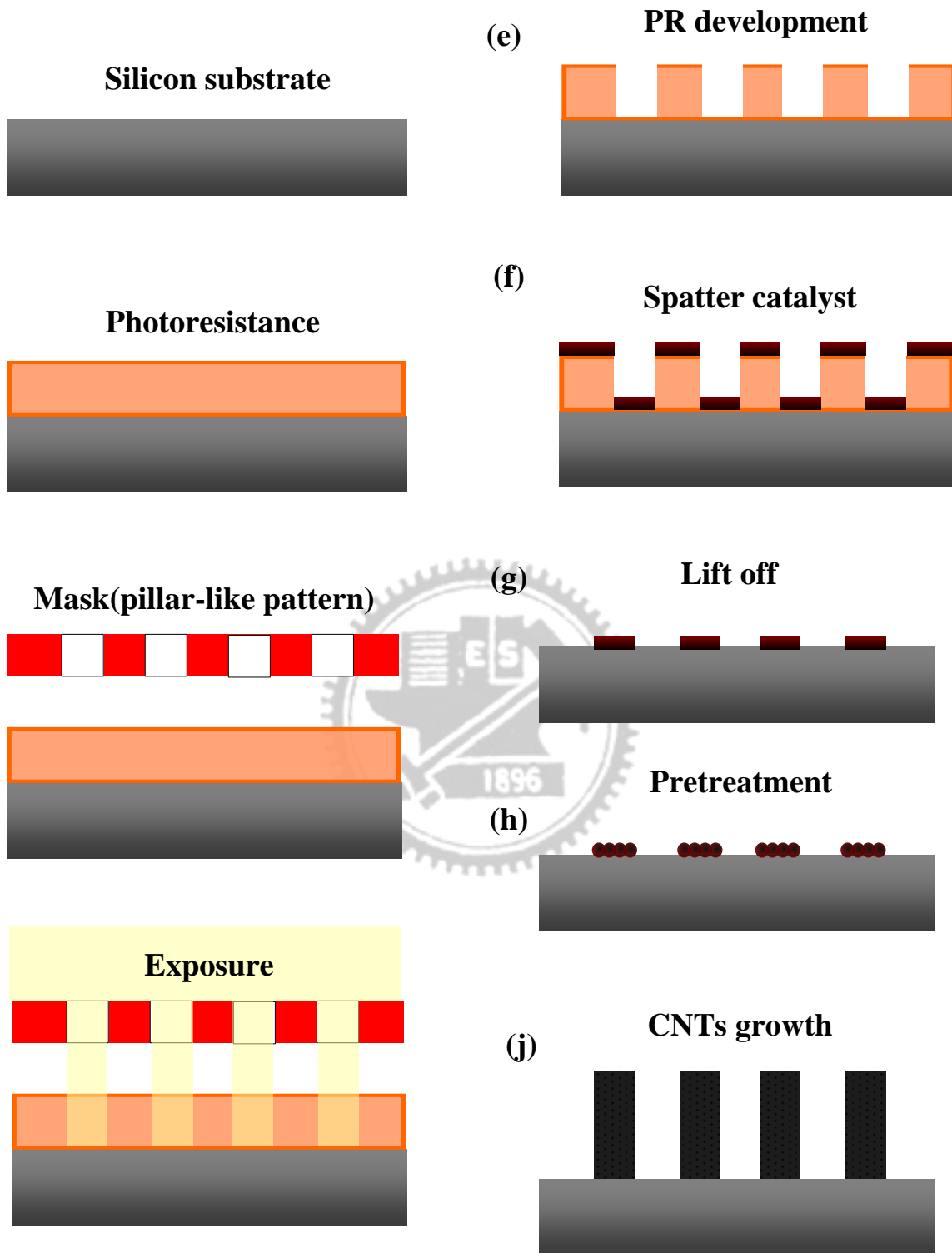
Fig.2.9 Fabrication flow diagrams (a) ~ (j). (f) Co-Ti / Al (2nm-3nm/10nm) catalyst by sputtering system, (h) pretreatment with H₂ (50 sccm), and (j) CNTs
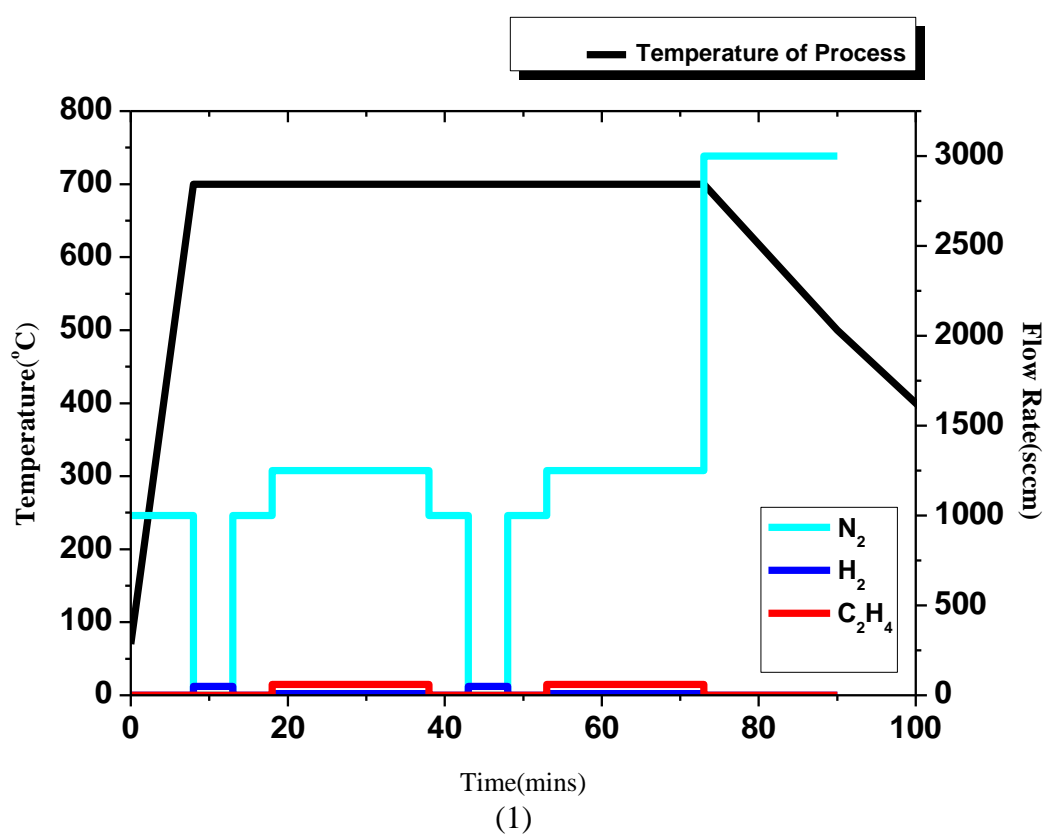
(1)
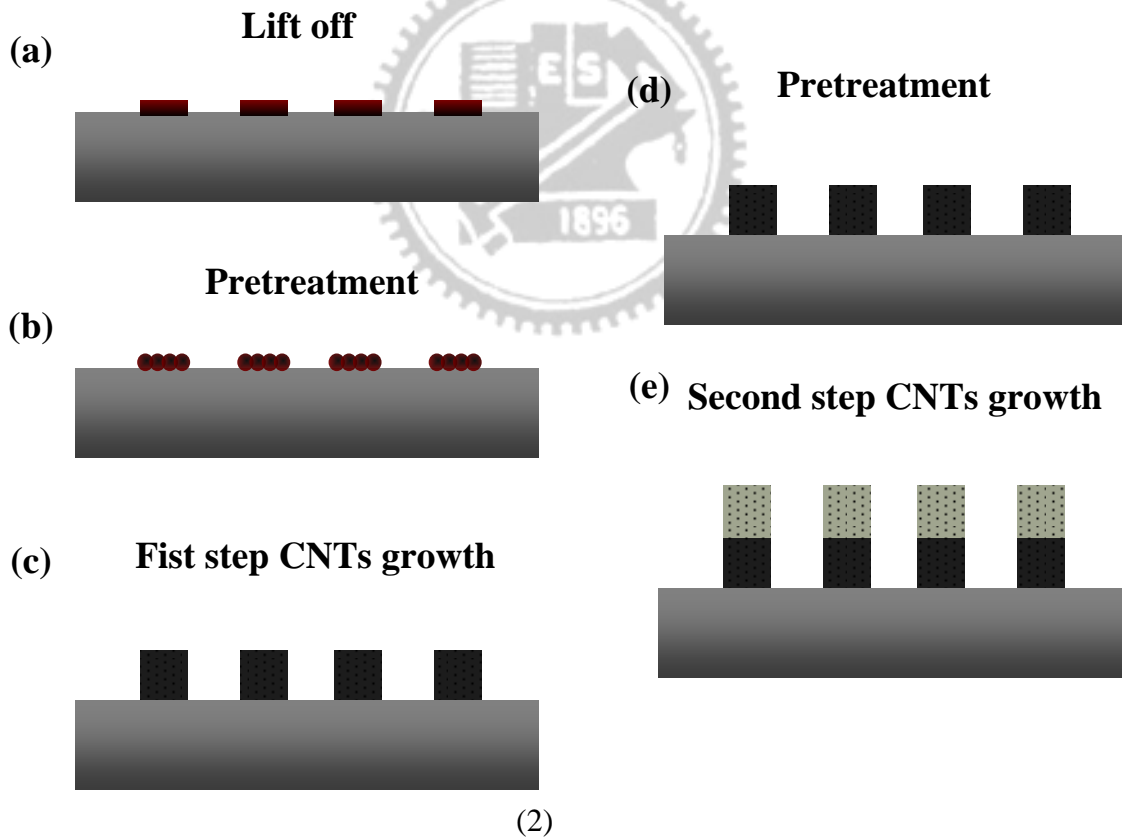
(2)

Fig.2-10 (1) Process of two steps growing for CNTs' synthesis.(2) Fabrication

flow diagrams (a) ~ (e). (d) pretreatment in H$_2$ at 50 sccm again , and (e)

second step CNTs growth method under C$_2$H$_4$ atmosphere.

(a)

Silicon substrate

(b) **PR development**

(c)

Spatter catalyst

(d)

Lift off by acetone

(e)

CNTs growth

(f)

CNTs treated after high density plasma
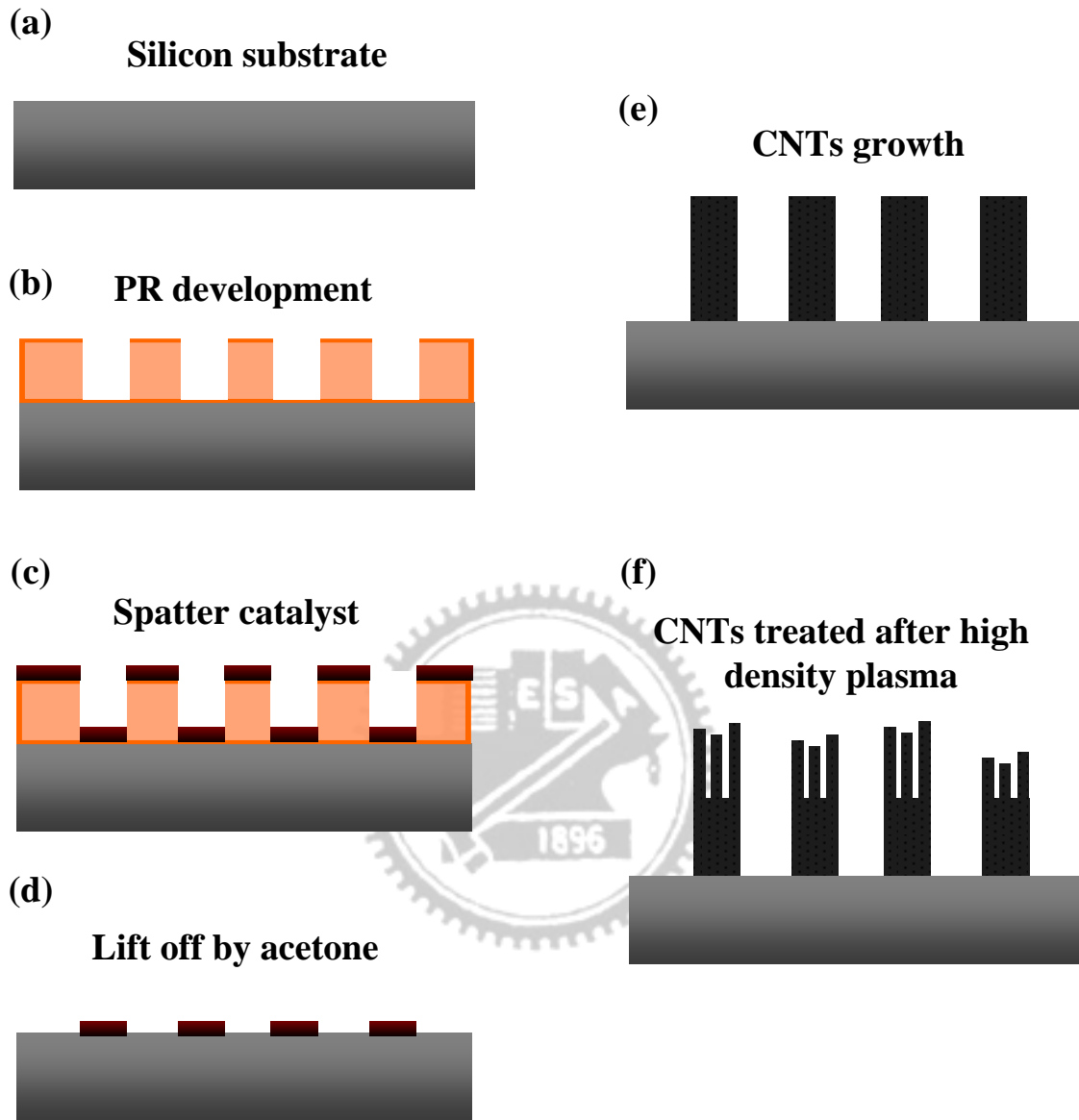
Fig.2.11 Fabrication procedures for CNTs treated by plasma etching.

Table 2-1 Sample1 and sample2 represent the post-treatment process in oxygen and chlorine plasma. (R.T=room temperature)

| | ICP power (W) | BIAS power (W) | Gas flow rate | | Time (min) | Substrate temperature (^{o}C) | Pressure (mtorr) |
			O_2 (sccm)	Cl_2 (sccm)			
Sample1	600	20	40	0	2	R.T	10
	600	20	40	0	10	R.T	10
Sample2	600	20	30	10	2	R.T	10
	600	20	30	10	3	R.T	10
	600	20	30	10	5	R.T	10
	600	20	30	10	10	R.T	10

(a) → N⁺ Poly-Si Gate
    → Thermal Oxide
    → Si(100)

(b) → Mask
    → Photoresist

(c) → Photoresist

(d)

(e) → Catalytic Metal Layer

(f)

(g) → Carbon Nanotubes
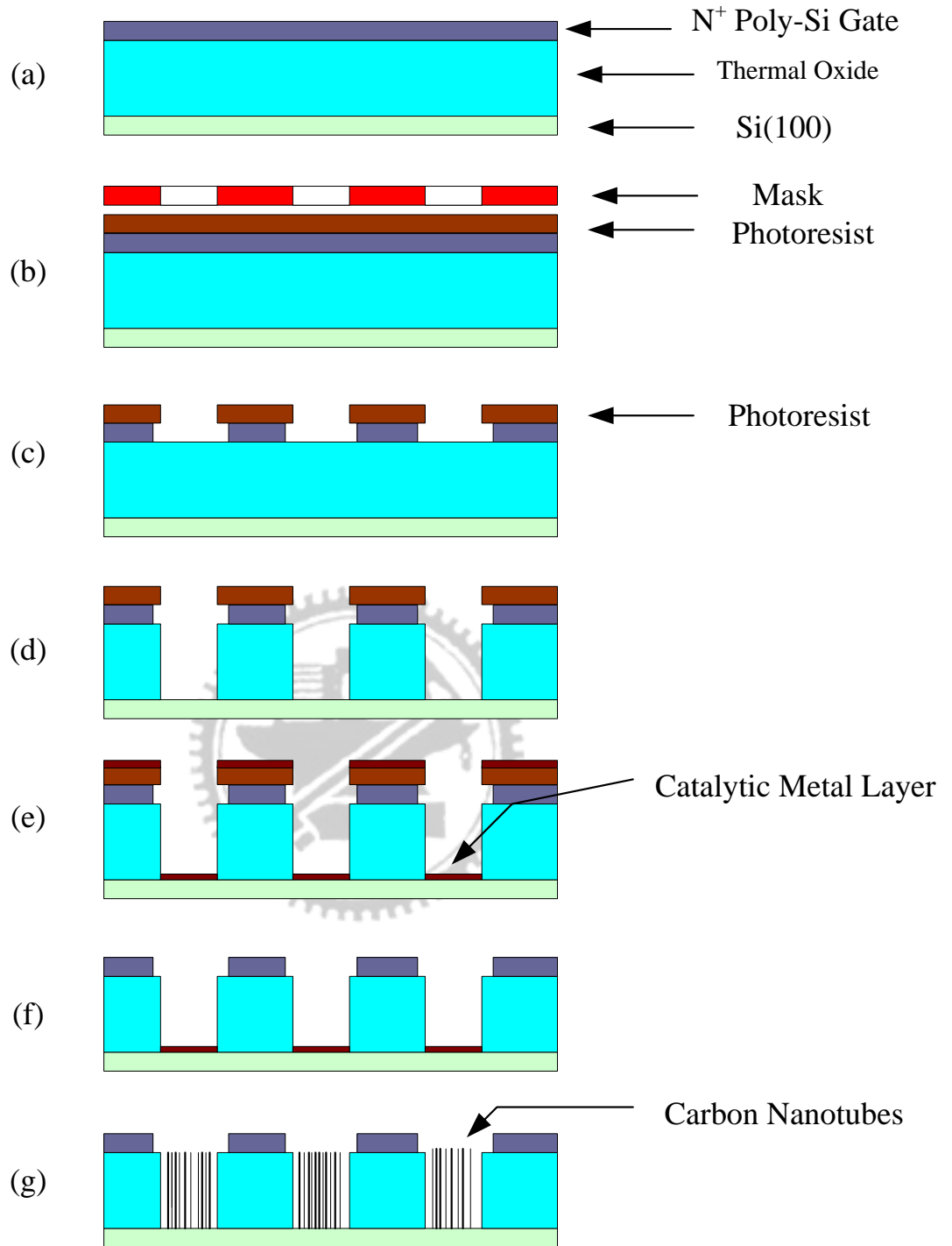
Fig 2-12 Schematic representation of fabrication procedures of triod structure.

45
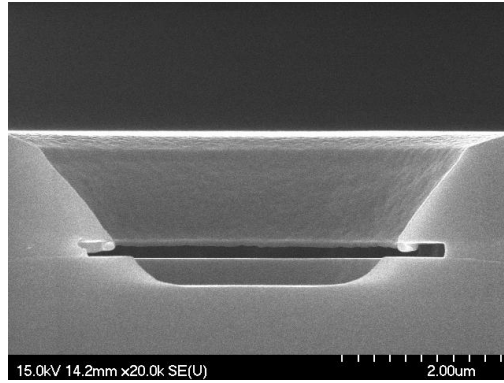
Fig 2-13The under etching condition of N-type Poly-silicon by Die-electric Material RIE 200L[2.13]

Anode

Gate

Cathode

$V_a > V_g$

$V_g > 0$

$V_C = 0$

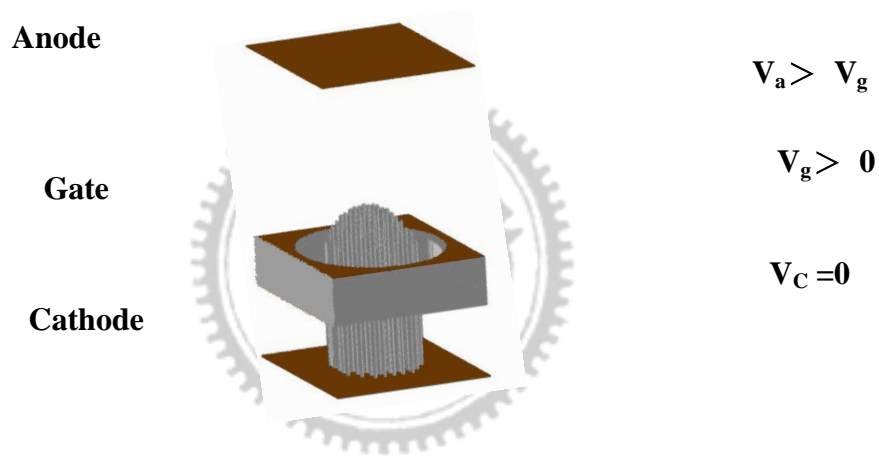**Fig 2-14 The aligned nanotubes in the bunch have variable heights and may protrude through the gate opening, as shown in the figure, or lie beneath the gate electrode plane.[2.14]**

Chapter 3:

Results and Discussion

3.1 Analysis of Catalyst

3.1 Analysis of Catalyst

  Prior to CNTs' growing, the choose of catalyst is very important. According to our group's researches, there are many advantages of CNT field emission characteristics by using novel co-deposition of catalyst. The most obvious characteristic is substantial increment of reliability.

  In the **Fig 3.1.7,** better uniform roughness and nanoparticle diameter are obtained in cobalt-titanium co-deposition case.[3.1] We have speculated that this phenomenon is caused by decreasing the diameter of nano-sized particles, therefore, finer particle provide higher activity and lower melting temperature. The AFM top view is the easiest method for making a comparison and it will clearly show the particle size and roughness, as shown in **Fig 3.1.7**.

  We compare catalysts of tri-components with catalysts of bi-components, with or without aluminum between electrode and other catalyst layers. Subsequently, we can easily find out the differences. The fluctuation in catalyst surface shows that simple and repeated nano-sized particle when pretreatment of bi-components catalyst without 100 Å Al buffer film, on the other hand, the fluctuation in catalyst surface is complex and additional curvature under those nano-sized particles when using the tri-components catalyst with 100 Å Al layer. As this result, we knew that Al plays a role of providing an additional curvature for surface of catalyst and quite increasing roughness mean square (RMS). The advantage of increasing RMS is raising the density of catalyst particle on the same top view area as shown in **Fig 3.1.2**, and then we can obtain better density of CNTs' pillar after the growing step.

  Furthermore, we focus the advantages of titanium (Ti) element in CNTs' growth. To

verify the effect of the Ti layer, because Co and Ti surface energy are very nearly [3.2], so that cobalt film turns into nanoparticles with uniform diameter during pre-treatment process. This phenomenon is shown in **Fig 3.1.3**. Adhesion is evidently improved is also found in our experiment. As for CNT films on Ti, in the high temperature due to the formation of conductive TiC , a barrier on the CNT–Ti junction is removed (as exhibited in **Fig 3.1.5**). Electrons can pass through this junction without obstacle. So, during the whole field emission, electrons need to overcome CNT-vacuum barrier only, as shown in **Fig 3.1.6**. Therefore, a very small voltage will result a considerable electron emission. So, titanium (Ti) layer can improve uniformity and strengthen adherence between CNTs and substrate for CNTs' growth [3.3]. The evident is shown in **Fig 3.1.4.**

3.2 Finding Optimum R/H Ratio of Different Pillar Spacing

3.2.1 Effect of carbon source flow rates on the morphology of CNTs' growth

It is indispensable to reduce the turn on field and threshold field to achieve practically applicable field electron emitters that operate at lower power consumption. It has been reported that field emission can effectively enhanced for aligned CNTs as field emitters when the ratio of distance between neighboring nanotubes to the height of each individual CNT is about 2 [3.4]. However, the optimum rule (R/H=2) for CNTs as electron field emitters has not been realized.

In our researches, different R/H ratios have been designed to study the relation between R/H ratios and the field emission characteristics, and it is essential to grow longer aligned CNTs' pillar with larger inter- pillar distance to meet the R/H ratios we need. However, growth of longer CNTs beyond 100μm is a little bit difficult. Therefore, it is very important to study the relation between the length of CNTs′ pillar and the growth condition including growth time, flow rate of carbon source, etc.

The length of the aligned CNTs pillar as a function of growth time is shown in **Fig 3.2.4(a)**. It is observed that there is a CNTs′ length limit of approximately to 130μm. In

this case of the aligned CNTs′ pillars grown on the aluminum substrate, the aligned CNTs can′t be lengthened even if prolongs the growth time beyond 90 min. When we increase the flow rate of C_2H_4 to 135sccm, its growth rate is about 2μ m/min faster than that at 60sccm at 700^oC in growth process. But the length of CNTs′ pillar does not match our prediction. **Fig 3.2.4 (b)** shows the longest CNTs′ pillar is about 50μ m , even if prolongs the growth time beyond 40min. It is probably due to too much amorphous carbon putting on catalytic nanoparticles. Too much carbon source to close crystalline graphite sheets of the wall and encapsulate nanoparticle at the closed tip is another probable reason. According to this result, we try to reduce the flow rate of C_2H_4 from 135sccm to 60sccm. Thus, moderate carbon source flow rate is indispensible to grow longer CNTs′ pillar. Besides, the tendency that CNTs′ growth rate is linear with the time until the length limit is reached is also observed from **Fig 3.2.4**. Therefore, moderate flow rate of carbon source as well as growth time is required to precisely control once we want to grow the specified length of CNTs′ pillar. According to our experimental results, we can easily grow longer length of CNTs′ pillar to meet the required R/H ratios we need.

3.2.2 Effect of arrangement of pillar array on its field-emission characteristic

Three circle patterns with different inter-pillar distance (80μ m,150μ m and 250μ m) are designed to get different R/H ratios. In the previous section, we have succeeded to find the suitable growth condition to grow longer length of CNTs′ pillar to meet the required R/H ratios we need.

The aligned CNTs pillar is characterized by high-resolution scanning electron microscopy (SEM). Aligned CNTs pillar that is perpendicular to the substrate surface is obtained due to J.van der Waals force between CNTs. **Fig.3.2.1 ~ Fig.3.2.3** show SEM images of an aligned CNTs pillar grown on silicon substrate with aluminum buffer layer.

(a) 80μm inter-pillar distance case

Fig.3.2.1 (a) shows the aligned CNTs bundle with a diameter of 50μ m and a height of 4.5μ m. The R/H value of 18.18 is obtained. **Fig.3.2.1 (b)** shows the aligned CNTs bundle with a diameter of 50μ m and a height of 8μ m. The R/H value of 11.2 is

obtained. **Fig.3.2.1 (c)** shows the aligned CNTs bundle with a diameter of 50μ m and a height of 10μ m. The R/H value of 8 is obtained. **Fig.3.2.1 (d)** shows the aligned CNTs bundle with a diameter of 50μ m and a height of 10.8μ m. The R/H value of 7.8 is obtained. **Fig.3.2.1 (e)** shows the aligned CNTs bundle with a diameter of 50μ m and a height of 13.2μ m. The R/H value of 6.06 is obtained. **Fig.3.2.2 (f)** shows the aligned CNTs bundle with a diameter of 50μ m and a height of 22.3μ m. The R/H value of 3.6 is obtained. **Fig.3.2.1 (g)** shows the aligned CNTs bundle with a diameter of 50μ m and a height of 53μ m. The R/H value of 1.5 is obtained.

(b) For 150μm inter-pillar distance case

Fig.3.2.2 (a) shows the aligned CNTs bundle with a diameter of 50μm and a height of 14μm. The R/H value of 10.7 is obtained. **Fig.3.2.2 (b)** shows the aligned CNTs bundle with a diameter of 50μm and a height of 20μm. The R/H value of 7.5 is obtained. **Fig.3.2.2 (c)** shows the aligned CNTs bundle with a diameter of 50μm and a height of 26μm. The R/H value of 6 is obtained. **Fig.3.2.2 (d)** shows the aligned CNTs bundle with a diameter of 32μm and a height of 14μm. The R/H value of 4.7 is obtained. **Fig.3.2.2 (e)** shows the aligned CNTs bundle with a diameter of 50μm and a height of 47μm. The R/H value of 3.2 is obtained. **Fig.3.2.2 (f)** shows the aligned CNTs bundle with a diameter of 50μm and a height of 60μm. The R/H value of 2.5 is obtained. **Fig.3.2.2 (g)** shows the aligned CNTs bundle with a diameter of 50μm and a height of 82μm. The R/H value of 1.87 is obtained.

(c) For 250μm inter-pillar distance case

Fig.3.2.3 (a) shows the aligned CNTs bundle with a diameter of 50μm and a height of 17.9μm. The R/H value of 14 is obtained. **Fig.3.2.3 (b)** shows the aligned CNTs bundle with a diameter of 50μm and a height of 23μm. The R/H value of 10 is obtained. **Fig.3.2.3 (c)** shows the aligned CNTs bundle with a diameter of 50μm and a height of 49μm. The R/H value of 5.1 is obtained. **Fig.3.2.3 (d)** shows the aligned CNTs bundle with a diameter of 50μm and a height of 80μm. The R/H value of 3.1 is obtained. **Fig.3.2.3 (e)** shows the aligned CNTs bundle with a diameter of 50μm and a height of 100μm. The R/H value of 2.5 is obtained.

From the SEM images in the above section, patterned CNT pillars with different

R/H ratios we need have been fabricated successfully using thermal chemical vapor deposition (CVD) method. Therefore, it is easily to study the effect of R/H ratios on the field emission characteristics of CNTs′ pillar arrays.

3.2.3 Effect of different CNTs′ pillar arrays with different R/H ratios on the field-emission characteristic

In our experiment, we get high density, vertical, long length and aligned CNTs pillar structure with different inter-pillar distance. Then, the relation between R/H ratios and field-emission characteristics from the CNT pillar array are studied. **Fig.3.2.5(a)** shows field emission current density (J) as a function of applied electric field (E) for CNT pillar arrays with heights of 4.5μm, 8μm, 10μm, 10.8μm, 13.2μm, 22.3μm and 53μm (R/H=18.18, 11.2, 8, 7.8, 6.06, 3.6,and 1.5,respectively). We find that the best field-emission characteristic is obtained from the pillar array with R/H=8 (H=10μm) and it will be discussed later. **Fig3.2.5(c)** shows the Fowler–Nordheim (FN) plots corresponding to Fig3.2.5(a) .The occurrence of field emission is confirmed by the linearity of the FN plot. **Fig 3.2.6(a)** shows the turn-on field ($E_{turn-on}$) obtained from **Fig. 3.2.5(a)** as a function of R/H. $E_{turn-on}$ is defined to be the field required to produce J=10 μA/cm^2. The optimal value of R/H giving a value of minimum $E_{turn-on}$ is approximately 8. which corresponds to H=10μm. When R/H is smaller than 8, the field-emission characteristic is poor, which is likely to be due to the field screening effect. However, when the R/H is greater than 8, $E_{turn-on}$ increases, and the reduction of field enhancement owing to a small H is conjectured. **Fig3.2.6(b)** shows R/H versus the field enhancement factor (β), [3.12] which is estimated from the slope of the FN plots in Fig. β is estimated experimentally by setting the work function of the CNTs to be 5 eV. The obtained values of β for the CNT pillar array with R/H values of 8, 11.2, 6.06 and 1.5 are 61060, 54540, 29075 and33031, respectively. The best field enhancement factor is obtained at R/H~8.

In the case for inter-pillar distance of 150μm, the relation between R/H ratios and field-emission characteristics from the CNT pillar array are studied. **Fig3.2.7** shows emission current density (J) as a function of applied electric field (E) for CNT pillar arrays with heights of 14μm, 20μm, 26μm, 32μm, 47μm, 60μm and 82μm (R/H=10.7,7.5,6, 4.7,3.2,2.5and1.87,respectively). We also find that the best

field-emission characteristic is obtained from the pillar array with R/H=4.7 (H=32μm), and it will be discussed later. **Fig.3.2.7(c)** shows the Fowler–Nordheim (FN) plots corresponding to **Fig3.2.7(a)**. The occurrence of field emission is confirmed by the linearity of the FN plot. **Fig.3.2.8(a)** shows the turn-on field obtained from **Fig.3.2.7(b)** as a function of R/H. The optimal value of R/H giving a value of minimum $E_{\text{turn-on}}$ is approximately 4.7, which corresponds to H=32μm. When R/H is smaller than 4.7, the field-emission characteristic is poor, which is likely to be due to the field screening effect. However, when the R/H is greater then 4.7, $E_{\text{turn-on}}$ increases, and the reduction of field enhancement owing to a small H is conjectured. **Fig.3.2.8(b)** shows R/H versus the field enhancement factor (β), [3.12] which is estimated from the slope of the FN plots in **Fig 3.2.7(c).** The obtained values of β for the CNT pillar array with R/H values of 6, 4.7and 1.87 are 52907, 97345 and 42901, respectively. The best field enhancement factor is obtained at R/H~4.7.

In the case for inter-distance of 250μm, the relation between R/H ratios and field-emission characteristics from the CNT pillar array are studied. **Fig.3.2.9(a)** shows emission current density (J) as a function of applied electric field (E) for CNT pillar arrays with heights of 18μm, 23μm, 49μm, 80μm and 100μm (R/H=14,10,5.1, 3.1,3.2,2.5and1.87,respectively). We also find that the best field-emission characteristic is obtained from the pillar array with R/H=3.1 (H=80μm), as discussed later. **Fig.3.2.9(c)** shows the Fowler–Nordheim (FN) plots corresponding to **Fig.3.2.9(a)** The occurrence of field emission is confirmed by the linearity of the FN plot. **Fig.3.2.10(a)** shows the $E_{\text{turn-on}}$ obtains from **Fig.3.2.9(b)** as a function of R/H. The optimal value of R/H giving a value of minimum $E_{\text{turn-on}}$ is approximately 3.1, which corresponds to H=80μm. When R/H is smaller then 3.1, the field-emission characteristic is poor, which is likely to be due to the field screening effect. However, when the R/H is greater than 3.1, $E_{\text{turn-on}}$ increases, and the reduction of field enhancement owing to a small H is conjectured. **Fig.3.2.10(b)** shows R/H versus the field enhancement factor (β), [3.12] which is estimated from the slope of the FN plots in **Fig.3.2.9(c)**. The obtained values of β for the CNT pillar array with R/H values of 10, 3.1and 2.5 were 58223, 89427 and 44792, respectively. The best field enhancement factor is obtained at R/H~3.1.

Based on these results and measurements, we find not all of CNT pillar arrays having optimal R/H value of 2.[3.4] The inter-pillar distance is an important key about what optimal R/H value we can achieve. Once the inter-pillar distance is close, the edges of the pillars significantly interfere with field enhancement.[3.5] Most of field emission electrons are contributed from the edges of each pillar. One the contrary, large inter-pillar distance leads less field screening effect and each pillar can be regarded as a single emitter. **Fig.3.2.11** shows that the optimal R/H values decrease from 8 to 3.1 when the inter-pillar distances increase from 80μm to 250μm. [3.10] Therefore, the optimal R/H value approaches the theoretical calculated value (i.e. 2) at larger R.

Luminescent uniformity is another important topic for backlight application. In order to improve uniformity in a unit, less field screening effect for the edges of pillar to pillar is needed. [3.6] **Table3-2** shows the relation between luminescent uniformity and R/H value of different inter-pillar distances at the applied field of 2.5 V/μm. It is evident that luminescent uniformity has strong relation to the R/H value. The luminescent image has better uniformity when the R/H value is optimal for three different inter-pillar distances. The best luminescent uniformity is achieved with R/H value of 3.1 when R is 250μm. Therefore, we have demonstrated that CNTs′ pillar arrays has deep potential in the backlight application.

3.3 Analysis of Two-Step Growing Method

3.3.1 Effect of evolution recipe on the morphology of CNTs' growth

Growth of longer CNTs seems not to be an easy job and needs to find a precise control of some parameters such as the choice of catalyst, the growth condition and growth methods, and so on. In our experiment, we have tried a lot of methods using thermal chemical vapor deposition (T-CVD) to grow higher and perpendicular pillar arrays to meet the required R/H value we have designed. A funny and special method (two-step growth) is found after numerous trials of changing growth parameters for CNTs′ growth and is proved to be an efficient way to improve field emission characteristics. In this two step growth method, the first growth step which is the same as the previous

mentioned method and the growth time is 20 min. Then, we try to control nanoparticles at the tip of CNTs not to be encapsulated completely by amorphous carbon. The cooling step is replaced by another pre-treatment process. Then, the second growth step is proceeded to flow carbon source (C_2H_4) at 60sccm, hydrogen at 10sccm, and nitrogen at 1000sccm into the furnace to grow CNTs for 20 min, respectively. It can keep growing until running out of activity of catalysts. Then cooling step is the same as first growing step.

Two-step growth method is an efficient way to grow longer CNTs. We have successfully used this method to obtain aligned, vertical and longer CNTs pillar arrays and some useful material analyses used to study their properties of CNTs will described in the next section.

3.3.2 SEM TEM and Raman spectrum analysis

SEM, TEM and Raman spectrum are used to study the morphology and material properties. **Fig 3.3.1(a)** shows CNTs′ pillar arrays with the height of about 80μ m grown by one-step growth method. **Fig 3.3.1(b)-(c)** show that the diameter of CNTs grown by one-step growth method ranges from 32μ m to 42μ m. **Fig 3.3.2(a)** shows aligned, perpendicular CNTs′ pillar arrays with the height of about 80μ m grown by two-step growth method. This confirms longer CNTs growing ability for this two step growth method. **Fig 3.3.2(b)** shows top view image of one pillar. **Fig 3.3.2(c)** shows the tilt image on the top of pillar. **Fig 3.3.2(d)** shows CNTs′ pillar with one joint between the upper part and the bottom part of CNT′ pillar.

Fig 3.3.3 shows the SEM images of CNTs grown by two-step growth method. The diameter of the upper part of the pillar ranges from 20 to 26μm and the diameter of the bottom part of the pillar is about 32nm. The size of catalyst nanoparticles of the two step growth method is speculated smaller than that of one step growth method. Thinner diameter of CNT in the upper part than that of the bottom part means that CNTs′ pillars grown by this two-step growth method have higher aspect ratio.

The Raman spectra of one step growth and two-step method are plotted in **Fig**

3.3.4. The two main features in the Raman spectra are the D and G peaks about 1350 and 1600 cm^{-1}, respectively. The G band corresponds to the symmetric E_{2g} vibrational mode in graphite-like materials, while the D band is activated in the first-order scattering process of sp^2 carbons by the presence of substitutional hetero-atoms, vacancies, grain boundary or other defects and by finite size effects, all of which lower the crystalline symmetry of the quasi-infinite lattice. Sharper D and G peaks are shown in two-step growth case of CNTs and the I_G/I_D increases from 1.5 to 1.8 which confirms that the CNTs have a highly crystalline graphite structure. The TEM images show its magnified CNTs as shown in **Fig 3.3.7.** It is obvious that few defects in the graphite wall.

Therefore, less field screening effect and enhancement in field emission characteristics can be achieved due to thinner diameter (i.e. high aspect ratio) and highly crystalline graphite structure.

3.2.3 Comparing usual recipe and this special recipe in electric characteristic

Fig 3.3.5-(a) shows the current density versus electric field characteristic (J-E plot) of the pillar arrays. The Fowler- Nordheim (FN) plots are shown in **Fig 3.3.5-(c)** and their linearity verifies the field emission phenomenon. The turn-on field($E_{turn-on}$) and threshold field (E_{th}) are defined to be the field required to produce the current densities of 10 μA/cm^2 and 10 mA/cm^2 are 0.1 V/μm and 0.64 V/μm, respectively. The obtained E_{th} is the lowest value that has been reported to date. The electron field emission is monitored by a fluorescent screen at an electric field of 0.66 V/mm, as shown in **Fig 3.3.6**. The emission uniformity and high brightness are clearly evident.

3.4 Field Emission and Uniformity Improvement by Plasma post-treatment

3.4.1 Effect of plasma post-treatment on CNTs' pillar morphology

Fig 3.4.1. shows the typical top view SEM images and cross-sectional views of CNT films before and after pure O_2 plasma treatment. The O_2 gas flow rate was 40sccm and the 20W BIAS Power with different etching time: (a) 2 min, (b) 10 min. The density of the CNTs decreases as plasma treats, which results from the destruction of CNTs during oxygen plasma treatment. We got the result that no matter what post-treatment with 40sccm O_2 plasma for etching time 2 or 10 min, their morphology was become short, dispersed and surface was covered with amorphous carbon and oxygen carbonization. Thus, we tried to decrease oxygen flow to 30sccm and introduced 10sccm chlorine, respectively. The Cl_2 mix O_2 plasma with 20W BIAS Power with different etching time: (a) 2 min, (b) 3min, (c) 5min and (d) 10min, were shown in **Table 2-1**. **Fig 3.4.3** shows the SEM mocrographs of the as grown CNT pillar array was not obviously different with untreated case in macro view. But, in the micro view at the tip of the pillar, the CNTs merged together to decrease field screening effect, and increase field emission sites. **Fig 3.4.4** shows the SEM images for 3min case. The result not only maintained the benefits of the **Fig 3.4.3** (2 min), but also formed the ring edges around the periphery at the tip of a pillar. [3.8] This structure can provide more many field emission sites in edge areas. [3.9] **Fig 3.3.5** shows the SEM mocrographs of the as grown CNT pillar array as well as the conical shaped CNT pillars after the plasma treat for 5 min.

3.4.2 TEM, Raman spectrum and EDS analysis

We had analyzed CNT pillar array after O_2 mix Cl_2 plasma post-treatment by Raman spectrum, EDS and TEM analysis. The Raman spectra of the CNT pillar array before and after plasma post-treatment in the frequency range of 500–2500 cm^{-1} are shown in **Fig 3.4.7 .** The spectra show mainly two Raman bands at 1350 cm^{-1} (*D* band) and 1580 cm^{-1} (*G* band). In the spectra of CNT pillar array, the *D* band of the sample after 5 min plasma treatment appears as a small shoulder of the *G* band at 1610 cm^{-1}. The origin of the *D* and post-treatment of *D* bands have been attributed as the disorder features of graphitic sheets [3.7]. The *D* bands become stronger and sharper after plasma treatment. The details of the Raman analysis is summarized in Table.. The intensity ratio of the *G* band to the *D* band (I_G/I_D) from 1.47 to 0.82 after plasma treatment.The ratio values given in **Table 3-3** are the I_G/I_D ratio of the corresponding peaks. We found that I_G/I_D ratio decayed linearly as increasing the time for plasma post-treatment as shown in **Fig 3.4.8**.

The EDS spectra analysis show in Table3-4. **Fig.3.4.9 (a)-(d)** show the EDS spectra of the tips after 2, 3, 5 and 10 min for plasma treatment, respectively. The nanoparticles observed at the tip of the aligned CNTs consisted of Co, O, Cl principally..In spite of Ti co-deposited in the catalyst, there are none of Ti atoms at the CNTs' tips in **Table3-4**. It indicated that titanium (Ti) doesn't catalyze action. However, the coble atom(%) was decayed from 0.23% to 0.14%. It means O_2 mix Cl_2 plasma is effective to remove nanoparticles from the tips of the aligned CNTs. Thus, after this post-treatment we got more many emission sites at the CNTs' tips.

The TEM images show its magnified CNT as shown in **Fig 3.4.12**. It is obvious that cut tip without nanoparticale as post-treatment. Therefore, it contributed more emission sites for field emission. Thus, we can got more uniformity field emission result by this way.

3.4.3 Improvement of Uniformity and FE characteristic

Fig 3.4.10 show the results of the field emission measurement made on the as grown CNT pillar array after plasma treatment. The turn-on fields ($E_{turn-on}$ defined at an emission current density of 10 $\mu A/cm^2$) for the sample before and after 2, 10 min O_2 plasma treatment are 3.45, 3.82 and 3.94 V/μm, respectively shown in **Fig 3.4.10(a)**. According for pure 40sccm O_2 plasma consuming carbon graphite was too fast to remain some amorphous carbon and some carbon oxide. Those materials reduced field emission current and raise the turn-on filed on the contrary. In O_2 mix Cl_2 plasma post-treatment, we replaced 10sccm O_2 to 10sccm Cl_2 flow. Utilizing O_2 reacted with carbon to produce $CO_{2(g)}$ and $CO_{(g)}$,and exposed the coble nanoparticles at the tip of aligned CNTs. Then, chlorine reacted with coble nanoparticles to etch and remove it way. This continue chemical reaction produced many emission sites for this application. for the sample after 2,3,5 and 10 min O_2 mix Cl_2 plasma post-treatment are 2.95, 1.32, 2.08 and 5.4 V/μm, respectively in **Fig 3.4.10 (b)**. The optimal post-treatment time is 3min, it was removed amount of nanoparticles at the aligned CNTs' tips and made more effective emission sites in the meantime. Keeping on treatment time for 5 min, many defects were formed to course the current density to electric field curve unstable in high electric field. Keeping on treatment time for 10 min, too much amorphous carbon and chloride were formed that was the main reason for poor electric characteristics. **Fig 3.4.11** shown the image of fluorescent screen monitoring the field emission from the pillar array (10mm×10mm) at an electric field of 3.33V/μm.(a) no post-treatment, (b) post-treatment for 3min. Obviously, after O_2 mix Cl_2 plasma post-treatment image of fluorescent screen monitoring the field emission were more bright and more uniformity.

3.5 Field emission Characteristics of CNT Field Emission Triode

3.5.1 Simulations of CNTs' triode structure

Simulations were performed to investigate the beam spreading of emission electrons with commercial software (SIMION-3D) using the finite element method. It was found that an initial energy and divergence angles of e-beams at the moment of emission from CNTs were 5 eV and -90°~+90°, respectively [3.11].

Our triode structure was design as **Fig3.5.1**. Central CNTs were used to be cathode electric emitter, and surrounding N-type poly-Si was used to be gate of this triode structure. Basically the anode voltage was fixed as 800V, cathode was 0V, and the gate was sweeping from 0V to 80V. Secondly, the spacing between cathode and anode was fixed as 150μm, the phosphor was deposited on anode glass plate with ITO coating.

Instead of the diode structures of field emission were shown in **Fig 3.5.2 (a)** without gate voltage bias and the triode structures of our field emission unit shown in **Fig3.5.2 (b)**. We could obviously observe the enhancement of concentration by triode gated structure and gate structure can enhance the density of equipotential lines near CNT tips shown in **Fig 3.5.3**, but it has the leakage current from cathode to gate shown in **Fig 3.5.2(b)** .Furthermore, the gap between the gate and CNTs can be controlled by varying the poly-Si lateral etching time. In **Fig 3.5.5 (c)、(d)** show a SEM micrograph of CNT pillar triode for poly-Si lateral etching time of 80 s. The growth time of the CNTs was 5min. It can be seen that CNTs area well oriented and perpendicularly distributed in the center of the gate hole.

3.5.2 Effect of pillar length on the field emission characteristics

The effect of the length of CNT pillar was investigated with the gate-to-emitter gap kept at 1μ m. The length of CNTs can be adjusted by changing the growth time. **Fig3.5.4** and **Fig3.5.5** show SEM micrographs of planner-type CNT triodes for the growth times of 1 min,

2 min and 5 min, respectively. The lengths of the CNTs are 0.5μ m, 1μ m and 5μ m for the growth times of 1 min, 2 min and 5 min, respectively. The top of nanotube tips for the growth times for 2 min and 5 min are higher than the gate top surface and that for the growth time of 1 min is lower than the gate. Uniform growth of CNTs was achieved over the entire array for all CNT triodes.

The J_A versus V_B characteristics of CNT triodes for different lengths of CNTs are shown in **Fig3.5.6**. The turn-on voltages were 17 V and at beginning, respectively. A higher gate voltage is required when the nanotubes are lower than the gate. This is ascribed to that more emitted electrons would be captured by the gate. However, when the CNTs are much higher than the gate, the tips of the nanotubes also need high gate voltage to emit electrons due to the increasing distance between the gate and emitters. Thus, the proper length of CNTs should be considered to achieve the low turn-on voltage field emission triodes. The corresponding F-N plots of the CNT triodes for 1μm of nanotubes was shown in **Fig 3.5.7.** In the **Fig 3.5.8** Images of fluorescent screen monitoring the field electron emission from the CNT triode array (3mm × 3mm) at the gate voltage (a) 20 V, (b) 30 V , respectively.

Fe-Ti
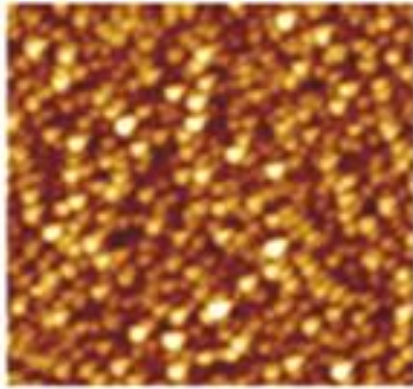
Co-Ti
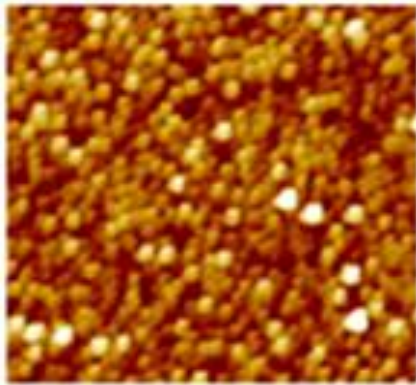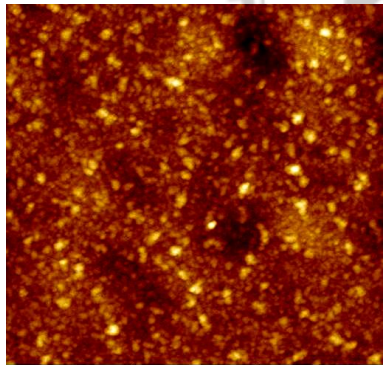
Co-Ti/Al
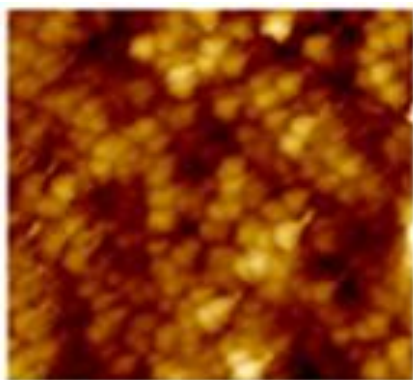
[Fig 3.1.7] AFM images of different catalysts growing at 700°C. The white pixel is standing for highest pick and the dark pixel is standing for the valley.

Co/Ti/Al

```
Digital Instruments NanoScope
Scan size          3.000 µm
Scan rate          1.001 Hz
Number of samples    512
Image Data         Height
Data scale         100.0 nm
```

view angle
light angle

X 1.000 µm/div
Z 100.000 nm/div

0 °

wei600.002
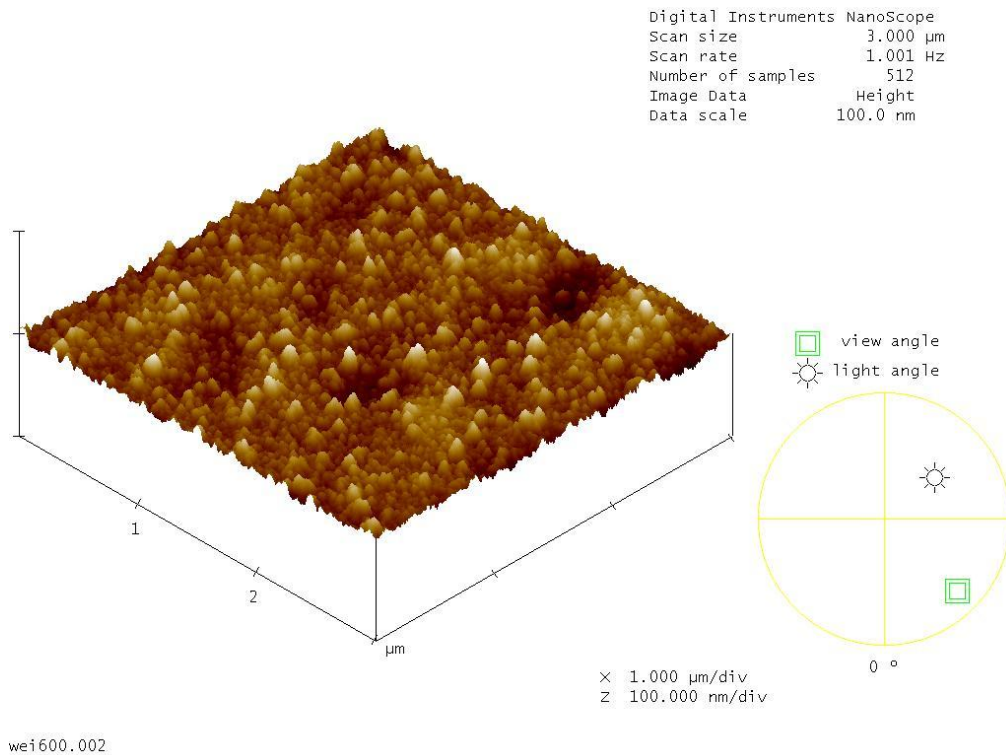
[Fig 3.1.1] Tilt AFM images of Co-Ti/Al catalyst growing nanoparticles during 5min at 700°C.
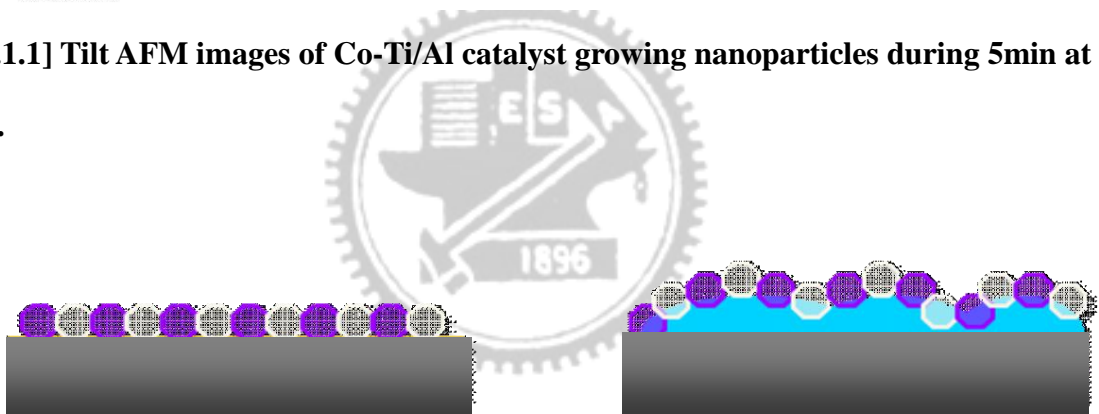
[Fig 3.1.2] The schematic profiles of thin film catalyst change into nano-sized particle (a) without Al buffer layer (b) with Al buffer layer.

Under 7.7 V/µm
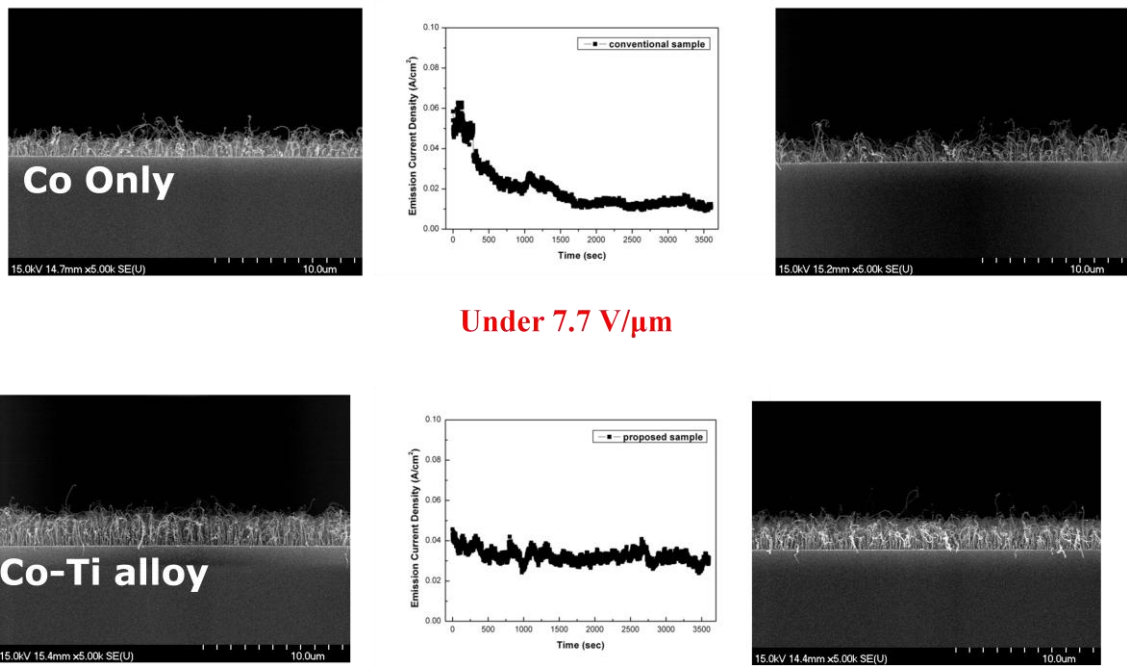
[Fig3.1.3] Co-deposition catalyst of Co and Ti improved reliability obviously
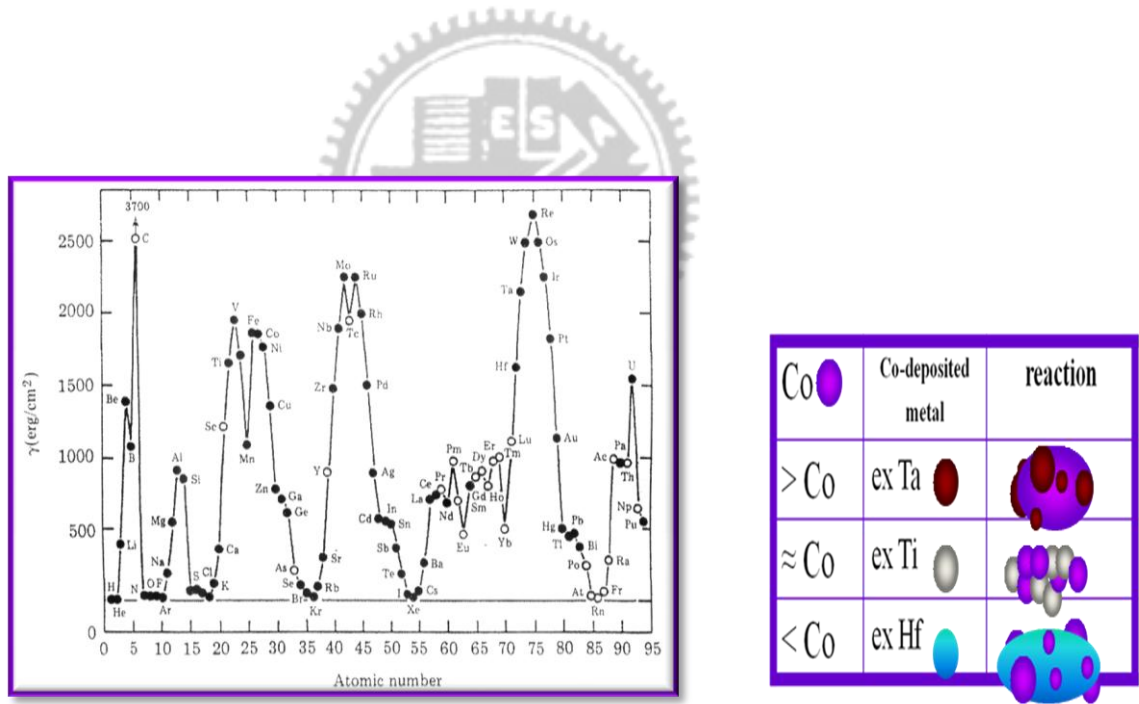
[Fig 3.1.4]The surface energy effected on interface reaction.

(a)
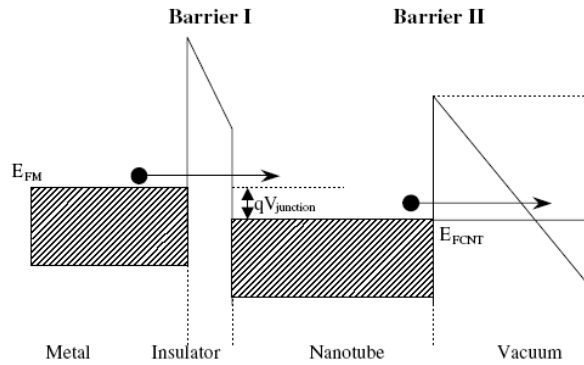
(b)
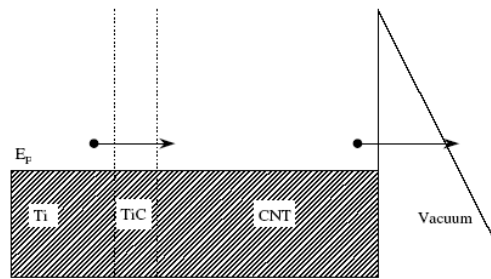
[Fig 3.1.5] (a) Band structure of double-barrier model for field emission of CNT films. E_FM and E_FCNT is the Fermi level of substrate metal and CNTs, respectively. V_junction is the voltage dropped on the substrate–CNTs junction.(b) Band structure of cathode for CNT films on titanium. The disappearing of interface barrier was due to formation of conductive TiC interlayer.
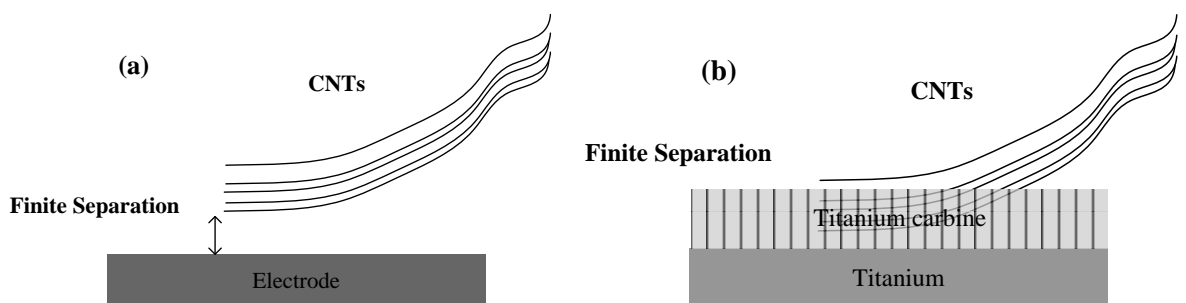
[Fig 3.1.6] Sketch for side-contact of CNT and electrode. (a) Electrons tunnel through

finite energy barrier created by oxide at CNT–metal interface. (b) Electrons can transport into CNT smoothly through conductive TiC layer at CNT–Ti interface.

(c)

15.0kV 15.1mm ×350 SE(U)   100um

15.0kV 14.8mm ×1.00k SE(U)   50.0um

10.1um

15.0kV 13.4mm ×2.00k SE(U)   20.0um

83.3um   10.6um

15.0kV 14.8mm ×300 SE(U)   100um

(d)

15.0kV 15.4mm ×300 SE(U)   100um

11.1um

15.0kV 14.7mm ×2.00k SE(U)   20.0um

15.0kV 14.7mm ×2.00k SE(U)   20.0um
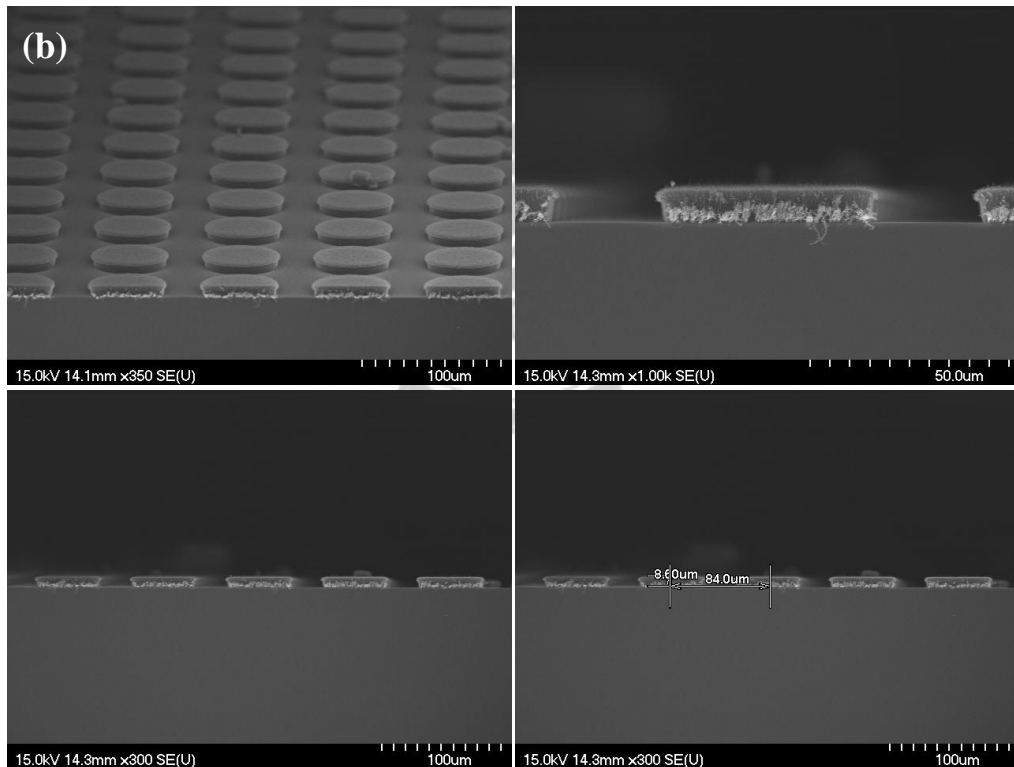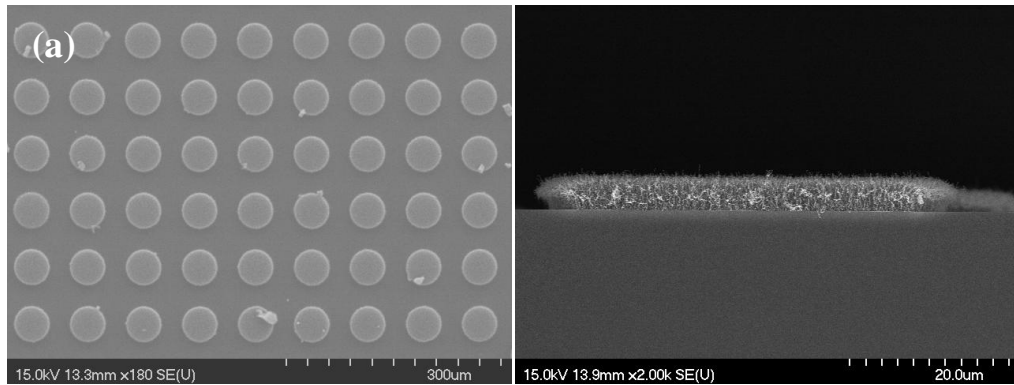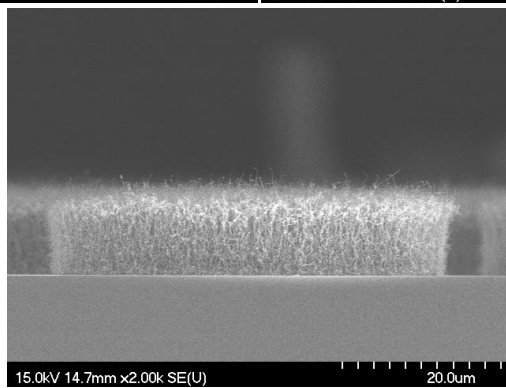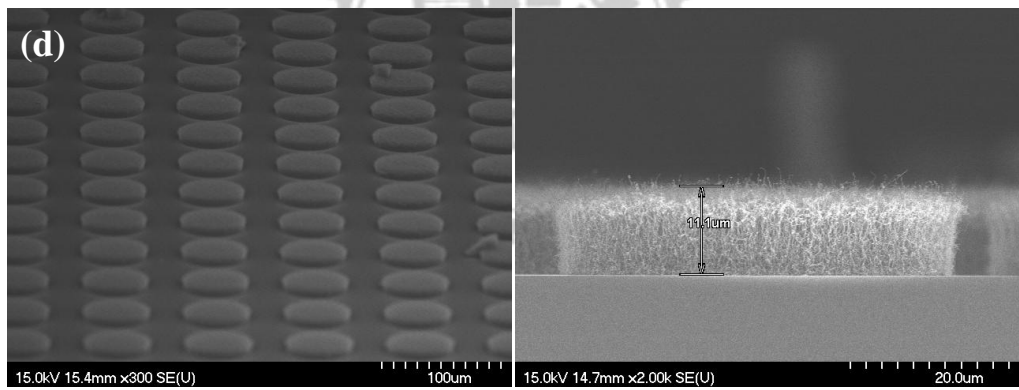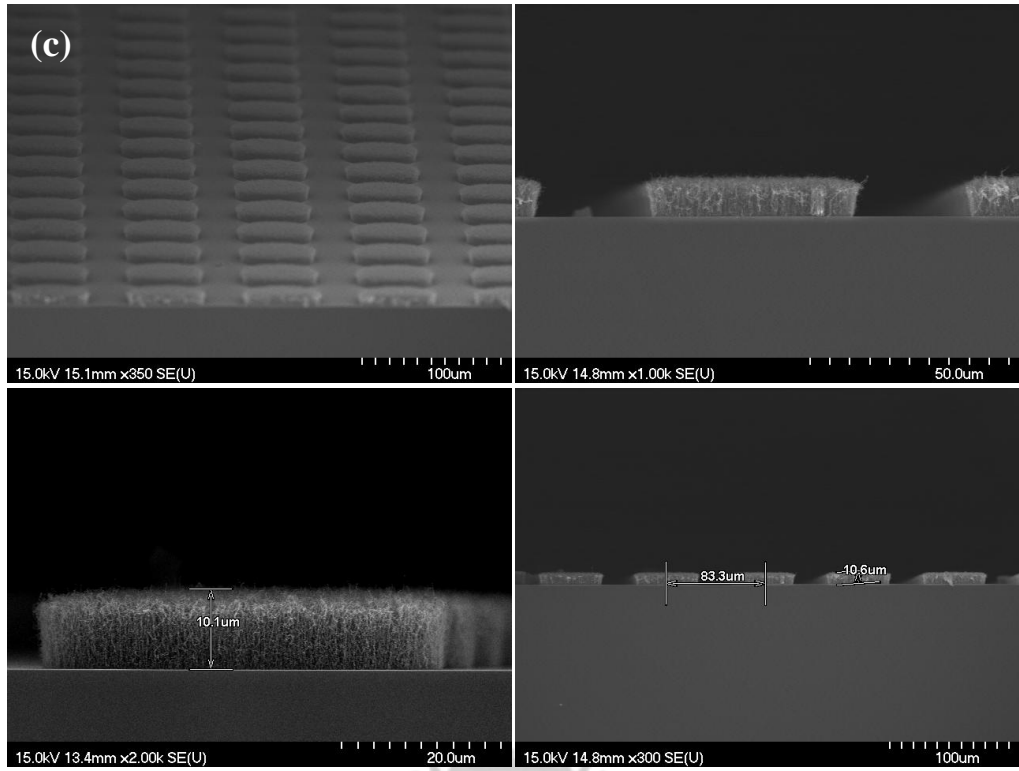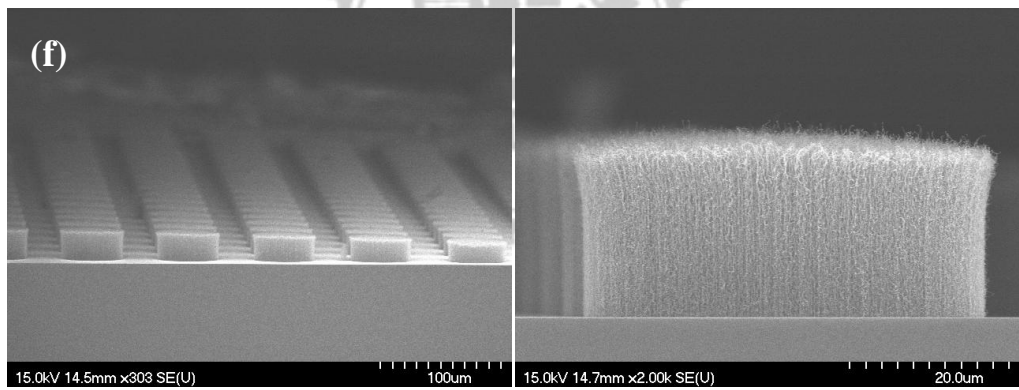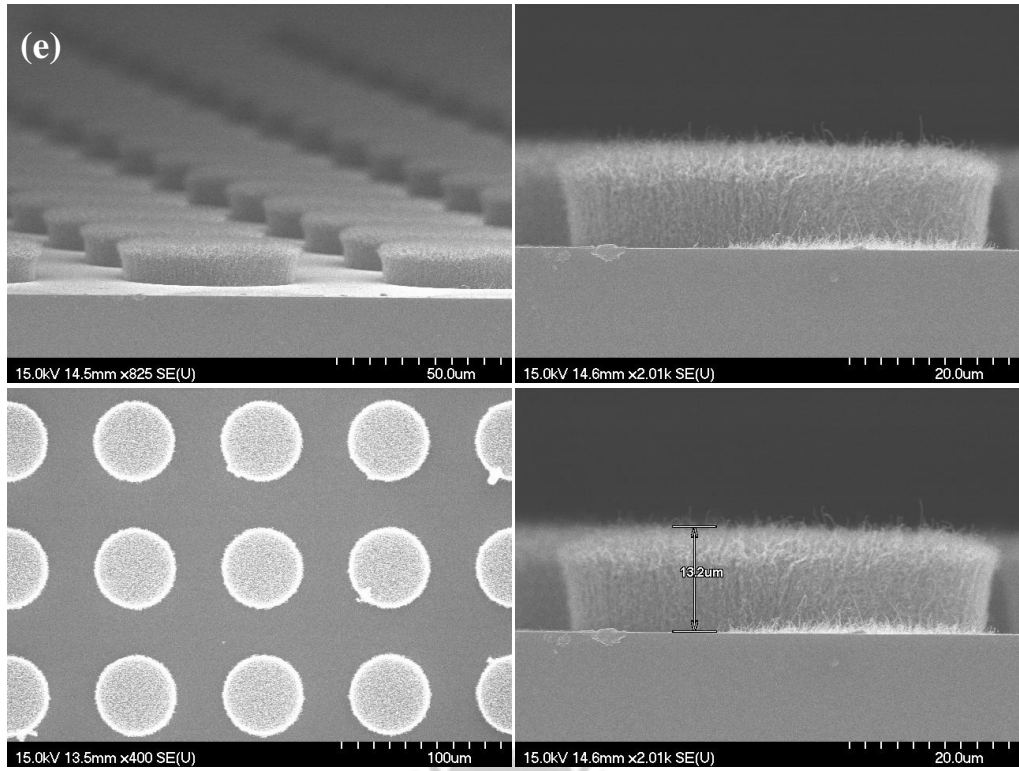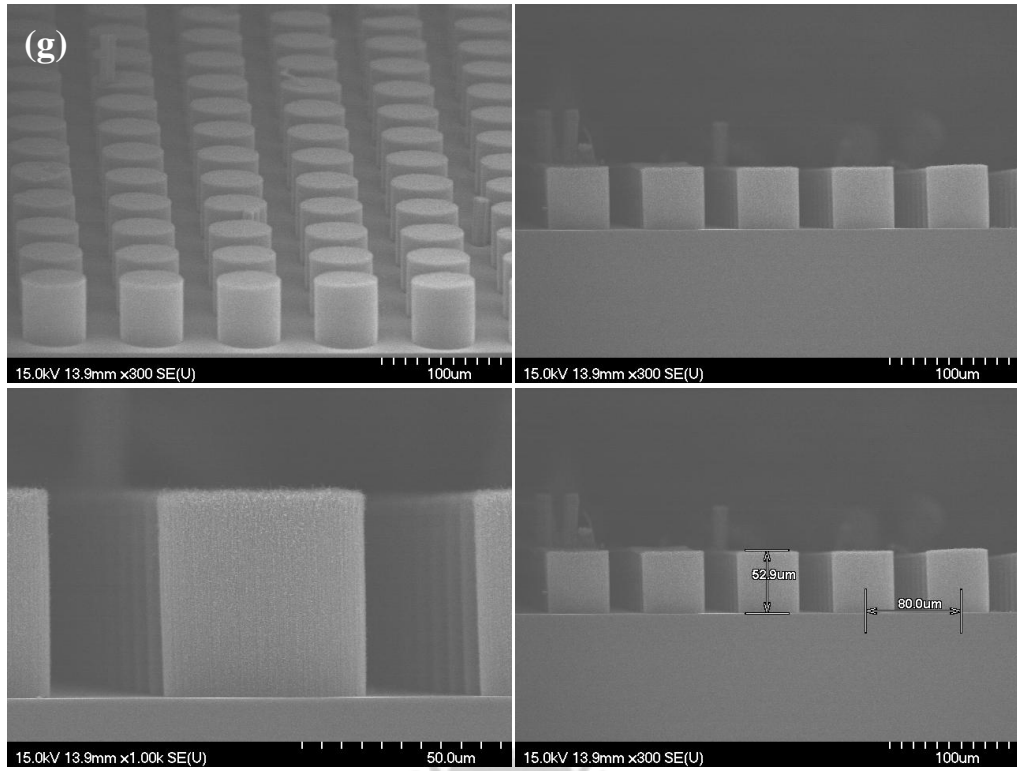
[Fig.3.2.1 (a)~(g)] SEM images of aligned CNT pillar array in inter-distance of 80μm.
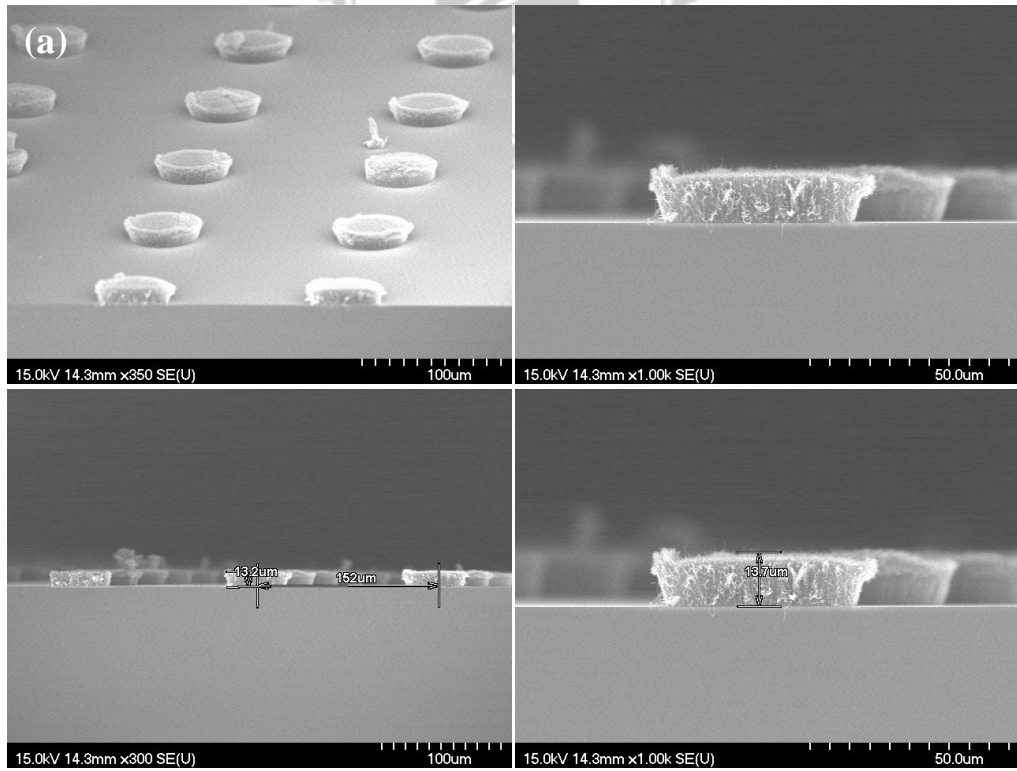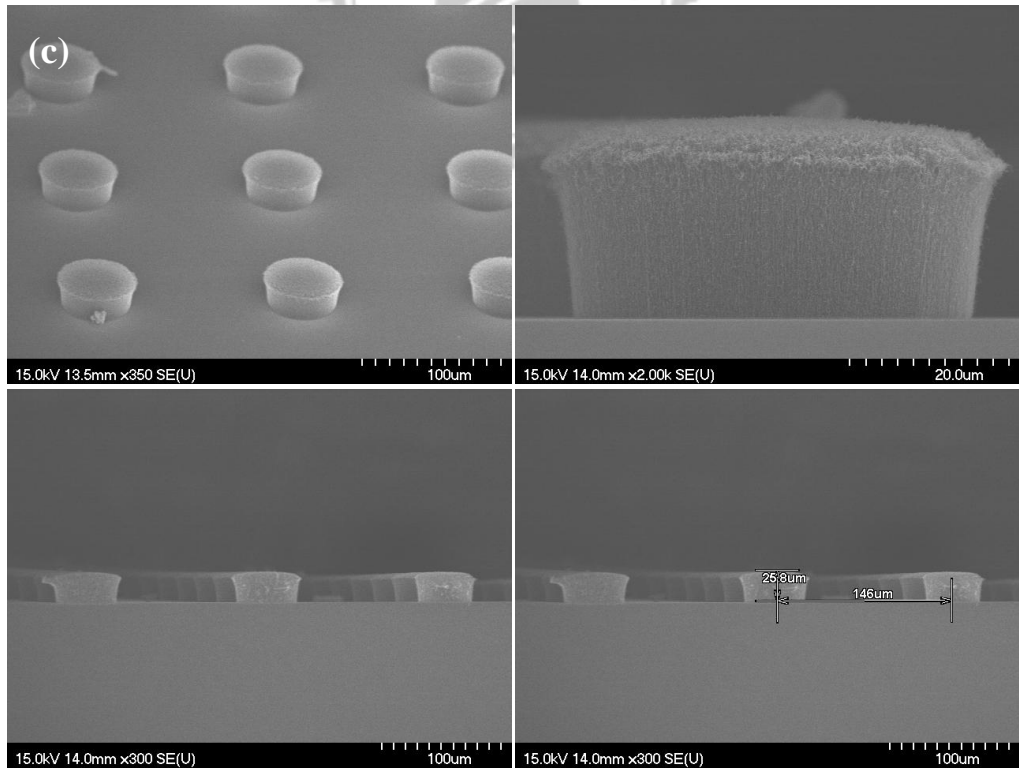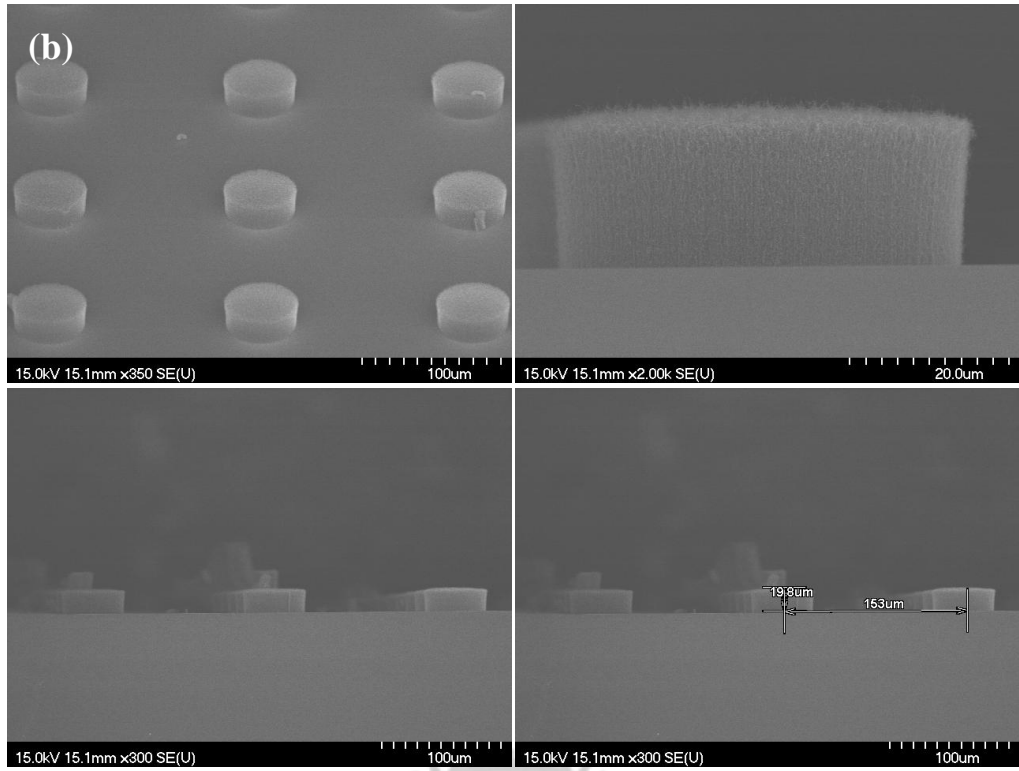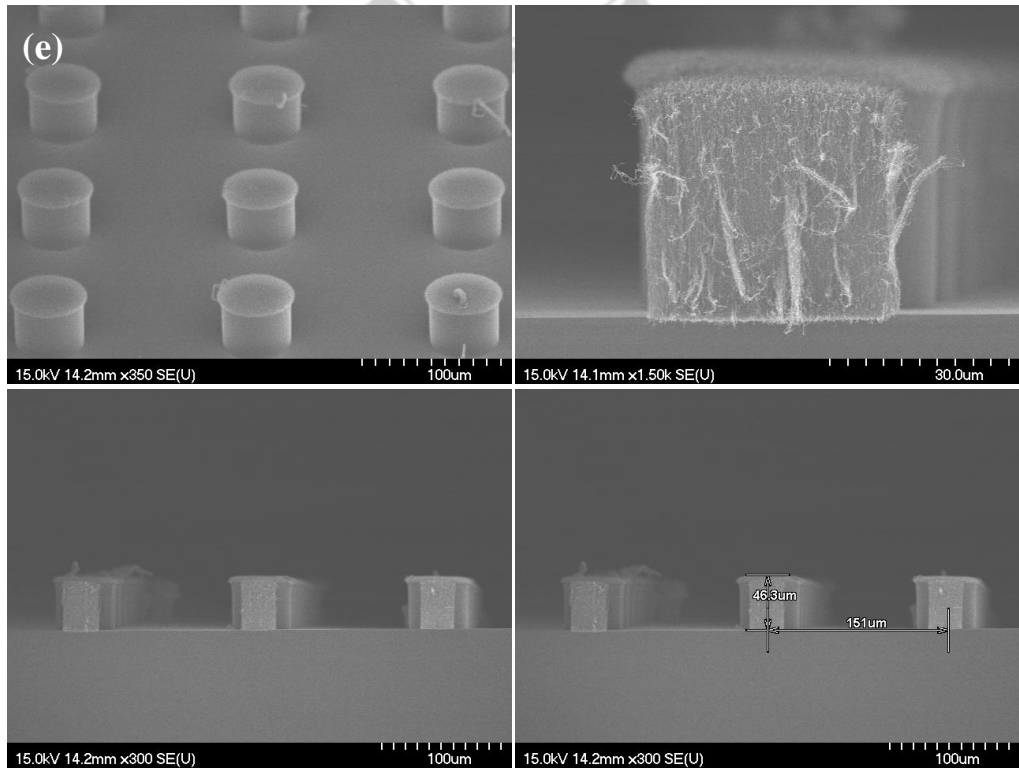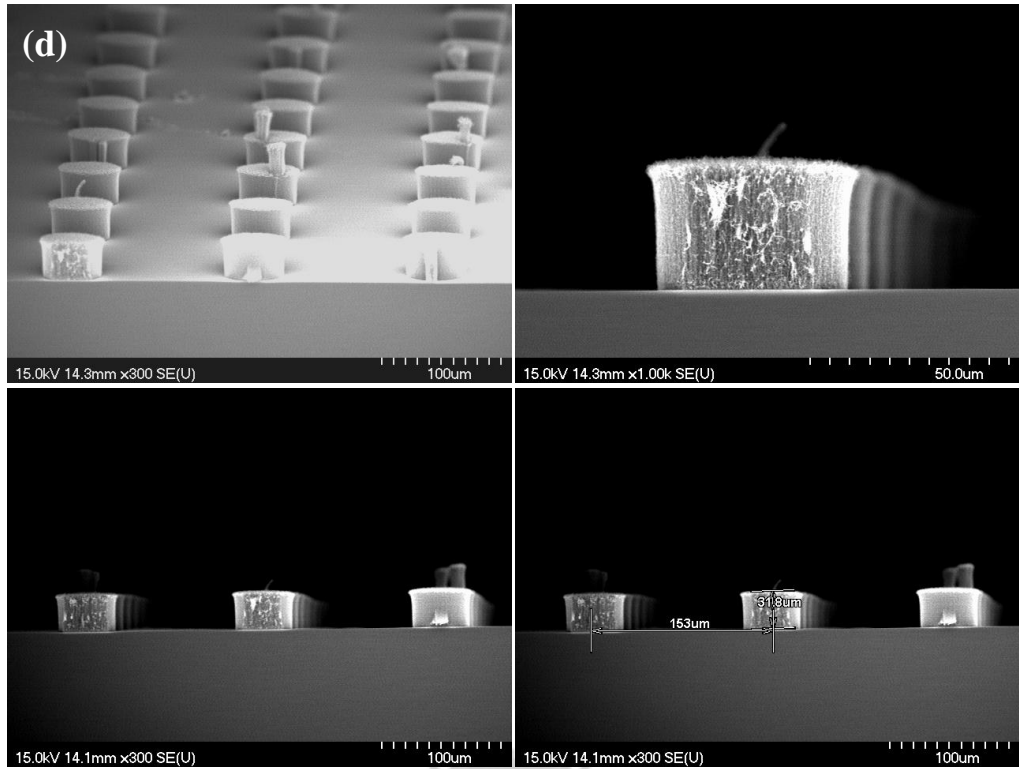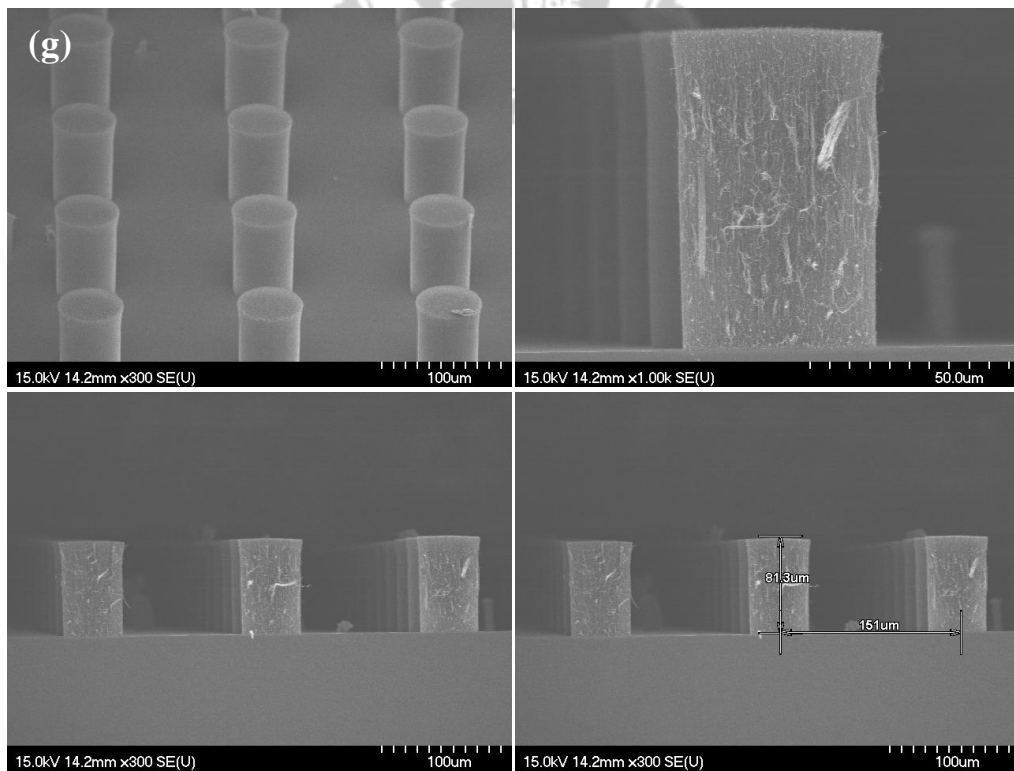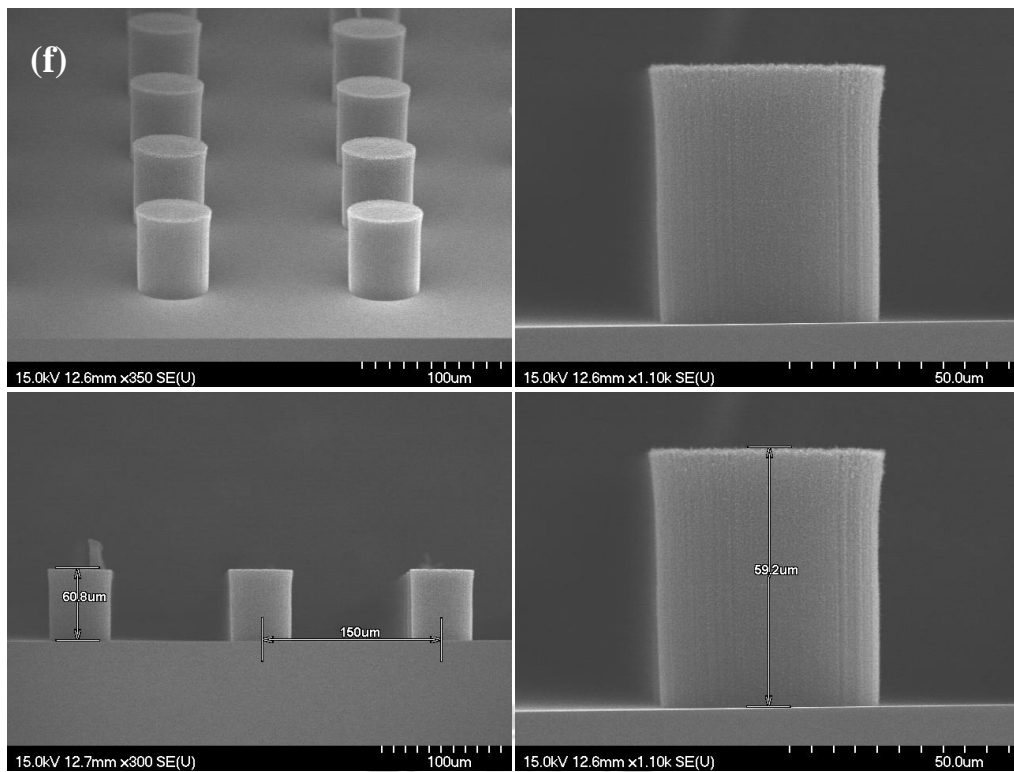
[Fig 3.2.2(a)~(g)]SEM image of aligned CNT pillar array in inter-distance of 150μ m.

(c)

15.0kV 14.1mm ×300 SE(U)   100um

15.0kV 14.1mm ×1.00k SE(U)   50.0um

15.0kV 14.1mm ×300 SE(U)   100um

50.3um
257um

15.0kV 14.1mm ×1.00k SE(U)   50.0um

49.6um

(d)

15.0kV 14.3mm ×300 SE(U)   100um

15.0kV 13.5mm ×800 SE(U)   50.0um

15.0kV 13.5mm ×300 SE(U)   100um

15.0kV 13.5mm ×300 SE(U)   100um

77.4um
255um
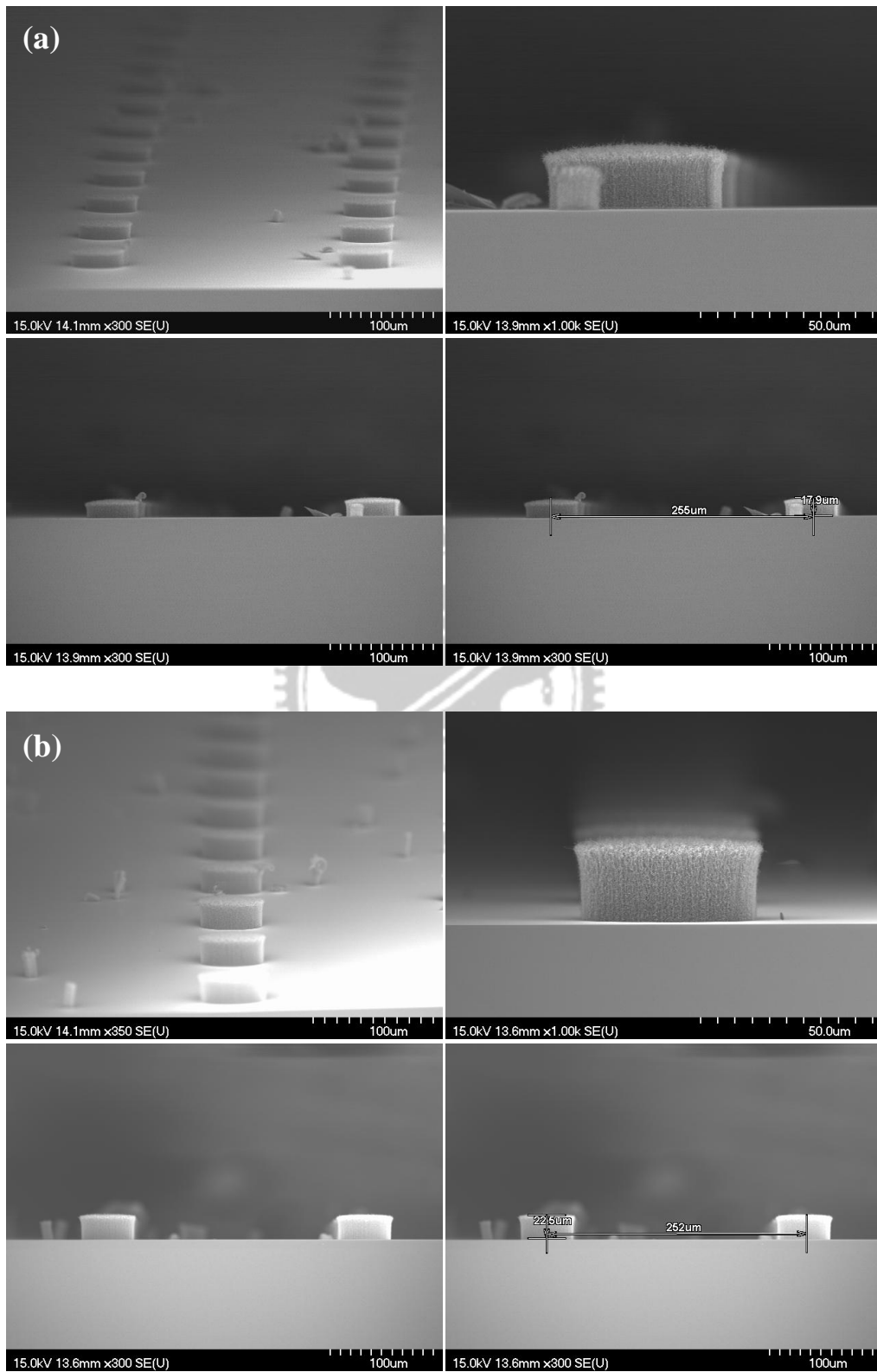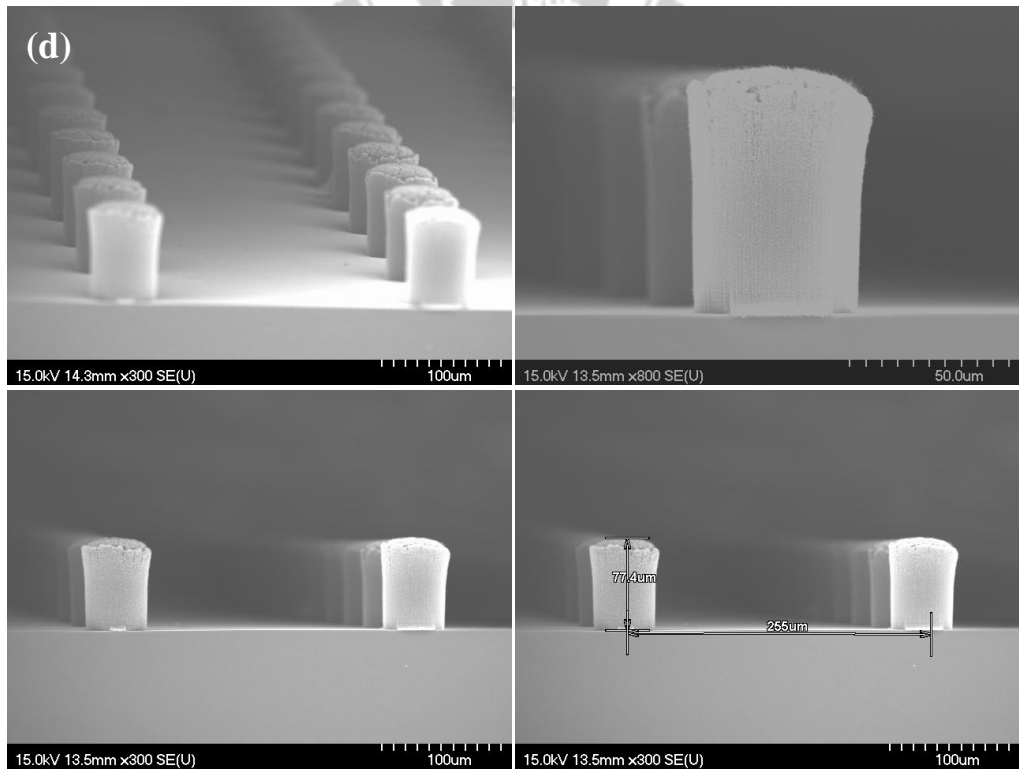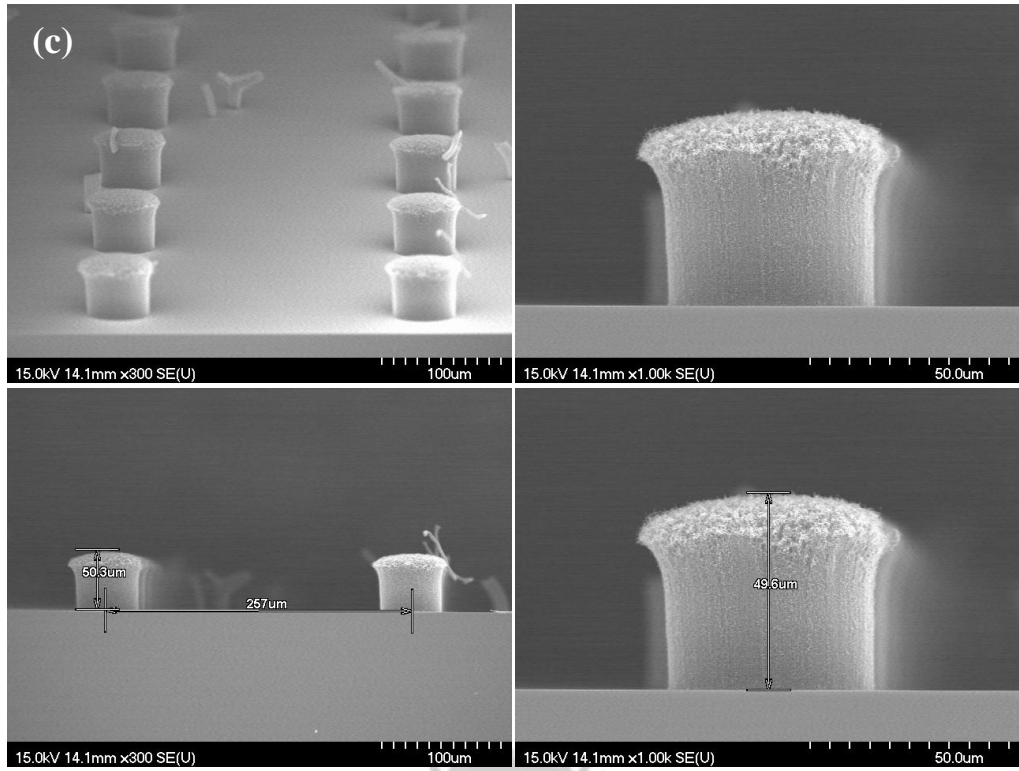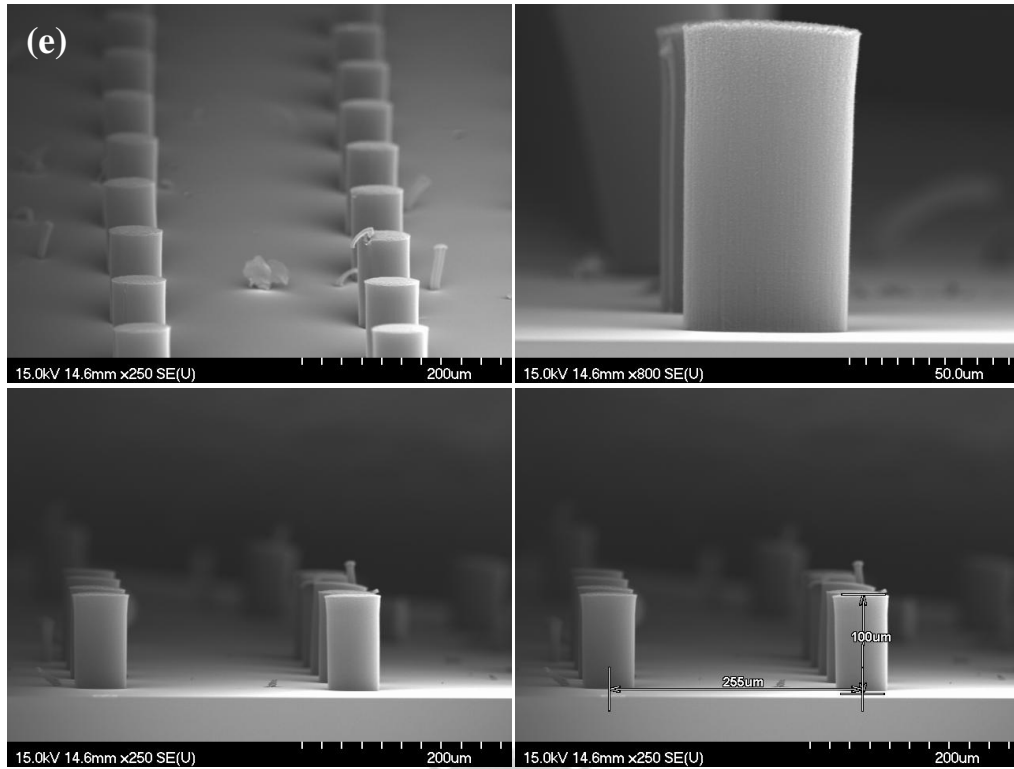
[Fig 3.2.3 (a)~(e)]SEM images of aligned CNT pillar array in inter-distance of 250μ m.
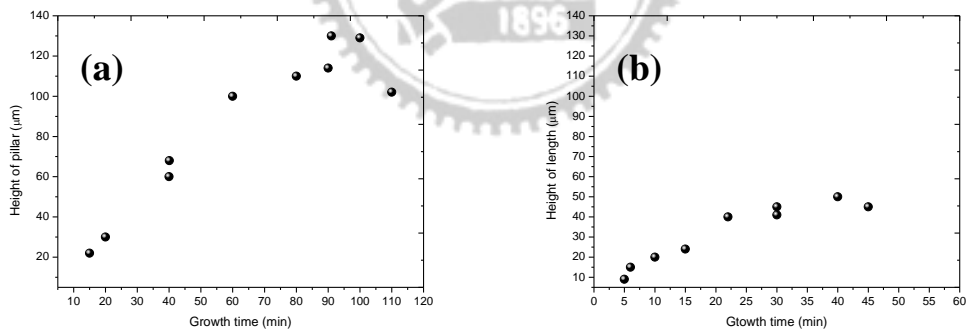
[Fig 3.2.4] Length of the aligned CNTs as a function of formation time (a) with 60sccm flow for C₂H₄, (b) with 135sccm flow for C₂H₄.
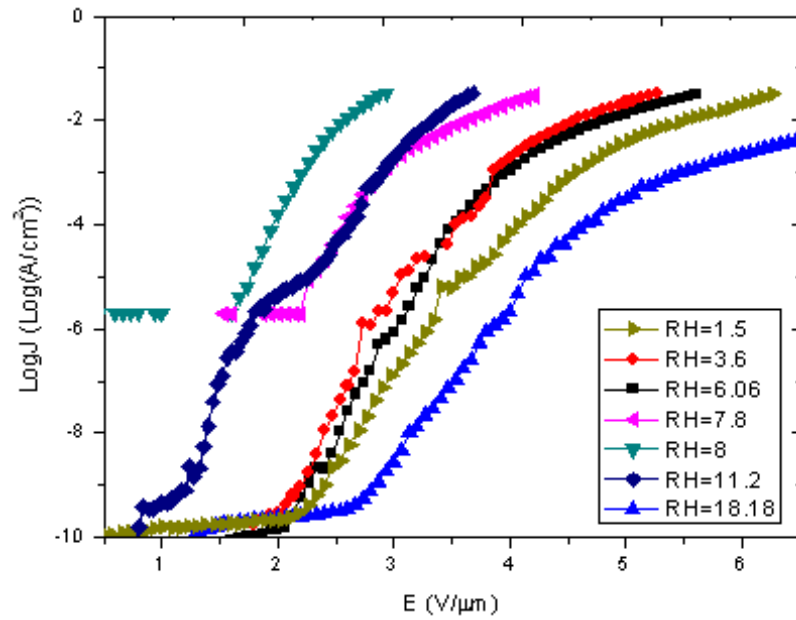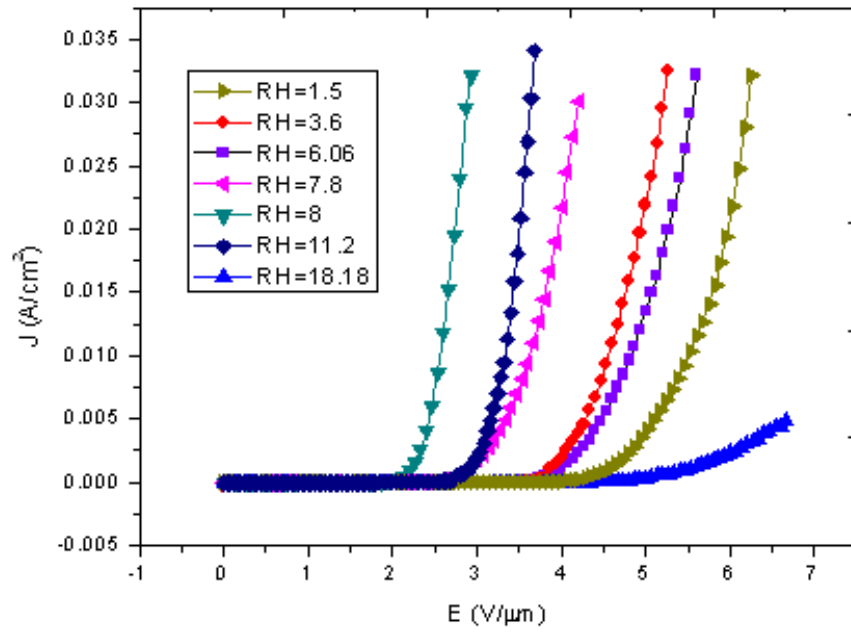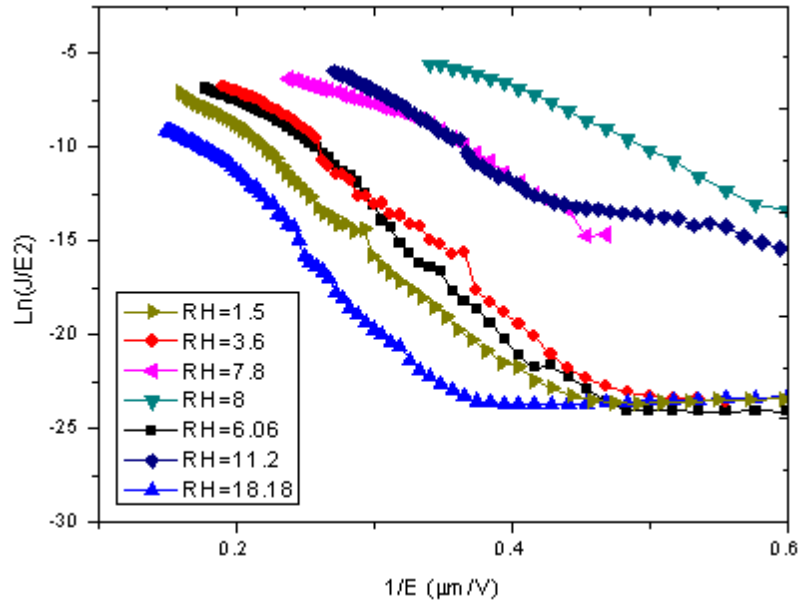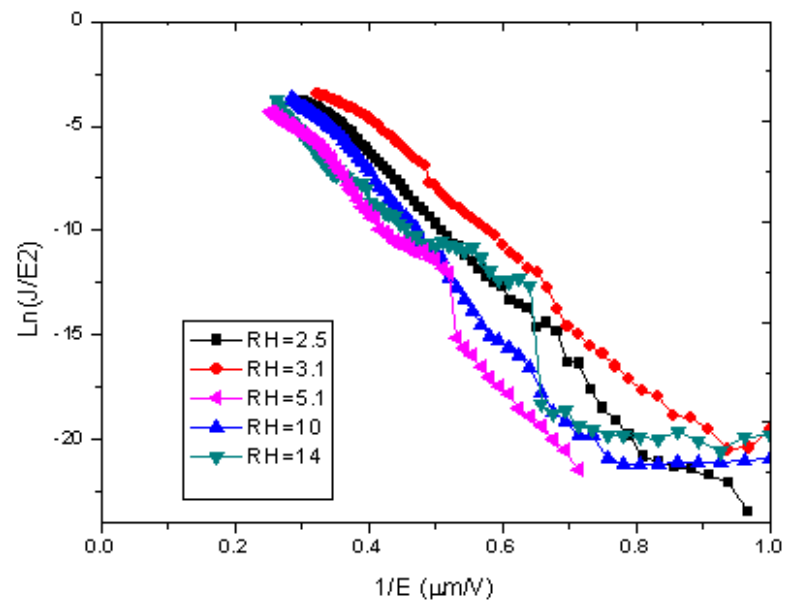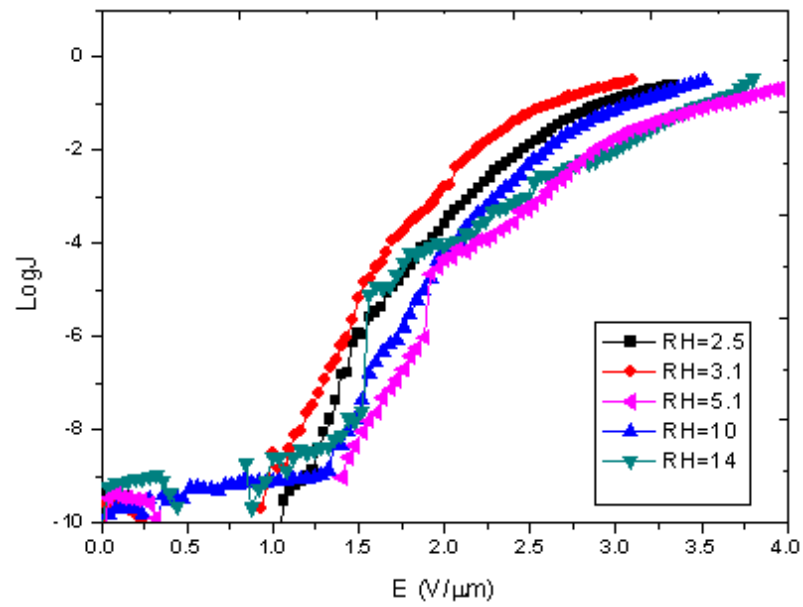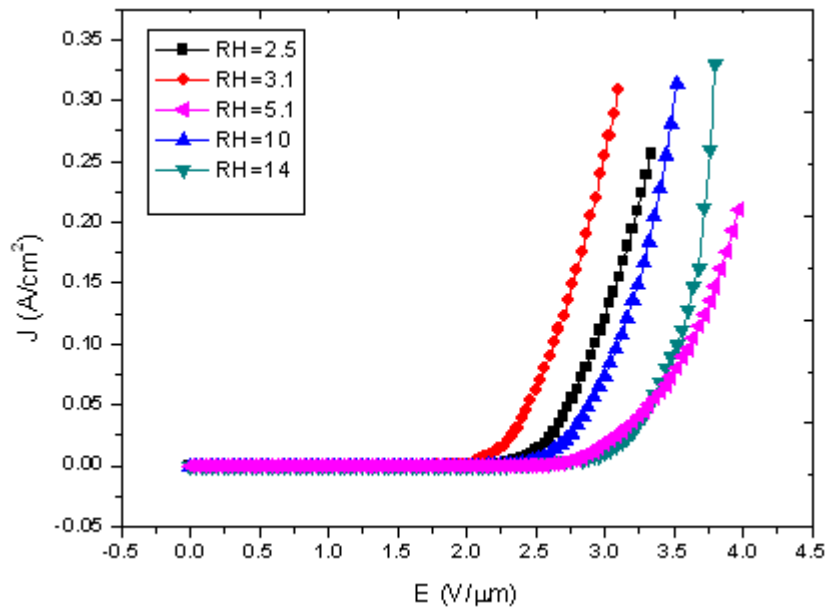
[Fig 3.2.5] **(a)Plot of the FE current density versus the applied electric field (b) current density in log scale versus the applied electric field (c) the corresponding F–N plots of CNT pillar array synthesized in pattern of inter-distance 80μ m .**
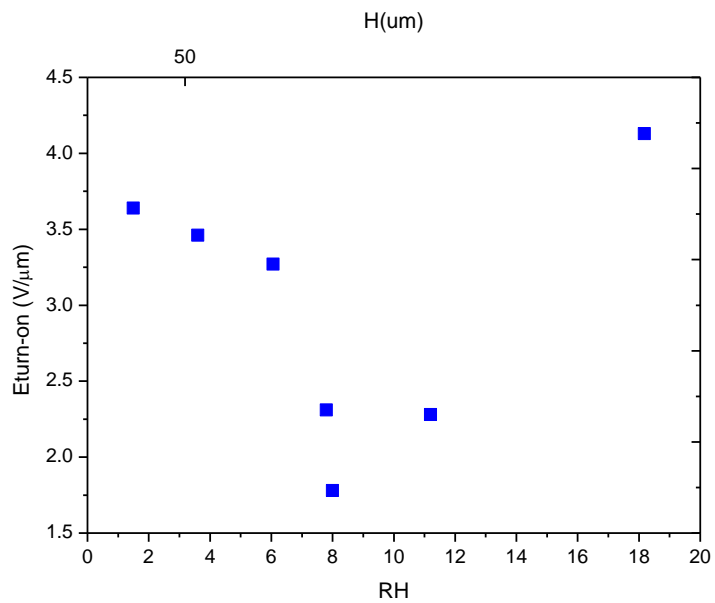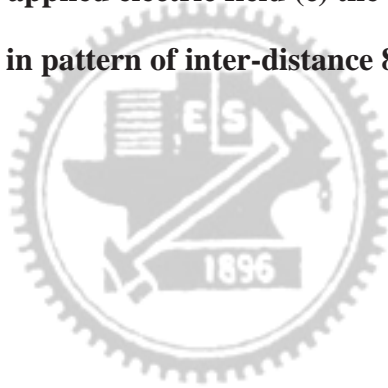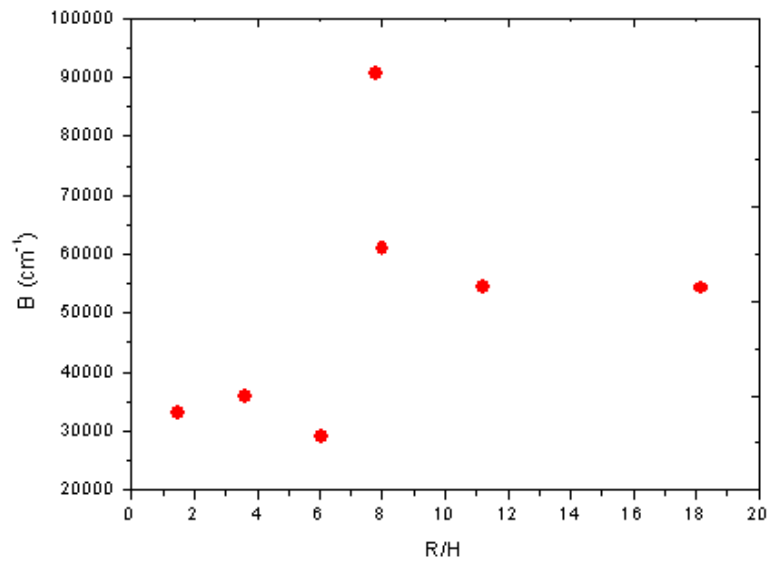
[Fig 3.2.6] Variation of (a) turn-on field (E_{to}) and (b) field-enhancement factor (β) with the ratio of inter-distance (80μm) to pillar height (H) .
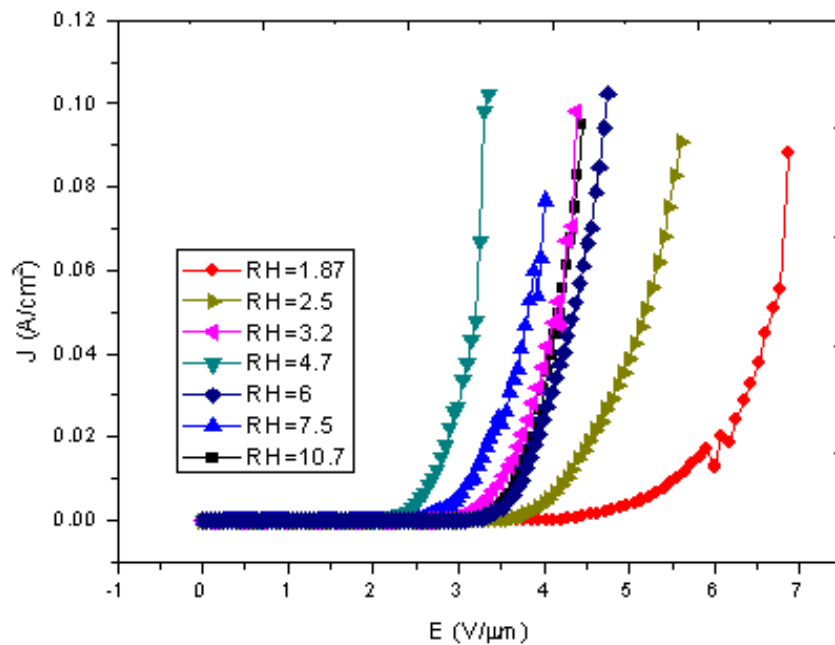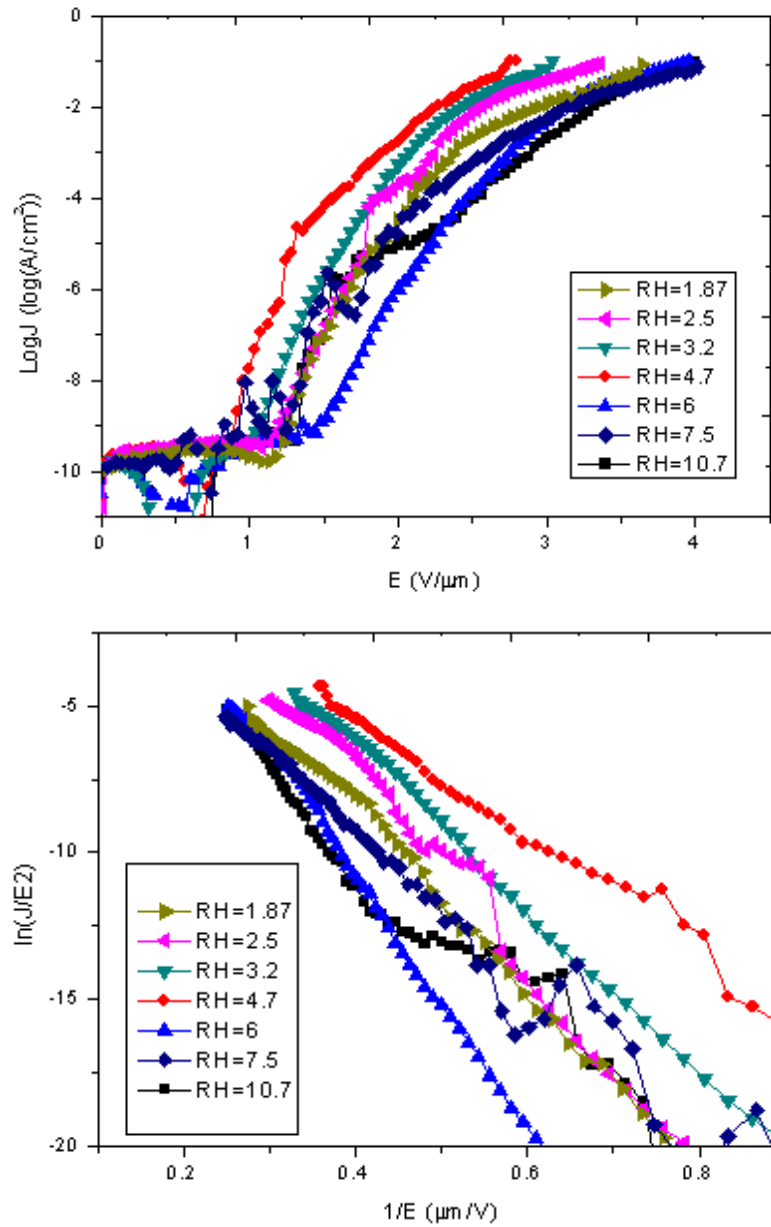
[Fig 3.2.7] **(a)Plot of the FE current density versus the applied electric field (b) current density in log scale versus the applied electric field (c) the corresponding F–N plots of CNT pillar array synthesized in pattern of inter-distance 150μm .**
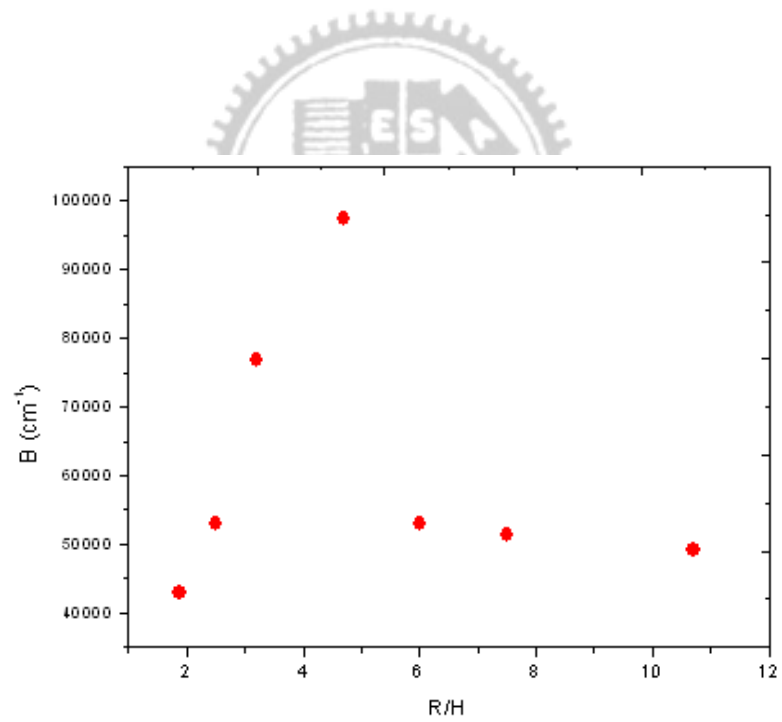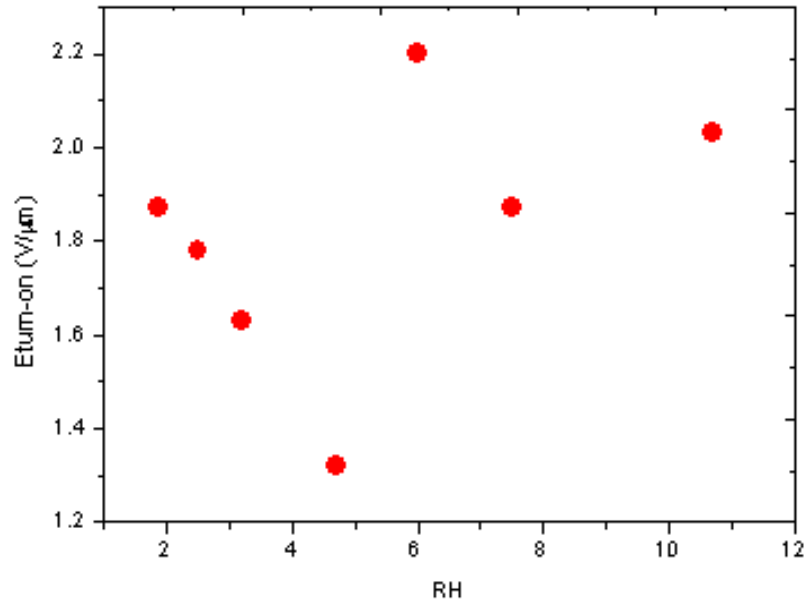
[Fig 3.2.8] Variation of (a) turn-on field (E_{to}) and (b) field-enhancement factor (β)

with the ratio of inter-distance (150µm) to pillar height (H) .

[Fig 3.2.9] **(a)Plot of the FE current density versus the applied electric field (b) current density in log scale versus the applied electric field (c) the corresponding F–N plots of CNT pillar array synthesized in pattern of inter-distance 250µm.**
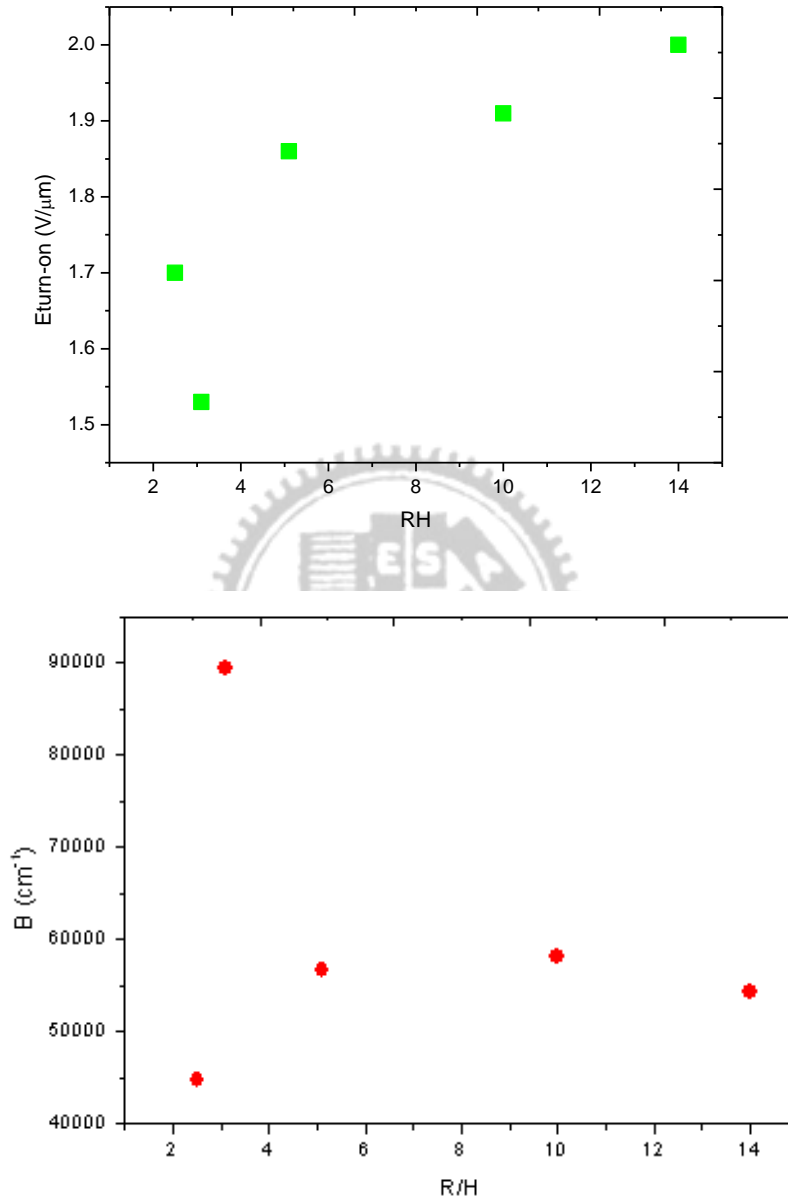
[Fig 3.2.10] Variation of (a) turn-on field (E_{to}) and (b) field-enhancement factor (β) with the ratio of inter-distance (250µm) to pillar height (H) .
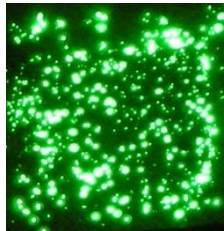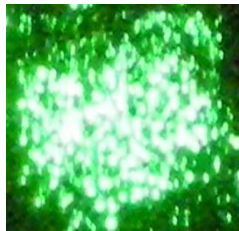
Ref. Diamond & Related Materials 17 (2008) 556–558
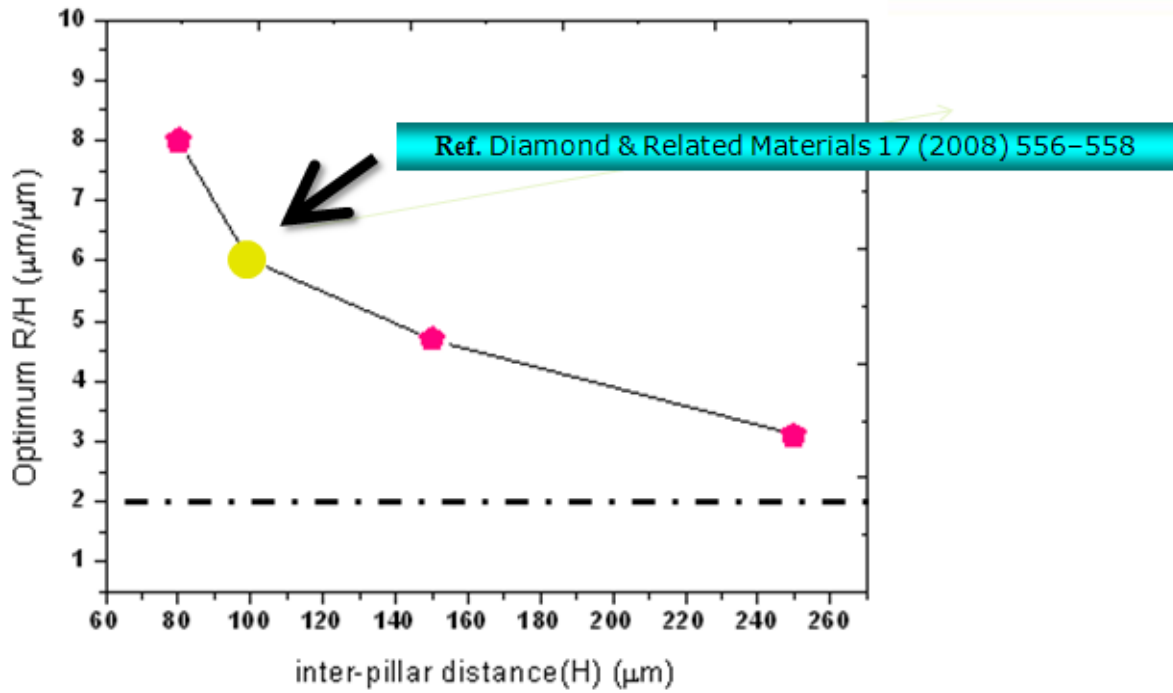
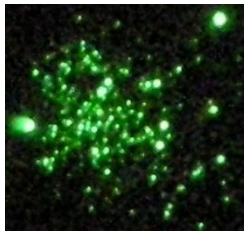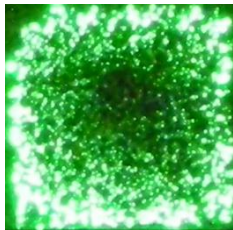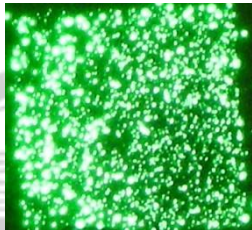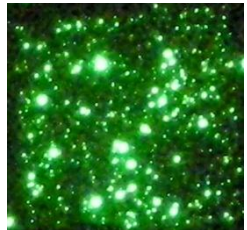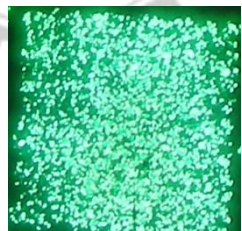[Fig 3.2.11]Optimal R/H value for inter-pillar distance ratio is approached to 2.
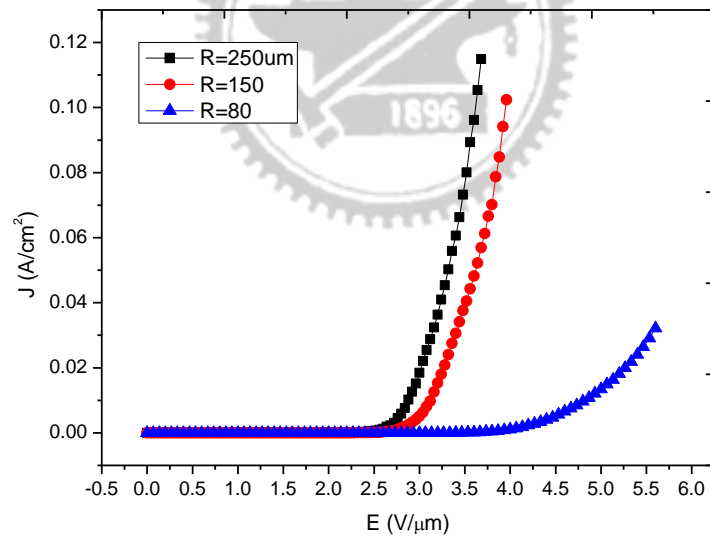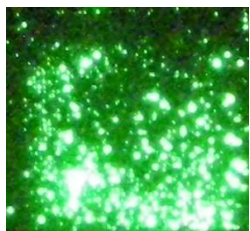
[Fig 3.2.12] Field emission property of different inter-pillar distances with R/H values of about 5.5

[Table3-2] Images of fluorescent screen monitoring the field electron emission from pillar array for three type patterns (10mm × 10mm) at an electric field of 2.5 V/μm.

D=80μm	R/H=1.5	R/H=8	R/H=11.2
Supplied electric field=2.5 V/μ m			

D=150μ m	R/H=1.87	R/H=4.7	R/H=10.7
Supplied electric field=2.5 V/μ m			

D=250μ m	R/H=2.5	R/H=3.1	R/H=13.9
Supplied electric field=2.5 V/μ m			
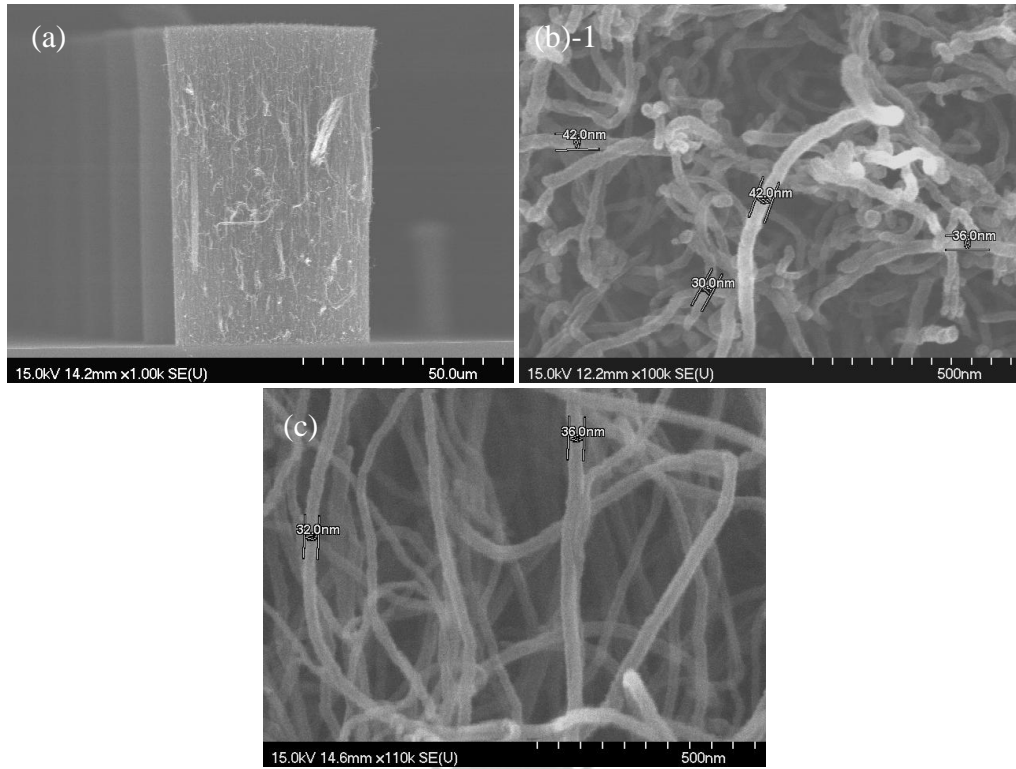
[Fig 3.3.1] SEM images for directly growing method (a) the height of pillar is about 80μm (b)-1,2 the range of CNTs' diameter is from 32 to 42μm.
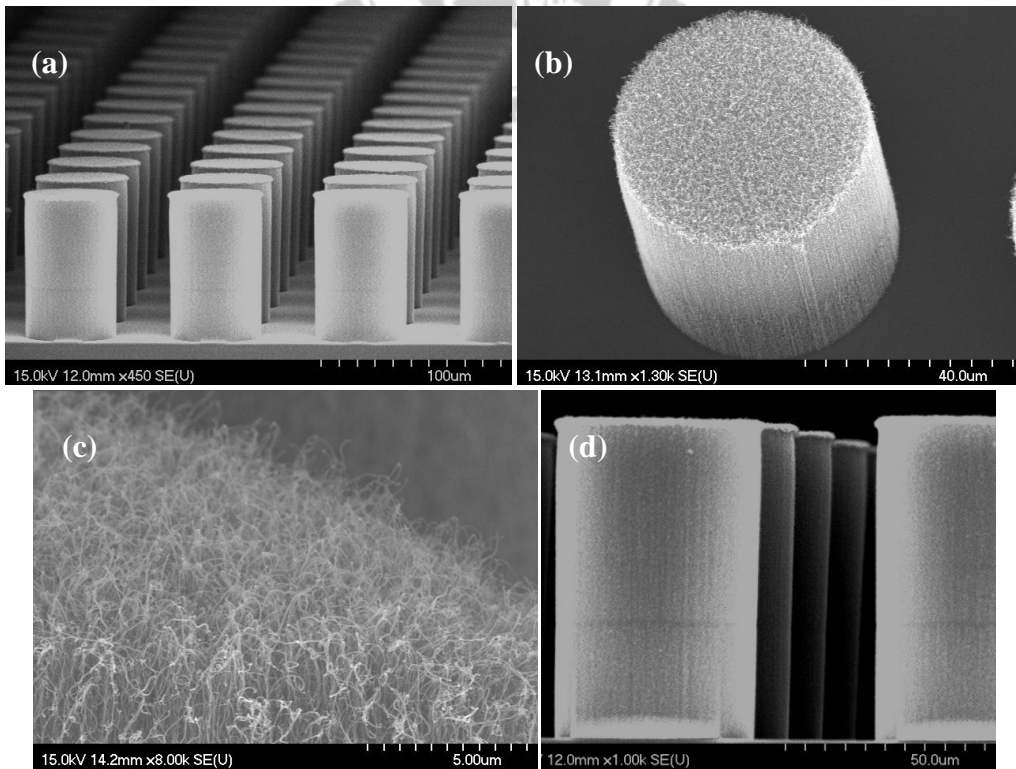
[Fig 3.3.2] SEM images for two-step growing method (a) the height of pillar is about 80μm (b)the bird's eye view image for a pillar (c) the tilted image at the tip of a pillar (d) a joint connect first-time to second-time, obviously.
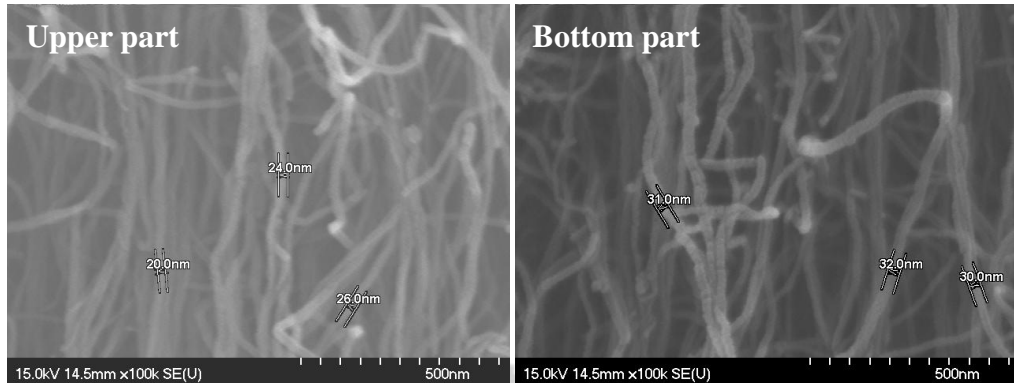
[Fig 3.3.3] SEM images for two-step growing method the range of upper part's diameter is form 20 to 26μm and the range of bottom part's diameter is above 30μm.
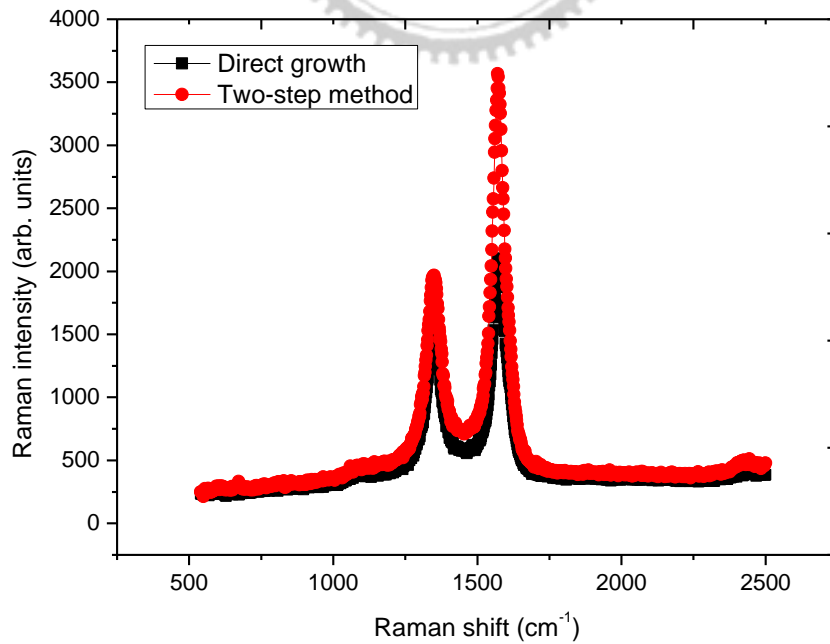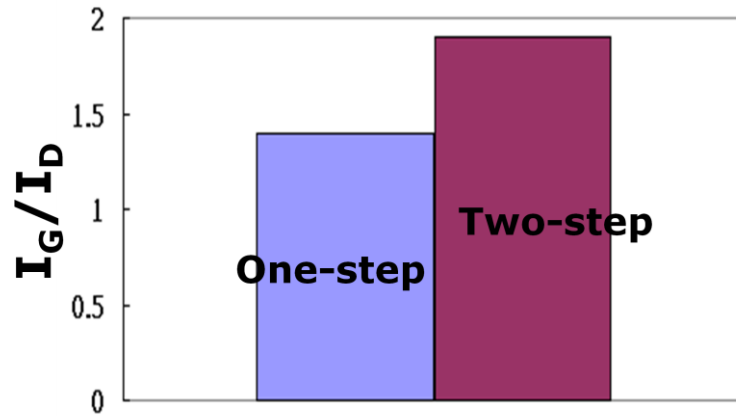
[Fig 3.3.4] The Raman spectra of direct growth CNT pillar and two-step growth CNT pillar array. The *IG/ID* ratio indicates the increasing of the graphite in the CNT pillar array after two-step growth method.

(b)

(c)
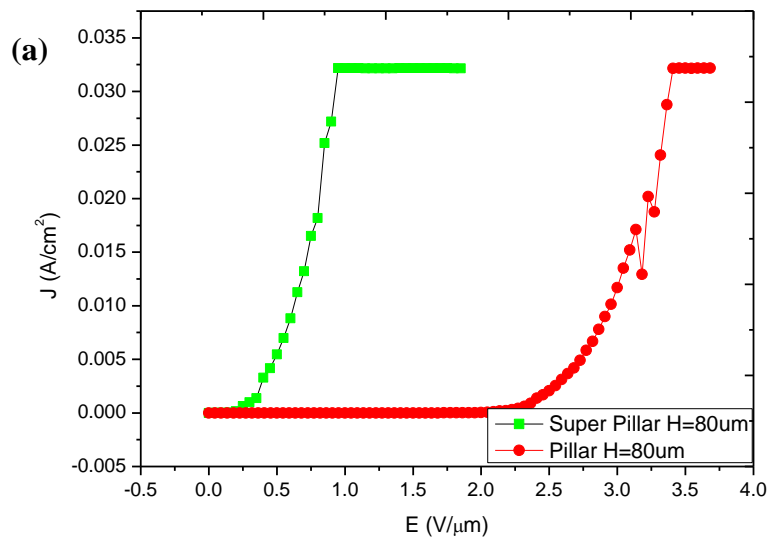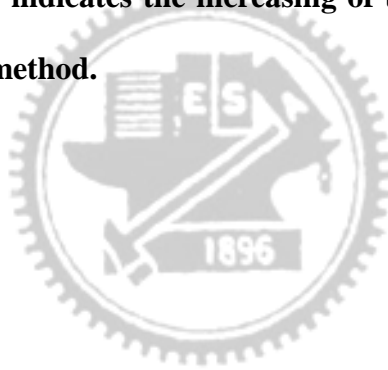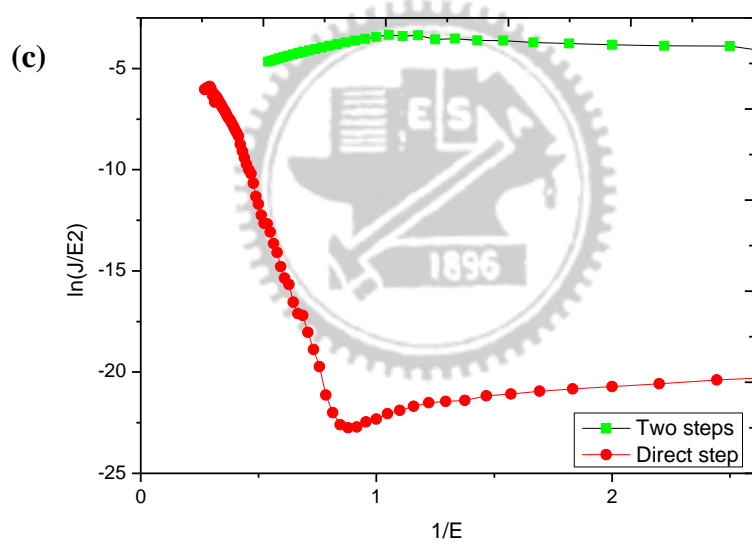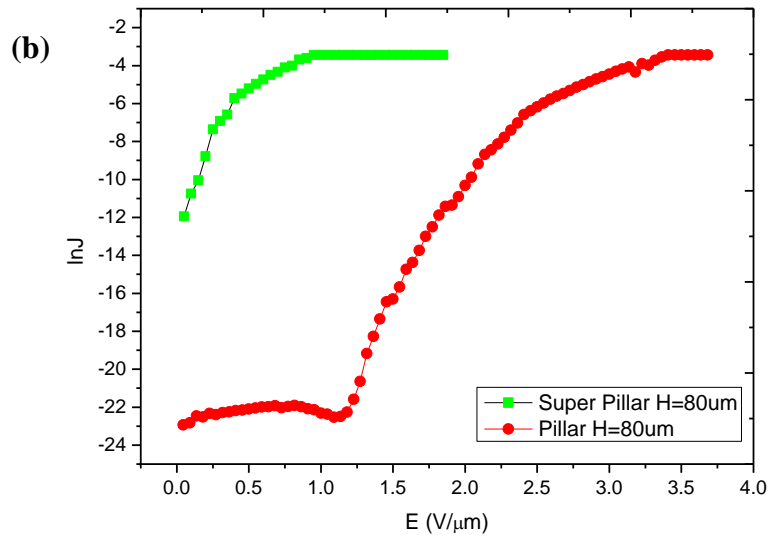
[Fig 3.3.5] Field emission properties of pillars of aligned CNT bundles: (a) current density-electric field plot, (b) current density in log scale versus electric field plot and (c) Fowler-Nordheim plot.

[Fig 3.3.6]   Image of fluorescent screen monitoring the field electron emission from the pillar array (10mm × 10mm) at an electric field of 0.66 V/µm.
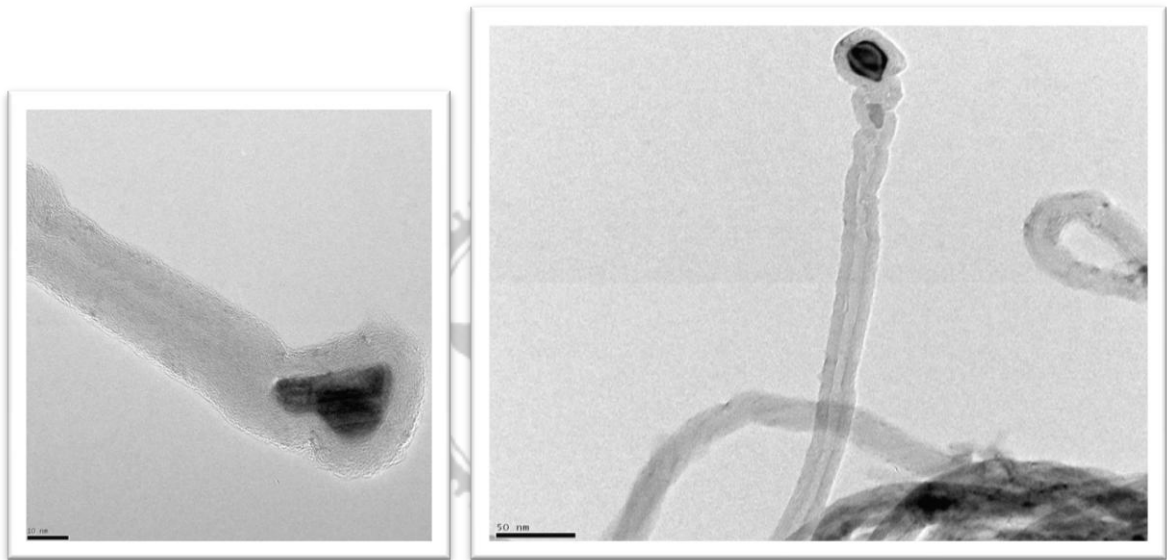
[Fig 3.3.7] TEM images of a carbon nanotube.
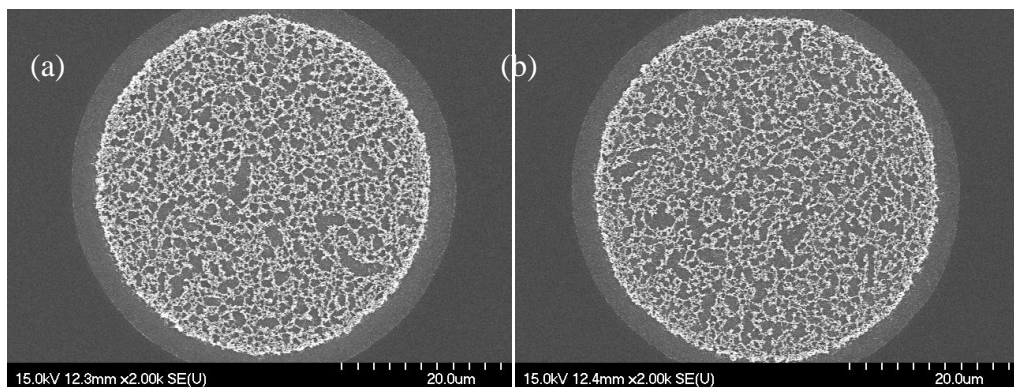
[Fig 3.4.1] SEM images after post-treatment of pure oxygen in the top view (a) 2min (b) 10min.
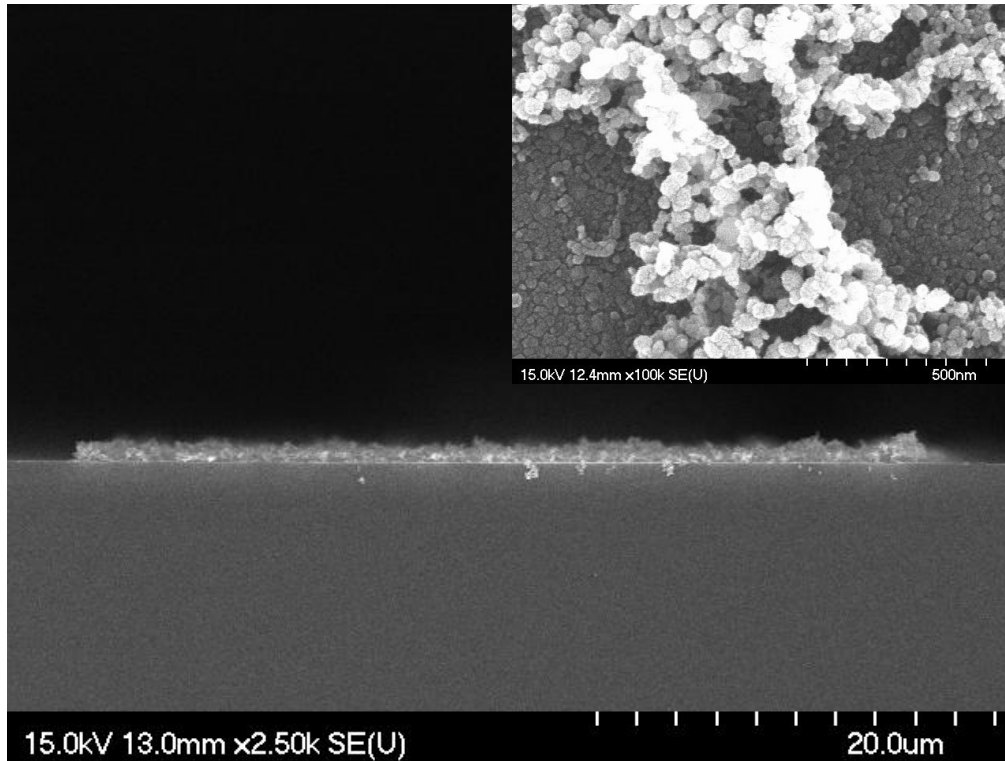
[Fig 3.4.2] SEM images after post-treatment of pure oxygen in the cross-section view. The inset image is oxide carbon compound.
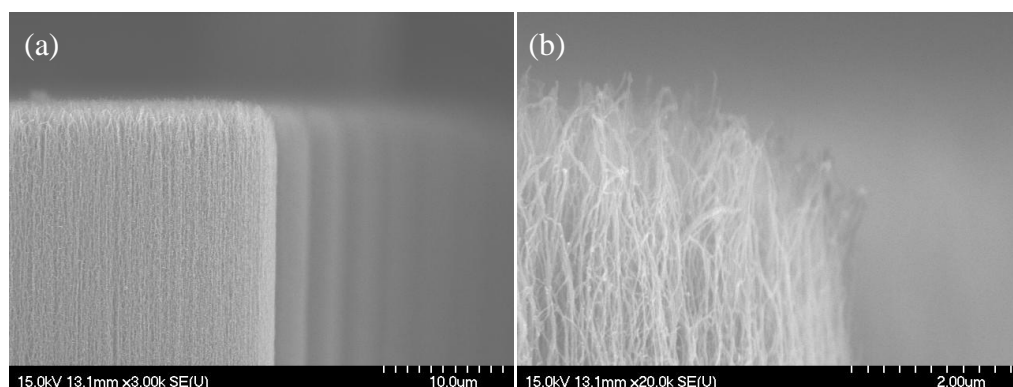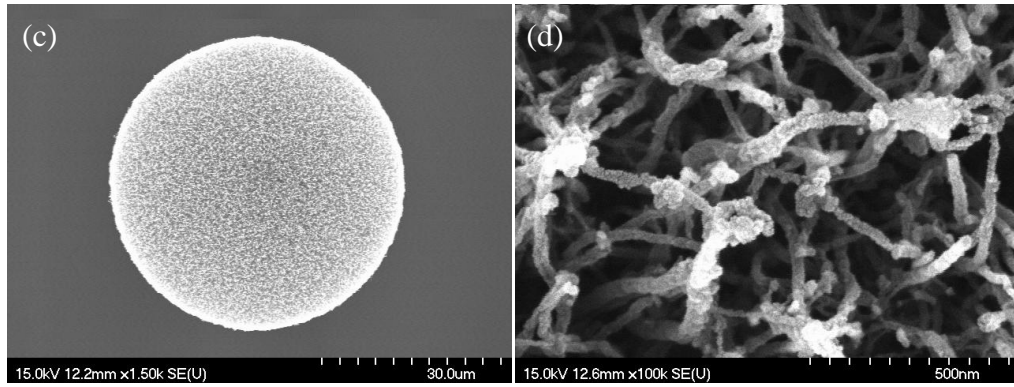
[Fig 3.4.3] SEM images after post-treatment of oxygen mix chlorine for 2 min (a) (b) in the tilt view (c) in the top view (d) oxygen mix chlorine compound around the CNTs.
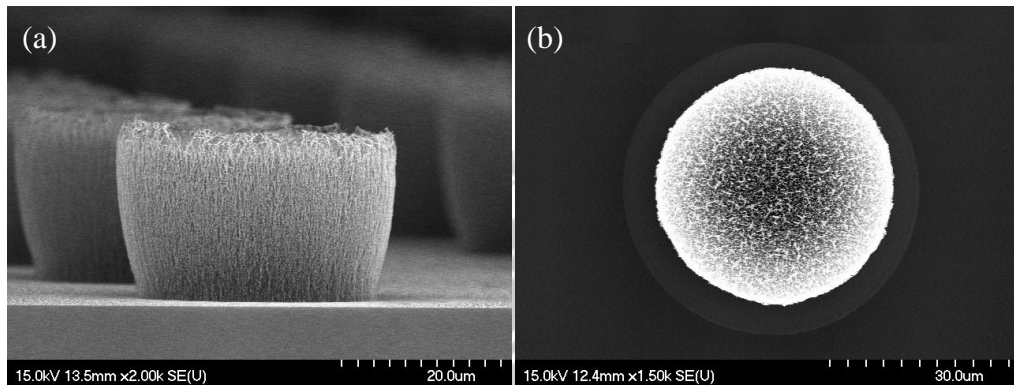
[Fig 3.4.4] SEM images after post-treatment of oxygen mix chlorine for 3 min (a) in the tilt view (b) in the top view.
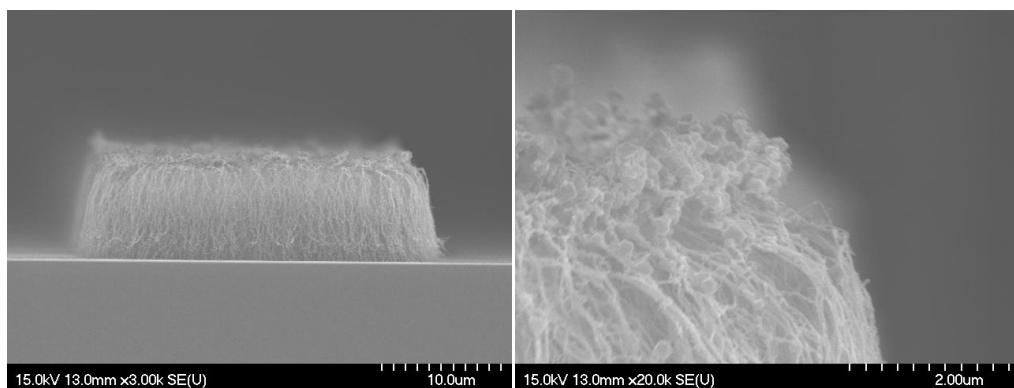
[Fig 3.4.5] SEM images after post-treatment of oxygen mix chlorine for 5 min (a) in the cross-section view (b) at the tip of the pillar.
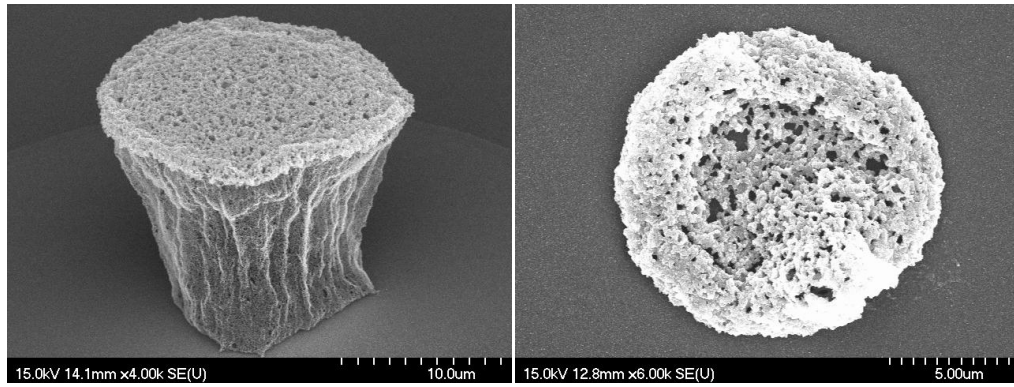
[Fig 3.4.6] SEM images after post-treatment of oxygen mix chlorine for 10 min (a) in the tilt view (b) in the top view.
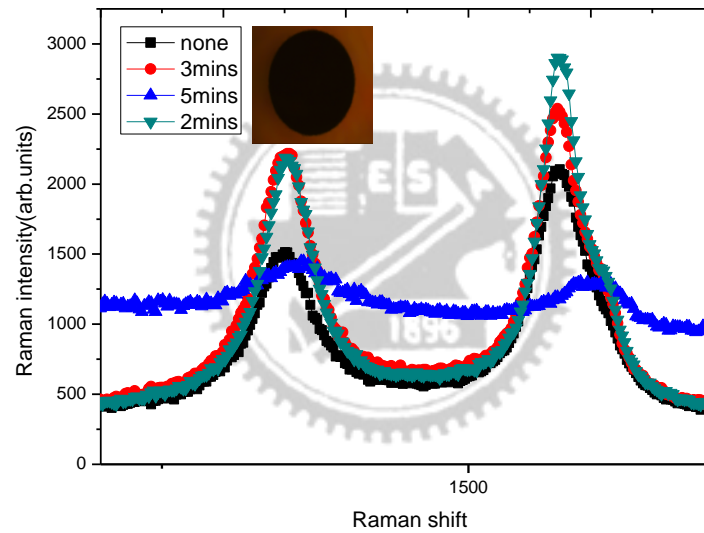
[Fig 3.4.7]Raman spectra of pillar sample after O_2 mix Cl_2 plasma post-treatment obtained using 514.5nm excitations. The inset image is an optic microscope image at the top of a pillar.

Table 3-3

Summary of Raman spectra for an as grown and CNT pillar array after O$_2$ mix Cl$_2$ plasma treatment.

Raman analysis				
Treatment time (min)	*0*	*2*	*3*	*5*
I$_G$/I$_D$	*1.47*	*1.22*	*1.08*	*0.82*
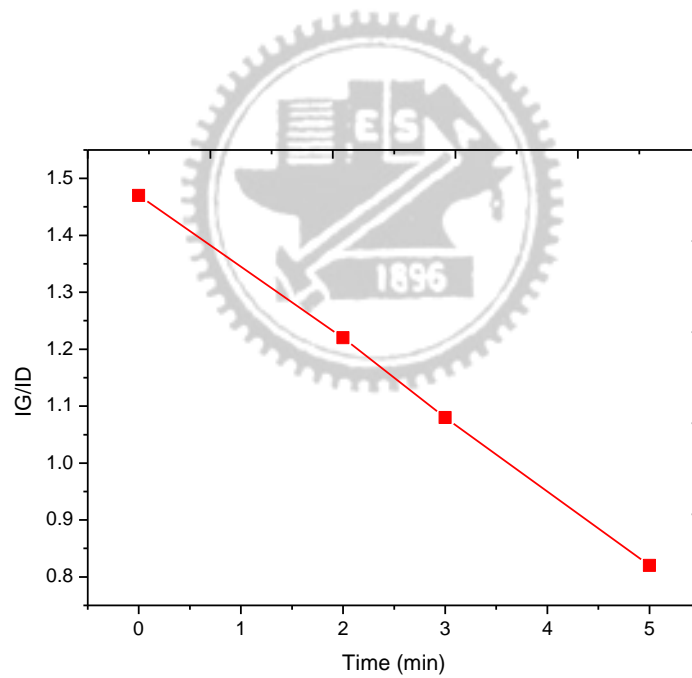
[Fig 3.4.8] Plot of the I$_G$/I$_D$ versus the time for O$_2$ plus Cl$_2$ plasma post-treatment.

Table 3-4

EDS analysis

Treatment time(min)	Element factor	Co	Cl	O	Ti
2	Atom(%)	0.23	0.1	0.18	0.00
	Element Wt (%)	1.13	0.3	0.24	0.00
3	Atom(%)	0.19	0.12	1.05	0.00
	Element Wt (%)	0.74	0.28	1.10	0.00
5	Atom(%)	0.14	0.20	2.24	0.00
	Element Wt (%)	0.42	0.97	2.31	0.00
10	Atom(%)	12.56	4.13	31.31	0.97
	Element Wt (%)	33.68	6.66	22.79	8.98
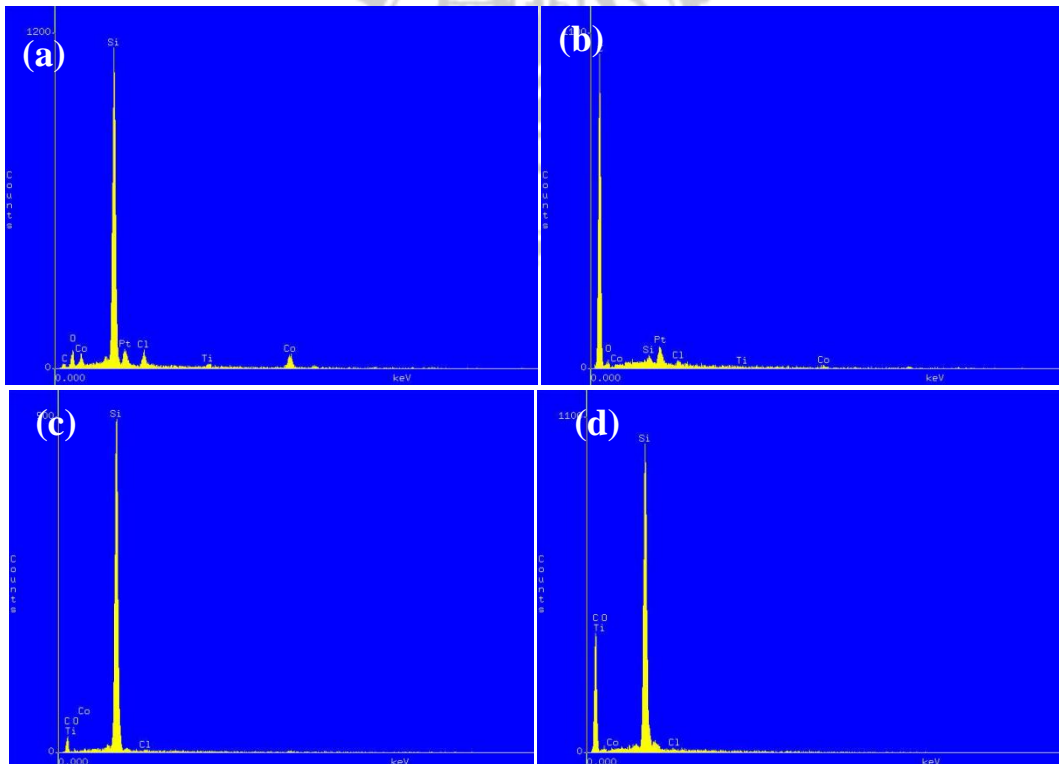
[Fig 3.4.9] EDS spectra for the nanoparticles at the tip of the CNT.
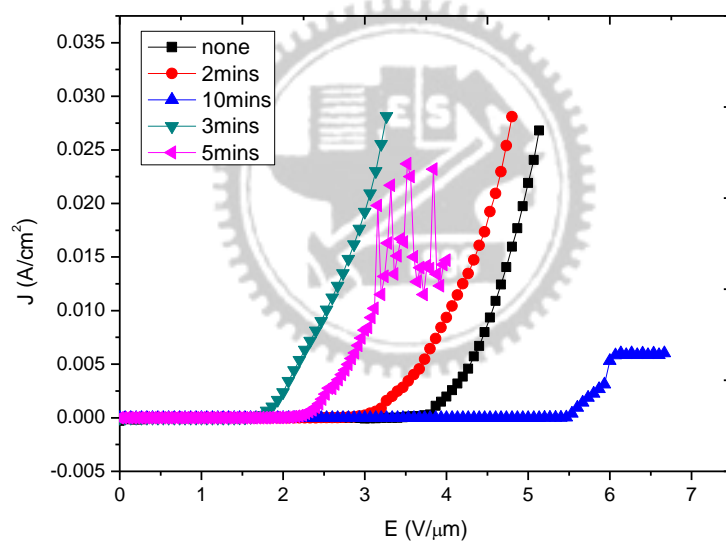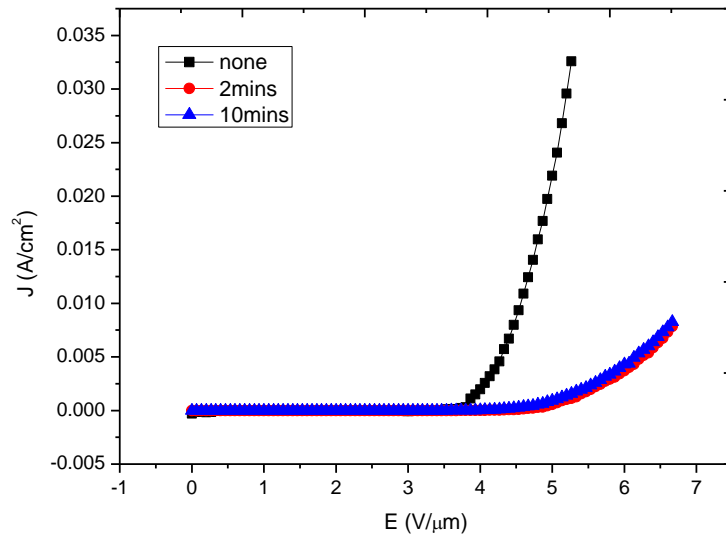
[Fig 3.4.10] Field emission current density vs electric field for a vertically aligned CNT pillar array (a) after O_2 plasma post-treatment and (b) after O_2 mix Cl_2 plasma post-treatment.
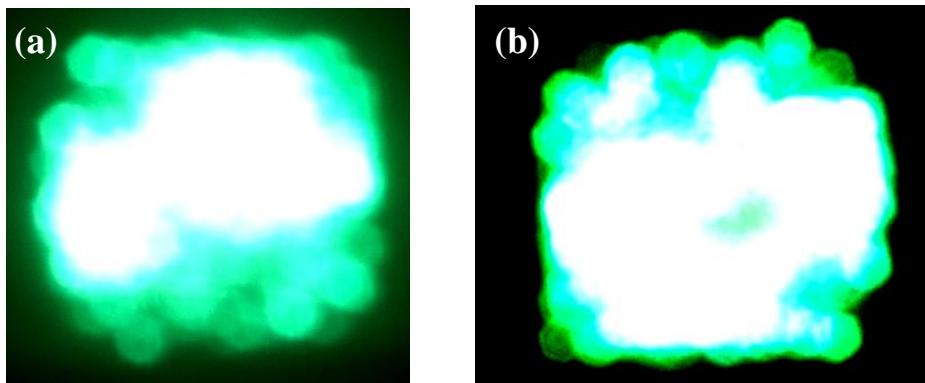
[Fig 3.4.11] Image of fluorescent screen monitoring the field emission from the pillar array (10mm×10mm) at an electric field of 3.33V/μm.(a) no post-treatment, (b) post-treatment for 3min.
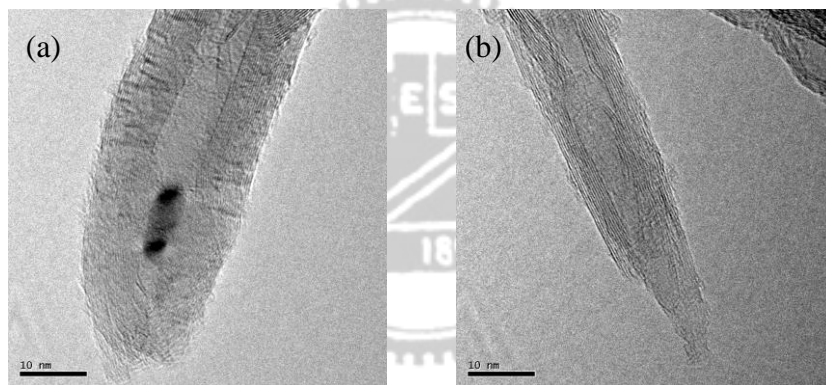
[Fig 3.4.12] TEM analysis (a)before plasma post-treatment, (b)after plasma post-treatment.
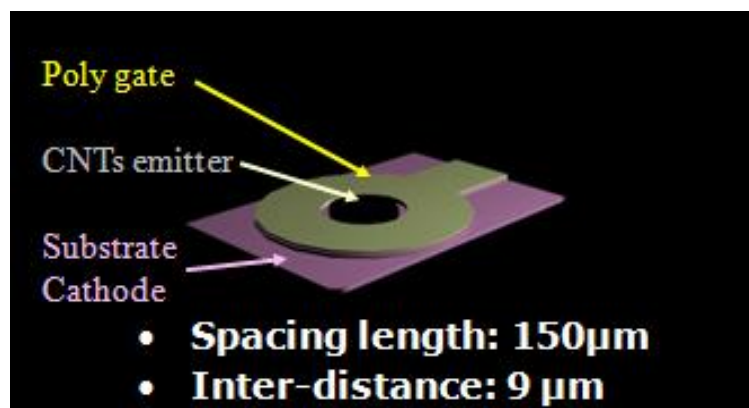
[Fig 3.5.1] Central CNTs were used to be cathode electric emitter, and surrounding

N-type poly-Si was used to be gate of this triode structure by Simulation
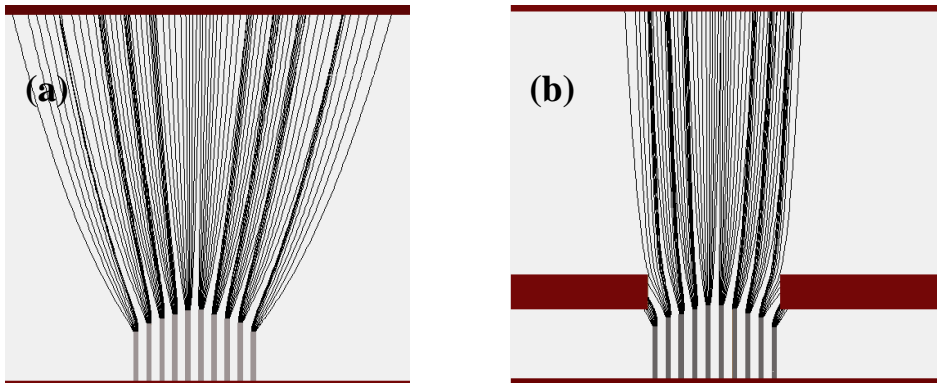
[Fig.3.5.2] Cross-section view for the nanotriode 3D model used for computing the electric field with Simion 3D 7.0. The aligned nanotubes in the bunch have variable heights and may protrude through the gate opening, as shown in the figure, or lie beneath the gate electrode plane.(a) electric field emission without gate structure.(b) electric field emission with 35V gate voltage supplied.
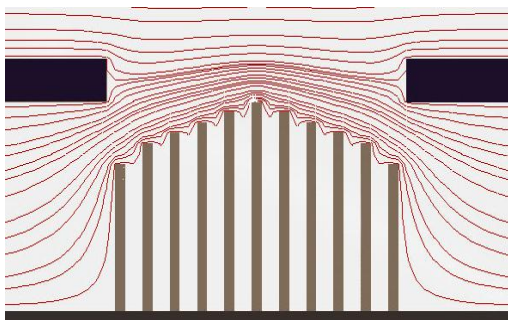
[Fig.3.5.3] Equipotential lines near CNT tips – detail with the gate supplied 35V.
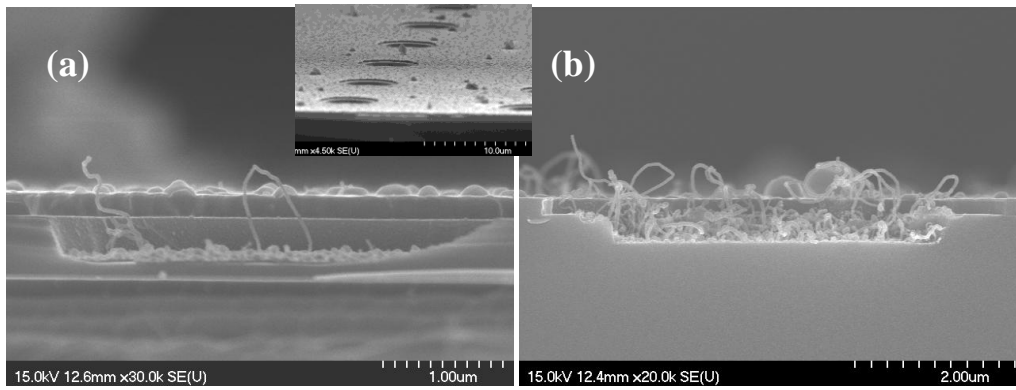
[Fig.3.5.4] The corresponding cross-sectional SEM micrographs showing the CNT lengths of (a) 0.5µm and (b) 1µm. Inset image is triode structure with 9µm inter-distance after CNTs growth.
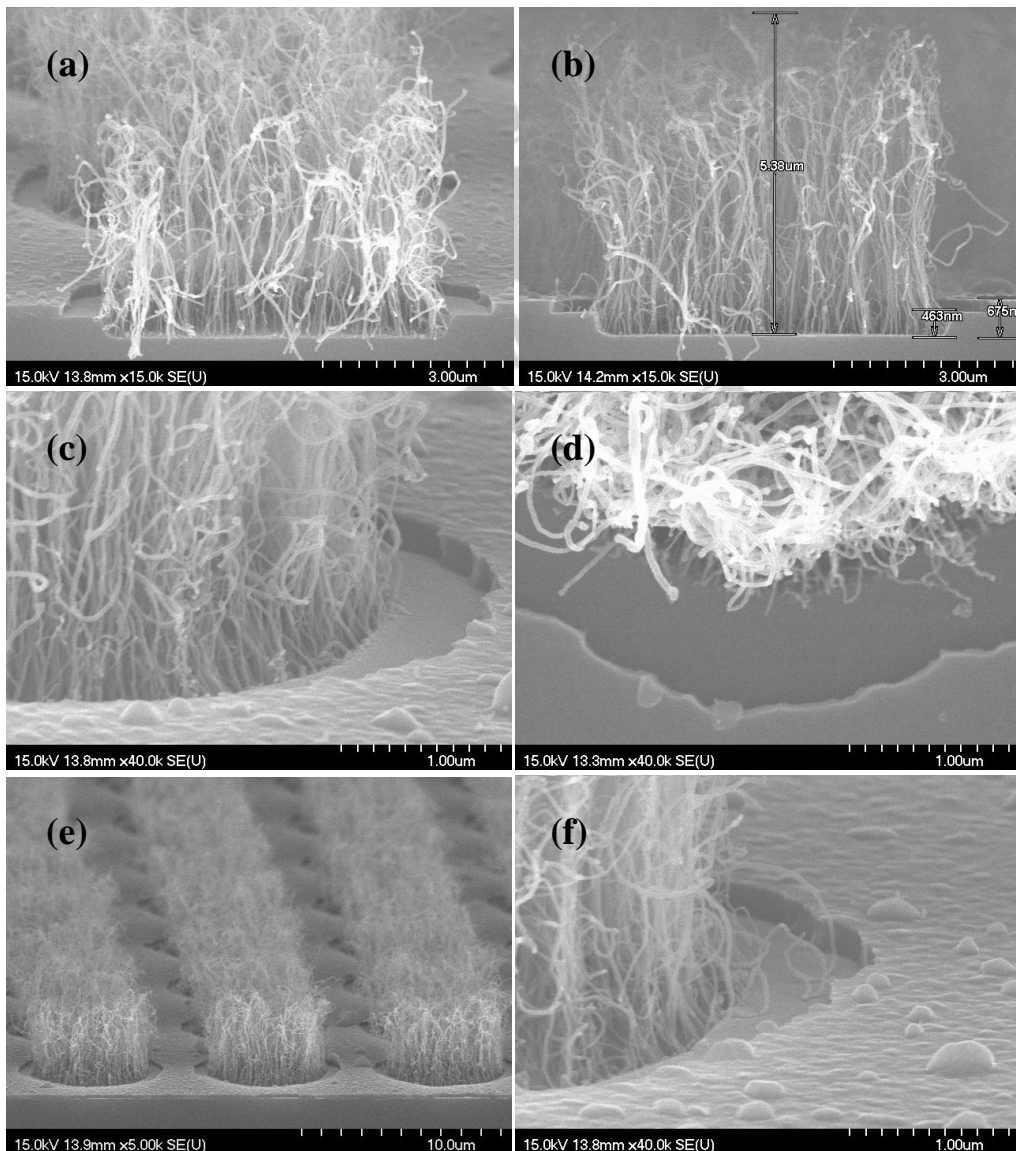
[Fig.3.5.5] The SEM images micrographs showing the CNT lengths of 5µm (a)(e)tilt image (b)cross-section view for triode pillar array (c)(d) the gate-to-emitter gap kept at 0.8µm (f) few CNTs shorted gate to cathode
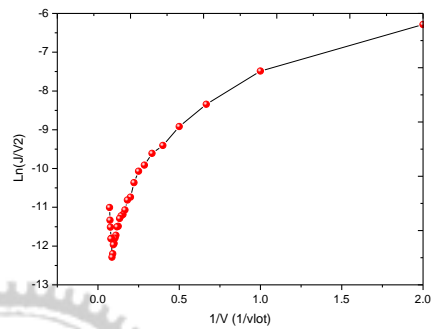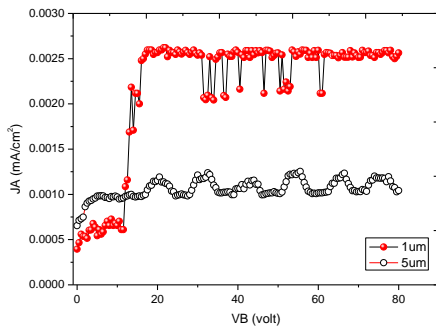
[Fig.3.5.6] The corresponding J_A-V_B plots of the CNT triodes for 1µm and 5µm of nanotubes, respectively.

[Fig.3.5.7] The corresponding F-N plots of the CNT triodes for 1µm of nanatubes.
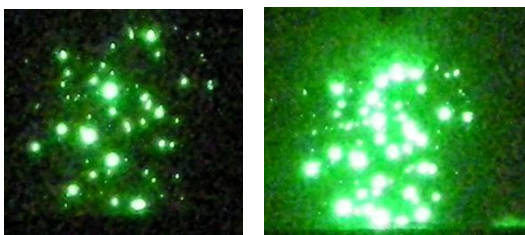
[Fig.3.5.8] Images of fluorescent screen monitoring the field electron emission from the CNT triode array (3mm × 3mm) at the gate voltage (a) 20 V, (b) 30 V , respectively.

Chapter 4

Summary and Conclusions

4.1 Summary and Conclusions

In this thesis, the field-emission characteristics of a pillar array of aligned CNT bundles grown by thermal CVD are investigated. It is indispensable to reduce the turn on field and threshold field to achieve practically applicable field electron emitters that operate at lower power consumption. It has been reported that field emission can effectively enhanced for aligned CNTs as field emitters when the ratio of distance between neighboring nanotubes to the height of each individual CNT is approached 2. To explore the effect of the pillar arrangement on its field emission, R/H is investigated as a function of H by changing H while maintaining R at 80μm、150μm and 250μm, respectively. The experimental results show that the optimum R/H ratio is approaching to 2 when the inter-pillar distance is larger. Pillar like CNT probably behaves like individual field emitter and has less field screening effect within pillar. The results show that when R/H ratios are 8, 4.7 and 3.2 for inter-pillar distance of 80μm、150μm and 250μm , respectively, ultra low turn-on field(1.78V/μm, 1.55V/μm and 1.53V/μm, respectively) is achieved and fluorescent uniformity can also be improved.

Two-step growth method is proposed by adding another growth process just after the previous growth process. When the first growth process is finished, H_2 is added to begin another growth process instead of adding N_2 to cooling the first growth process. This creative idea is to not only keep the catalyst nanoparticle not to be encapsulated by amorphous carbon but also keep the catalyst nanoparticle with activity. Ultra low turn-on field (0.1 V/μm) and

ultra threshold field (0.64 V/μm) are the best value that has been reported to date. Besides, SEM, Raman and TEM are also used to study the material properties of the growth carbon nanotubes. SEM and TEM micrograph show that thinner diameter about 24nm is observed on the top of CNTs′ pillar grown by the two-step growth method. As CNT pillar with one-step skill to two-step technique exhibit the I_G/I_D increases from 1.5 to 1.8 which confirms that the CNTs for the two-step one have a highly crystalline graphite structure for all cases in the experimental design of CNTs synthetic conditions. The best field emission characteristic is therefore achieved due to thinner diameter (i.e. high aspect ratio) and highly crystalline graphite structure.

Next, in order to improve the uniformity and emission performance of electric characteristics, the field emission behaviors of CNT pillar arrays treated with a plasma of a mixture of O_2 and Cl_2 gases is investigated systematically. The field emission enhancement of the pillar arrays after plasma post-treatment is attributed to the physical changes in CNT pillar array by plasma treatment such as enhancement in the geometrical factor due to reduce the screening effect. Furthermore, it also showed a low I_G/I_D ratio in Raman Spectrum analysis, indicating many defects are produced after plasma post-treatment. A low turn-on field of 1.4 V/μm at an emission current density 10 μA/cm^2 Iis achieved when the time of post-treatment is 3 min by O_2 mix Cl_2 plasma.

Finally, utilizing semiconductor fabrication technology and selective-area growth of CNTs, the CNT triode structures can be easily obtained. The gate-to-emitter gap can be reduced to 1μm by controlling the lateral etching time of the poly-Si gate.Furthermore, the results of the simulations and luminescent images clearly indicated that this gate structure with surrounding gate electrodes close to the emitters can cause larger divergence angle of electrons and the emitted electrons traveling through the spacing between cathode and anode

plates would give rise to a more uniform lighting region on the anode plate. Then, the field emission investigation reveals the low gate turn-on voltage of 17 V. These properties offer the promising future of the CNT field emission triode for vacuum microelectronic applications.

References

[1.1]   J. Bardeen and W. H. Brattain, *"The Transistor, A Semi-Conductor Triode,"* Phys. Rev., vol.74, pp.230-231, 1948.

[1.2]   C. A. Spindt, I. Brodie, L. Humpnrey, and E. R. Westerberg, *"Electrical Properties of Thin-film Field Emission Cathodes with Molybdenum Cones,"* J. Appl. Phys., vol. 47, pp. 5248-5251, 1976.

[1.3]   S. M. Sze, *"Physics of Semiconductor Devices,"* 2nd ed., John-Wiley & Sons pulisher, New York, pp. 648-651, 1981.

[1.4]   R. H. Fowler and L. W. Nordheim, *"Electron Emission in Intense Field,"* Proc. R. SOC. A229, pp. 173-181, 1928.

[1.5]   S. Itoh, T. Watanabe, T. Yamaura, and K. Yano, *"A Challenge to Field Emission Displays,"* in Proc. Asia Display, pp. 617-620, Oct. 1995.

[1.6]   R. Meyer, *"Recent Development on Microtips Display at LETI,"* IVMC'91 Technical Digest, pp. 6-9, 1991.

[1.7]   N. E. McGruer and K. Warner, *"Oxidation-sharpened Gated Field Emitter Array Process,"* IEEE Trans. Electron Devices, vol. 38, no. 10, pp. 2389-2391, 1991.

[1.8]   S. E. Huq and L. Chen, *"Fabrication of sub-10 nm Silicon Tips: A New Approach,"* J. Vac. Sci. & Technol. B, vol. 13, no. 6, pp. 2718-2721, Nov. 1995.

[1.9]   D. W. Branston and D. Stephani, *"Field Emission from Metal-coated Silicon Tips,"* IEEE Trans. Electron Devices, vol. 38, no. 10, pp. 2329-2333, Oct. 1991.

[1.10]   V. V. Zhirnov and E. I. Givargizov, *"Field Emission from Silicon Spikes with Diamond Coating,"* J. Vac. Sci. & Technol. B, vol. 13, no. 2, pp. 418-421, 1995.

[1.11]   R. B. Marcus, T. S. Ravi, T. Gmitter, H. H. Busta, J. T. Niccum, K. K. Chin, and D. Liu, *"Atomically sharp silicon and metal field emitters,"* IEEE Trans. Electron

Devices, Vol. 38, pp. 2289-2291, 1991.

[1.12] P. Vaudaine and R. Meyer, "*Microtips fluorescent display,*" IEEE IEDM'91, pp.197-201, 1991.

[1.13] C. Curtin, "*The field emission display,*" International Display Research Conference pp. 12-15, 1991.

[1.14] C. A. Spindt, C. E. Holland, I. Brodie, J. B. Mooney, and E. R. Westerberg, "*Field-emitter array applied to vacuum fluorescent displays,*" IEEE Trans. Electron Devices, Vol. 36, No. 1, pp. 225-228, 1989.

[1.15] David A. Cathey, "*Field emission displays,*" Information Display, p. 16, Oct., 1995.

[1.16] "*Pixtech to produce color FEDs from November,*" News reported in Nikkei Electronics ASIA, p. 42, Nov., 1995.

[1.17] H. G. Kosmahl, "*A wide-bandwidth high-gain small size distributed amplifier with field-emission triodes (FETRODE's) for the 10 to 300 GHz frequency range,*" IEEE Trans. Electron Devices, Vol. 36, No.11, pp. 2728-2737, 1989.

[1.18] P. M. Larry, E. A. Netteshiem, Y. Goren, C. A. Spindt, and A. Rosengreen, "*10 GHz turned amplifier based on the SRI thin film field emission cathode,*" IEEE IEDM'88, pp. 522-525, 1988.

[1.19] C. A. Spindt, C. E. Hollard, A. Rosengreen, and I. Brodie, "*Field emitter array development for high frequency operation,*" J. Vac. Sci. & Technol. B, Vol. 11, pp. 486-473, 1993.

[1.20] C. A. Spindt, "*Microfabricated field emission and field ionization sources,*" Surface Science, Vol. 266, pp. 145-154, 1992.

[1.21] T. H. P. Chang, D. P. Kern, "*A scanning tunneling microscope controlled field emission microprobe system,*" J. Vac. Sci. & Technol. B, Vol. 9, p. 438-443, 1991.

[1.22] H. H. Busta, J. E. Pogemiller, and B. J. Zimmerman, "*The field emission triode as a displacement/process sensor,*" J. Micromech. Microeng., Vol. 3, pp. 45-56, 1993.

[1.23]   H. C. Lee and R. S. Huang, "*A novel field emission array pressure sensor,*" IEEE Transducers- International Solid-State Sensors and Actuators, pp. 241-244, 1991.

[1.24]   Wikipedia "http://en.wikipedia.org/wiki/Image:Cathode_ray_Tube.PNG" 2005

[1.25]   C. A. Spindt, "*A Thin Film Emission Cathode,*" J. Appl. Phys., vol. 39, pp. 3504-3505, 1968.

[1.26]   R. Meyer, A. Ghis, P. Rambaud, and F. Muller, "*Microtips Fluores-cent Display,*" in Proc. Japan Display, pp. 512-514, Sept./Oct. 1986.

[1.27]   S. Itoh AND M. Tanaka, "*Current Status of Field-Emission Displays*", Proceedings of the IEEE, vol. 90, no. 4, pp. 514-520, April. 2002.

[1.28]   M. Ding, H. Kim, and A. I. Akinwande "*Highly Uniform and Low Turn-On Voltage Si Field Emitter Arrays Fabricated Using Chemical Mechanical Polishin*g", IEEE Electron Device Letters, vol. 21, no. 2, pp. 66-69, Feb. 2000.

[1.29]   J Itoh, Y Tohma, K Morigawa, S. Kanemaru and K. Shimizu "*Fabrication of Double Gate Si Field Emitter Arrays for Focused Electron Beam Generation*" J. Vac. Sci. & Technol. B., vol. 13, no. 5, pp. 1968-1972, 1995.

[1.30]   K. Yamamoto, I. Nomura, K. Yamazaki, S. Uzawa and K. Hatanaka, "F*abrication and Characterization of Surface Conduction Electron Emitters*," SID Digest, pp. 1933-1935, 2005.

[1.31]   T. Oguchi, E. Yamaguchi, K. Sasaki, K. Suzuki, S. Uzawa and K. Hatanake, "*A 36-inch Surface Conduction Electron Emitter Display (SED)* ," SID Digest, pp. 1929-1931, 2005.

[1.32]   Iijima S.," *Helical microtubules of graphitic carbon* ," Nature Vol. 354 (6348), pp.56–58, 1991.

[1.33]   Baughman, Ray H., Zakhidov, Anvar A., de Heer, and Walt A. ," *Carbon Nanotubes—The Route Toward Application* ," Science, Vol.297 pp.787-790, 2002.

[1.34]   Gamaly EG and Ebbesen TW," *Mechanism of carbon nanotube formation in the arc*

discharge ," Phys Rev B, 1995,52(3), pp.2083–2089.

[1.35]   Guo T, Nikolaev P, Thess A, Colbert DT, and Smalley RE.," *Catalytic growth of single-walled nanotubes by laser vaporization* ," Chem Phys Lett, Vol. 243, pp.49–54, 1995.

[1.36]   M. P. Siegal, D. L. Overmyer, and F. H. Kaatz ," *Controlling the site density of multiwall carbon nanotubes via growth conditions,*"App. Phys. Lett., Vol. 84, No. 25, pp. 5156-5158, 2004

[1.37]   Yih-Ming Shyu and Franklin Chau-Nan Hong," *The effects of pre-treatment and catalyst composition on growth of carbon nanofibers at low temperature* ,"Diamond and Related Materials Vol.10, pp. 1241-1245, 2001.

[1.38]   Nolan, Peter E., Schabel, Michael J., Lynch, David C," *Hydrogen control of carbon deposit morphology* ,"Carbon , Vol. 33 , No. 1 , pp. 79-85 , 1995

[1.39]   Mi Chen, Chieng-Ming Chen, and Chia-Fu Chen," *Growth of carbon nanotubes by microwave plasma chemical vapor deposition using CH$_4$ and CO$_2$ gas mixture* ,"Thin Solid Films, Vol. 420/421, pp. 230-234. 2002

[1.40]   Mi Chen, Chieng-Ming Chen, Shin-Chen Shi and Chia-Fu Chen," *Low-Temperature Synthesis Multiwalled Carbon Nanotubes by Microwave Plasma Chemical Vapor Deposition Using CH$_4$-CO$_2$ Gas Mixture* ,"Jpn. J. Appl. Phys. Vol. 42, pp. 614–619, 2003.

[1.41]   M. S. Dresselhaus, G. Dresselhaus, K. Sugihara, L. I. Spain, and H. A. Goldberg, "*Graphite fibers and filaments,*" Springer-Verlag, New York, pp. 185-186, 1998.

[1.42]   P. M. Ajayan, "*Nanotubes from carbon,*" Chem. Rev., Vol. 99, pp. 1787-1790, 1999.

[1.43]   S. Iijima and T. Ichihashi, "*Single-shell carbon nanotubes of 1-nm diameter,*" Nature, Vol. 363, pp. 603-605, 1993.

[1.44]   D. S. Bethune, C. H. Kiang, M. S. de Vries, G. Gorman, R. Savoy, J. Vazquez, and R. Beyers, "*Cobalt-catalyzed growth of carbon nanotubes with single-atomic-layer*

walls," Nature, Vol. 363, pp. 605-607, 1993

[1.45]   "http://en.wikipedia.org/wiki/Image:CNTnames.png" 2006

[1.46]   "http://online.itp.ucsb.edu/online/qhall_c98/dekker/" 2006

[1.47]   Y. K. Kwon, T. H. Lee, S. G. Kim, P. Jund, D. Tomanek, and R. E. Smalley. "*Morphology and Stability of Growing Multiwall Carbon Nanotubes*" Phys Rev. Lett., Vol. 79, pp. 2065-2068, 1997

[1.48]   Y. Saito, "*Carbon Nanotubes: Preparation and Physical Properties,*" Asia Display/IDW'01, pp. 11-14, 2001

[1.49]   Min-Feng Yu et al., "*Strength and Breaking Mechanism of Multiwalled Carbon Nanotubes Under Tensile Load,*"   Science, Vol. 287, pp. 637-640, 2000.

[1.50]   Philip G. Collins and Phaedon Avouris, "*Nanotubes for Electronics- Scientific American December*", Vol. 69, 8 pages., 2000

[1.51]   Jing Kong, Nathan R. Franklin, Chongwu Zhou, Michael G. Chapline, Shu Peng, Kyeongjae Cho, Hongjie Dai**,"** *Nanotube Molecular Wires as Chemical Sensors* **,"** Science 28, Vol. 287. no. 5453, pp. 622 – 625, 2000

[1.52]   Cheng H-M, Yang Q-H, and Liu C.," *Hydrogen storage in carbon nanotubes* ," Carbon, Vol. 39, pp.1447–1457, 2001

[1.53]   Derycke, V., Martel, R.; Appenzeller, J. and Avouris, Ph.," *Carbon Nanotube Inter- and Intramolecular Logic Gates,*"Nano Letters Vol. 9, pp. 453-456. 2001

[1.54]   W. B. Choi, D. S. Chung, J. H. Kang, H. Y. Kim, Y. W. Jin, I. T. Han, Y. H. Lee, J. E. Jung, N. S. Lee, G. S. Park, and J. M. Kim, "*Fully Sealed, High-brightness Carbon-nanotube Field-emission Display,*" Appl. Phys. Lett., vol. 75, no. 20, pp. 3129-3131, 1999

[1.55]   Mitsubishi Rayon Co. Ltd. May 24, 2007

[1.56]   Waxin mage Inc. "http://www.wanix.com.tw" 2004-2005

[1.57]   Stefanie "Large-Sized TFT-LCD Industry Report" 2006

[2.1] M. S. Dresselhaus, G. Dresselhaus, and P. Avouris, *Carbon Nanotubes: Synthesis, Structure, Properties, and Application* _Springer, Berlin, 2001_.

[2.2] W. A. de Heer, A. Chatelain, and D. Urgate, Science **270**, 1197 _1995_.

[2.3]S. Fan, M. G. Chapline, N. R. Franklin, T. W. Tombler, A. M. Cassell, and H. Dai, Science **283**, 512 _1999_.

[2.4] Y. C. Kim and E. H. Yoo, Jpn. J. Appl. Phys., Part 2 **44**, L454 _2005_

[2.5] H. Sugie, M. Tanemura, V. Filip, K. Iwata, K. Takahashi, and F. Okuyama, Appl. Phys. Lett. **78**, 2578 _2001_

[2.6]Z. F. Ren, Z. P. Huang, J. W. Xu, J. H. Wang, P. Bush, M. P. Siegal, and P. N. Provencio, Science **282**, 1105 _1998_.

[2.7] S. H. Jo, Y. Tu, Z. P. Huang, D. L. Carnahan, D. Z. Wang, and Z. F. Ren, Appl. Phys. Lett. **82**, 3520 _2003_.

[2.8]L. Nilsson, O. Groening, C. Emmenegger, O. Kuettel, E. Schaller, L. Schlapbach, H. Kind, J.-M. Bonard, and K. Kern, Appl. Phys. Lett. **76**, 2071 _2000_.

[2.9] http://www.nfc.nctu.edu.tw/mechine_new/mechine/HDP-RIE.htm

[2.10] "http://www.wanxin.com.tw" Wanxin mage Inc. 2004-2005

[2.11] Hsia-Wei Chen "*Study on the Carbon-Nanotube Field Emission Devices with the Co/Ti/Al Catalyst and Novel Self-Focusing Gate Structure*" 2007

[2.12] Ref. Japanese Journal of Applied Physics Vol. 43, No. 6B, 2004, pp. L 774–L 776

[2.13] http://www.nfc.nctu.edu.tw/mechine_new/mechine/RIE%20200L.htm

[2.14] Japanese Journal of Applied Physics Vol. 43, No. 2, 2004, pp. 485–491.

[3.1] Huang-Chung Cheng, Rui-Ling Lai, Yao-Ren Chang, Kao-Chao Lin, Chuan-Ping Juan, Pei-Chi Chang, Chein-Ying Lee, and Jiun-Kai Shiu, "*Improvement of Luminescent Uniformity via Synthesizing the Carbon Nanotubes on an Fe–Ti Co-deposited*

Catalytic Layer," Japanese Journal of Applied Physics, vol. 46, No. 2,   pp. 863-866, 2007.

[3.2] Michael J. Bronikowski, "*CVD Growth of Carbon Nanotube Bundle Arrays*" CarBon, Vol.44, pp. 1822-2832, 2006

[3.3]J. Zhang et al. / Carbon 44 (2006) 418–422

[3.4] APPLIED PHYSICS LETTERS VOLUME 76, NUMBER 15 10 APRIL 2000

[3.5] S. Fujii, S. Honda, H. Machida, H. Kawai, K. Ishida, M. Katayama, H. Furuta, T. Hirao, K. Oura, Appl. Phys. Lett. 90 (2007) 153108.

[3.6] APPLIED PHYSICS LETTERS **90**, 153108 _2007_.

[3.7]P. C. Eklund, J. M. Holden, and R. A. Jishi, Carbon **33**, 959 _1995_

[3.8]20S. K. Patra and G. M. Rao, J. Appl. Phys. **100**, 024319 _2006_

[3.9]APPLIED PHYSICS LETTERS **93**, 131921 _2008_

[3.10] Diamond & Related Materials 17 (2008) 556–558

[3.11]Y. Huh et al. / Thin Solid Films 475 (2005) 267–270

[3.12]JOURNAL OF APPLIED PHYSICS **103**, 064312 _2008_